



FEDERAL UNIVERSITY OF DE PERNAMBUCO  
TECHNOLOGY AND GEOSCIENCE CENTER  
CIVIL ENGINEERING DEPARTMENT  
POST-GRADUATION PROGRAM IN CIVIL ENGINEERING

XIMENA ALEJANDRA RODRÍGUEZ FLÓREZ

**EFFECTS OF HYDRO-MECHANICAL AND CHEMICAL DEGRADATION OF  
CARBONATE ROCKS: IMPLICATIONS ON FRACTURE TRANSMISSIVITY**

Recife  
2024

XIMENA ALEJANDRA RODRÍGUEZ FLÓREZ

**EFFECTS OF HYDRO-MECHANICAL AND CHEMICAL DEGRADATION OF  
CARBONATE ROCKS: IMPLICATIONS ON FRACTURE TRANSMISSIVITY**

Thesis presented to the Graduate Program  
in Civil Engineering at The Federal  
University of Pernambuco as a partial  
requirement to obtain the Doctoral Degree  
in Civil Engineering.

Concentration area: Simulation and Oil  
Reservoir Management.

Advisor: D.S.c. Leonardo José do Nascimento Guimarães

Recife

2024

Rodríguez Flórez, Ximena Alejandra.

Effects of hydro-mechanical and chemical degradation of carbonate rocks: implications on fracture transmissivity / Ximena Alejandra Rodriguez Florez. - Recife, 2024. 141f.: il.

Tese (Doutorado) - Universidade Federal de Pernambuco, Centro de Tecnologia e Geociências, Programa de Pós-Graduação em Engenharia Civil, 2024.

Orientação: Leonardo José do Nascimento Guimarães.

1. Fracture transmissivity; 2. Acidification; 3. Rock texture; 4. Roughness; 5. Mineral composition; 6. Torsion displacement. I. Guimarães, Leonardo José do Nascimento. II. Título.

UFPE-Biblioteca Central

CDD 624

XIMENA ALEJANDRA RODRÍGUEZ FLÓREZ

**EFFECTS OF HYDRO-MECHANICAL AND CHEMICAL DEGRADATION OF  
CARBONATE ROCKS: IMPLICATIONS ON FRACTURE TRANSMISSIVITY**

Thesis presented to the Graduate Program  
in Civil Engineering at The Federal  
University of Pernambuco as a partial  
requirement to obtain the Doctoral Degree  
in Civil Engineering.

Concentration area: Simulation and Oil  
Reservoir Management.

Approved: 10/July/2024.

**EXAMINATION COMMITTEE**

---

D.S.c. Leonardo José do Nascimento Guimarães (Advisor)  
Universidade Federal de Pernambuco

---

D.S.c. José Antonio Barbosa (Internal Examiner)  
Universidade Federal de Pernambuco

---

D.S.c. Tiago Siqueira de Miranda (Internal Examiner)  
Universidade Federal de Pernambuco

---

D.S.c. Thomas Finkbeiner (External Examiner)  
King Abdullah University of Science and Technology

---

D.S.c. Flávia Falcão (External Examiner)  
Petrobras

---

D.S.c. Licia Costa (External Examiner)  
Universidade Federal de Pernambuco



XIMENA ALEJANDRA RODRÍGUEZ FLÓREZ

**EFFECTS OF HYDRO-MECHANICAL AND CHEMICAL DEGRADATION OF  
CARBONATE ROCKS: IMPLICATIONS ON FRACTURE TRANSMISSIVITY**

Thesis presented to the Graduate  
Program in Civil Engineering at The  
Federal University of Pernambuco as a  
partial requirement to obtain the Doctoral  
Degree in Civil Engineering.

Concentration area: Simulation and  
Oil Reservoir Management

Approved: 10/July/2024.

**EXAMINATION COMMITTEE**

Participation in person

D.S.c. Leonardo José do Nascimento Guimarães (Advisor)  
Universidade Federal de Pernambuco

Participation in person

D.S.c. José Antonio Barbosa (Internal Examiner)  
Universidade Federal de Pernambuco

Participation in person

D.S.c. Tiago Siqueira de Miranda (Internal Examiner)  
Universidade Federal de Pernambuco

Participation in person

D.S.c. Thomas Finkbeiner (External Examiner)  
King Abdullah University of Science and Technology

Participation by videoconference

D.S.c. Flávia Falcão (External Examiner)  
Petrobras

Participation in person

D.S.c. Licia Costa (External Examiner)  
Universidade Federal de Pernambuco

*Para todos  
mis grandes amores ♡*

## ACKNOWLEDGMENTS

I would like to thank Professors Leonardo Guimarães and Thomas Finkbeiner for their trust and for allowing me to explore knowledge in the development of laboratory experiments and numerical simulation. Thank you to Professor Antônio Barbosa for the insightful discussions. It has been a pleasure for me to work with you three.

I gratefully acknowledge the support of the King Abdullah University of Science and Technology (KAUST), which funded this research under Dr. Finkbeiner's baseline research fund no. 1421. I would also like to express my appreciation to Dr. Carlos Santamarina for his support and valuable insights. I would like to thank colleagues and the lab research staff of the Ali I. Al-Naimi Petroleum Engineering Research Center (ANPERC) at KAUST for assistance.

This study was financed in part by the Coordenação de Aperfeiçoamento de Pessoal de Nível Superior - Brasil (CAPES) - Finance Code 001.

I also acknowledge the Agency for Higher Education Personnel Improvement - Brazilian Ministry of Education (CAPES) and Energi Simulation for funding this work. I would also like to express my gratitude to UFPE colleagues, administrative staff, and GEOQUANTT and ModLab laboratories at the Federal University of Pernambuco (UFPE) for providing access to equipment for petrographic analysis.

Expreso mi más infinita gratitud y amor a mis padres María Nancy y Roberto, por su apoyo incondicional en cada paso que me han acompañado a dar. También agradezco a mi familia -Patricia, Tatiana, Robert, Thomas, Valeria, Luciana, Victoria, Antonia, Melva, Luz Mery, Natalia, Gabriela- por animarme e inspirarme a actuar con amor en todo lo que hago. Gracias a mis amigos, especialmente a Gloria, Daniela, Nivia y Laura, gracias por su compañía. Y un gracias único (como él) a mi mejor amigo y compañero de vida, Alejandro.

## ABSTRACT

Natural fractures are highly stress-sensitive, significantly impacting hydraulic conductivity and flow behavior. This highlights the need for further investigation, particularly concerning the interplay of fracture roughness and mineral composition. Laboratory fluid-flow experiments through hydraulically transmissive fractures in carbonate rocks subjected to mechanical loading, acidizing, and torsion displacement provided insights into how dissolution processes and shear stress induce changes in fracture transmissivity on smooth and rough fracture surfaces with varying mineral compositions and rock textures. This study aims to further investigate these phenomena.

The formations studied in this work, including the Maria Farinha and Gramame Formations, are compositional analogues of Brazilian post-salt reservoirs such as the Santos and Campos Basins, consisting of marly calcareous and marl materials. Additionally, the Jandaíra Formation serves as a textural analogue of Brazilian pre-salt reservoirs like the Barra Velha Formation due to its similar sedimentary textures. The different lithofacies studied—Mudstone, Wackstone, Packstone, Grainstone, and Crystalline rock—were characterized through petrographic analysis, and their elemental compositions were analyzed using X-ray diffraction and X-ray fluorescence tests. The fracture plane topography was scanned before and after acidification to observe changes in roughness due to the presence of the acid.

The impact of normal stress on fracture deformation was studied by applying axial loading and unloading cycles while maintaining a constant flow rate of water injection into the fracture plane. The dissolution effect was produced by injecting 5 cm<sup>3</sup> (at 1 cm<sup>3</sup>/min) of HCl solution (0.01 mol/l and pH = 2), following the same testing protocol described above. Results showed that fracture plane roughness and the size of unmated (i.e., non-contact) regions are critically important. Rough surfaces promote transmissivity enhancement, while smoother surfaces with higher levels of matedness and contact areas between the opposing fracture planes are less affected by chemical degradation. Such surfaces do not present relevant mechanical variations. Grain-supported calcareous lithofacies with high calcium contents and rough surfaces show the most significant increase in fracture transmissivity after acidizing. Conversely, fracture transmissivity after acid treatment in matrix-supported rocks with high calcium contents is low, even in samples with rough fractures and unmated surfaces.

Shear stress and strain were studied by applying constant axial loading while injecting water into the fracture plane at a constant flow rate. Shear displacements resulted from torsion induced by rotating  $\frac{1}{4}$  pitch of the two horizontal screws. The results show that shear strain due to torsion displacement induces variations in fracture transmissivity, which follows asymptotic trend models. Changes in fracture transmissivity due to shear stress are influenced by surface roughness, initial mechanical aperture, and rock texture.

Our findings highlight that fracture surface roughness, mineral composition, and rock texture impact fracture slip during shear failure and chemical dissolution during acidification. The results of both experiments can be used to improve reservoir hydromechanical and geochemical models and provide more robust numerical simulations. Moreover, these results provide valuable insights into understanding the interaction of carbonate rocks with other types of reactive fluids (e.g., carbon dioxide, CO<sub>2</sub>) and the behavior of fluid flow in fractured reservoirs subjected to normal and shear stresses. Although the impact of CO<sub>2</sub> injection is not as intense or significant as acidification using hydrochloric acid, a similar trend of dissolution effects in carbonate rocks is expected.

Keywords: Fracture transmissivity; Acidification; Effective normal stress; Roughness; Mineral composition; Rock texture; Torsion displacement.

## RESUMO

Fraturas naturais são altamente sensíveis ao estresse, impactando significativamente a condutividade hidráulica e o comportamento do fluxo. Isso destaca a necessidade de investigação, particularmente em relação à interação entre a rugosidade das fraturas e a composição mineralógica. Experimentos de fluxo de fluidos em laboratório através de fraturas em rochas carbonáticas, sujeitas a carregamento axial, acidificação e deslocamento por torção, forneceram insights sobre como os processos de dissolução e o estresse de cisalhamento induzem mudanças na transmissividade das fraturas em superfícies lisas e rugosas com diferente composição mineral e textura das rochas. Este estudo tem como objetivo investigar mais detalhadamente esses fenômenos.

As formações estudadas neste trabalho, incluindo as formações Maria Farinha e Gramame, são análogos composicionais dos reservatórios Pós-sal Brasileiro, como as bacias de Santos e Campos, consistindo em materiais calcários margosos e margas. Adicionalmente, a Formação Jandaíra serve como um análogo de textura dos reservatórios do Pré-sal brasileiro, como a formação Barra Velha, devido às suas texturas sedimentares similares. As diferentes litofácies estudadas — Mudstone, Wackstone, Packstone, Grainstone e rocha cristalina — foram caracterizados por meio de análise petrográfica, e suas composições elementares foram analisadas usando testes de difração de raios X e fluorescência de raios X. A topografia do plano de fratura foi escaneada antes e depois da acidificação para observar as mudanças na rugosidade devido à presença do ácido.

O impacto do estresse normal na deformação das fraturas foi estudado aplicando ciclos de carregamento e descarregamento axial enquanto se mantinha uma taxa constante de injeção de água no plano de fratura. O efeito de dissolução foi produzido pela injeção de 5 cm<sup>3</sup> (a 1 cm<sup>3</sup>/min) de solução de ácido clorídrico (HCl de 0,01 mol/l e pH = 2), seguindo o mesmo protocolo de teste descrito acima. Os resultados mostraram que a rugosidade do plano de fratura e o tamanho das regiões não coincidentes (ou seja, regiões sem contato) são criticamente importantes. Superfícies rugosas promovem o aumento da transmissividade, enquanto superfícies mais lisas com níveis mais altos de coincidência e áreas de contato entre os planos de fratura opostos são menos afetadas pela degradação química. Essas superfícies não apresentam variações mecânicas relevantes. Texturas grão-suportadas com altos

conteúdos de cálcio e superfícies rugosas mostram o aumento mais significativo na transmissividade das fraturas após a acidificação. Por outro lado, a transmissividade das fraturas após o tratamento ácido em rochas suportadas por matriz com altos conteúdos de cálcio é baixa, mesmo em amostras com fraturas rugosas e superfícies não acopladas.

A tensão e a deformação por cisalhamento foram estudadas aplicando um carregamento axial constante enquanto se injetava água no plano de fratura a uma taxa constante de fluxo. Os deslocamentos de cisalhamento resultaram da torção induzida pela rotação de  $\frac{1}{4}$  de pitch de dois parafusos horizontais. Os resultados mostram que a deformação por cisalhamento devido ao deslocamento de torção induz variações na transmissividade das fraturas, seguindo modelos de tendência assintótica. As mudanças na transmissividade das fraturas devido ao estresse de cisalhamento são influenciadas pela rugosidade da superfície, abertura mecânica inicial e textura da rocha.

Nossos resultados destacam que a rugosidade da superfície das fraturas, a composição mineral e a textura das rochas impactam o deslocamento das fraturas durante o cisalhamento e a dissolução química durante a acidificação. Os resultados dos experimentos podem ser usados para melhorar modelos hidromecânicos e geoquímicos de reservatórios e fornecer simulações numéricas mais robustas. Além disso, esses resultados fornecem insights valiosos para entender a interação das rochas carbonáticas com outros tipos de fluidos reativos (por exemplo, dióxido de carbono,  $\text{CO}_2$ ) e o comportamento do fluxo de fluidos em reservatórios fraturados submetidos a tensões normais e de cisalha. Embora o impacto da injeção de  $\text{CO}_2$  não seja tão intenso ou significativo quanto a acidificação com ácido clorídrico, espera-se uma tendência similar de efeitos de dissolução em rochas carbonáticas.

Palavras-chave: Transmissividade de fratura; Acidificação; Tensão normal efetiva; Rugosidade; Composição mineralógica; Textura da rocha; Deslocamento por torção.

## TABLE OF FIGURES

Figure 1 –	Rock formation in in-situ stress state is in equilibrium conditions.....	24
Figure 2 –	Drilling rock modifies the stress state of the system.....	25
Figure 3 –	Stress anisotropy effects observed at the wellbore and reservoir scale.....	25
Figure 4 –	Fracture deformation over time due to hydromechanical and chemical effects.....	26
Figure 5 –	World map of the distribution of carbonate reserves .....	27
Figure 6 –	The Brazilian coast section from Recife in the south to Natal in the north. Barbosa (2004, 2007) collects the rocks of the Jandaíra Formation (J1 to J4) near Apodi city (Potiguar Basin; blue star) and Maria Farinha and Gramame samples (M1 and G1 in Poty Quarry and near Itamaracá island ((Paraíba Basin; orange and red stars, respectively) .....	30
Figure 7 –	Different proposed stratigraphic columns over time for the Paraíba Basin defined by (Beurlen, 1967), (Nascimento-Silva et al., 2011), and (Barbosa, 2007) .....	34
Figure 8 –	Comparison of the stratigraphic column of the Paraíba Basin concerning Olinda and Alhandra/Miriri sub-basins .....	35
Figure 9 –	Thin section samples for different facies of the Maria Farinha Formation. Ponta do Funil samples A) and B) Dolosparite with grains of quartz and pyrite (Nichols // 10x and Nichols X / 4x). Poty Quarry samples: C) micrite with high clay and quartz content (Nichols X / 4x); and D) biomicrite (mudstone) with fine crystals of quartz, pyrite, and bioclasts (Nichols X / 4x) .....	36
Figure 10 –	Thin section samples of Gramame Formation. A) PL-01-PE wackestone with dolomite crystals (Nichols X / 4x); B) wackestone of Poty Quarry with bioclast, pyrite and glauconite (Nichols X / 4x); and wackestone to packstone samples of Itapessoca mine (cathodoluminescence / 4x): C)	



	with high bioclasts content (e.g., foraminiferous) and D) microlaminations of clay minerals .....	38
Figure 11 –	Stratigraphic column of Potiguar Basin relating the lithostratigraphic units with the depositional system and tectonic events .....	40
Figure 12 –	Petrographic thin sections of Jandaíra Formation. A) bioclastic grainstone with bivalves, green algae, gastropods, and miliolids. B) peloidal foraminifera grainstone; C) peloidal grainstone with skeletal grains of bivalves and echinoderms; and D) bioclastic floatstone with skeletal grains and echinoderms fragments .....	41
Figure 13 –	Importance of the geomechanical model of a reservoir production over time, from exploration until abandonment .....	43
Figure 14 –	Ternary diagram of the general compositions of the full spectrum of carbonates .....	56
Figure 15 –	Graphic classification of limestones according to type of grains and distribution, proposed by Folk, 1962 .....	60
Figure 16 –	Graphic classification of carbonate deposits according to the depositional conditions of the sediments (from low-energy on the left to high-energy on the right), proposed by Folk in 1962 .....	60
Figure 17 –	Scale of grains and crystals in a carbonate rock, proposed by Folk, 1962 .....	61
Figure 18 –	Classification of sedimentary texture for carbonate rocks proposed by Dunham, 1962 .....	62
Figure 19 –	The Embry and Klovan (1971) classification modified from the Dunham scheme .....	63
Figure 20 –	The Wright (1992) classification modified from the Dunham, Embry - Klovan previous classifications .....	63
Figure 21 –	Ternary diagram of a genetic classification for porosity in a carbonate rock .....	65
Figure 22 –	Equipment, modified from Darcy apparatus, to measure permeability as a function of fluid viscosity and pressure .....	66

Figure 23 –	Representation of a hydraulic and mechanical aperture of a fracture with a flow through it .....	68
Table 1 –	Fracture aperture models from the literature .....	68
Figure 24 –	Descriptive observation scale for roughness, proposed by Hoek-1981 .....	69
Table 2 –	Fracture roughness descriptors from height and texture .....	71
Figure 25 –	Example of a roughness profile and elements to define the mean width (RSm) .....	72
Table 3 –	Fracture transmissivity models .....	73
Figure 26 –	From outcrop rocks of Maria Farinha, Gramame, and Jandaíra formations to core plugs and one specimen for the experiment. ....	74
Figure 27 –	Sample preparation stages: (1) cutting blocks into smaller pieces; (2) subsample plugs; (3) cutting plugs to the required length; (4) smoothing sample surfaces; (5) roughening sample surfaces; (6) scratching the groove; (7) fixing steel cross; (8) drilling inner hole for pressure line to let fluid injection into the fracture plane; (9) sealing the inlet tube with epoxy, and (10) paraffining the perimeter of the samples .....	75
Figure 28 –	The torsional shear device allows measuring the hydromechanical and chemical processes occurring along a pre-existing fracture surface (rough, smooth, mated, and unmated). The equipment comprises (1) a steel reaction frame, (2) an Enerpac cylinder (yellow), and (3) a steel plate with two lever arms moved by (4) two screws mounted horizontally .....	76
Figure 29 –	Experimental setup and measurement accessories .....	77
Figure 30 –	Changes in fracture transmissivity were derived by measuring the sample's normal displacement with an LVDT rod (5) positioned along the Enerpac cylinder (yellow), the injection pressure monitored using a pressure transducer (6) connected to the pump pressure -not shown- before the	

	injected fluid entered the specimen and fracture plane (white dashed line), and the shear displacement using two pairs of strain gauges (7) on each lever arm .....	77
Figure 31 –	Sketch of the side and top view of the screw. The screw's pitch applied during the torsion corresponds with one turn of the screw. Thus, $\frac{1}{4}$ pitch is equal to 0.5 mm .....	79
Figure 32 –	Rock specimens and thin section of Jandaíra, Gramame, and Maríá Farinha formations. The thin sections display low impregnation of the blue-dye epoxy .....	82
Figure 33 –	Petrographic and cathodoluminescence characterization using A- Zeiss polarized-light microscope equipped with an integrated digital camera Axiocam 305 color, and B- Nikon Eclipse polarized petrographic microscope coupled with an X-ray energy dispersive spectrometer .....	83
Figure 34 –	The J1 sample of the Jandaíra Formation was pulverized and prepared for X-ray powder diffraction (XRD) testing using the Bruker D2 Phaser diffractometer .....	84
Figure 35 –	Nanovea ST500 profilometer device used to characterize fracture surfaces on all studied samples .....	85
Figure 36 –	Plug sample cross sections (left) and roughness maps (right) for the: A Jandaíra Formation (Sample J2), with a rough fracture surface; and B Maríá Farinha Formation (Sample M1), with a smooth fracture surface. The roughness scale ranges from blue (indicating low roughness) to red (indicating high roughness) .....	85
Figure 37 –	Illustrations from thin-sections of the samples. These carbonate rocks correspond to microfacies determined by sparite cement type (e.g., biosparite, biopelsparite, and dolosparite) and micrite matrix (e.g., biomicrite) ((Dunham, 1962; Scholle and Ulmer-Scholle, 2005) .....	89
Table 4 –	Geochemical composition of the Maríá Farinha, Gramame, and Jandaíra formations. Major constituents are calcium	

	oxide along with aluminum oxide and silicon dioxide. The results are expressed in weight percentage [wt %] .....	89
Figure 38 –	Correlations of the elemental compositions of the samples: A- CaO vs SiO <sub>2</sub> , showing the influence of carbonate on the depositional system (carbonatic vs terrigenous); B- Al <sub>2</sub> O <sub>3</sub> vs SiO <sub>2</sub> , showing the influence of terrigenous components, such as detrital silicate minerals and clay minerals; and C- MgO vs SiO <sub>2</sub> , indicating the influence of siliciclastic vs carbonatic phases .....	91
Figure 39 –	Comparison of images of fracture surfaces before and after acidizing of the Jandaíra Formation samples: A- Smooth surface, J21; and B- Rough surface, J24. After acidizing, microasperities were smoothed on the smooth surface while cavities were deepened on the rough surface .....	92
Figure 40 –	3D views of rough fracture surfaces after application of the acid and their respective roughness profiles (from along the dashed white lines): A- Sample J3; B- Sample M1; and C- Sample G1. Their predominant mineralogical compositions are included. The values below each profile correspond to the average roughness along the profile. Asperity development after acidizing appears to be strongly related to each sample's mineralogy and texture. ....	93
Figure 41 –	Fracture transmissivity evolution as a function of effective normal stress for samples with smooth surfaces. The presence of microasperities, which occur even in smooth surfaces, governed the different initial mechanical apertures and hydraulic behaviors for each sample .....	95
Figure 42 –	Evolution of fracture transmissivity as a function of effective normal stress during loading and unloading for Sample J24 with a rough surface and Sample J22 with a smooth surface. The fracture transmissivity decreased in both cases, but to different degrees. With loading, the asperities on the rough fracture surface appeared to break irreversibly, reducing the	

	transmissivity to $3 \times 10^{-4}$ cm <sup>2</sup> /s. During unloading, this loss of transmissivity was not recovered. Contrastingly, the smooth fracture surface showed quasi-flat initial fracture transmissivity behavior, but, at close to 4 MPa, it seems to suddenly lose transmissivity. Unlike the rough fracture surface, this loss in transmissivity was recovered during unloading, possibly due to there being a smaller difference between the mechanical and hydraulic apertures .....	96
Figure 43 –	Evolution of fracture transmissivity with effective normal stress cycling before and after acidizing the: A- Smooth; and B- Rough fracture surfaces. Fracture transmissivity was improved by 9% on the smooth surface and 15% on the rough sample .....	98
Table 5 –	Percentage increase in fracture transmissivity after acidizing with the respective elemental contents for samples with smooth and rough fracture surfaces, for a constant normal stress of 0.55 MPa .....	98
Figure 44 –	Relationship between increase in fracture transmissivity and content of: A- Ca; B- SiO <sub>2</sub> ; C- Al; and D- Mg. The greatest improvement in fracture transmissivity relates to a high Ca content with low SiO <sub>2</sub> , Al, and Mg .....	99
Figure 45 –	Vertical displacement as a function of effective normal stress before and after acidizing samples with: A Smooth; and B Rough fracture surfaces. Displacement between the fracture planes evidences the mechanical effect of the fracture (within the same stress cycle). Contrastingly, there was insignificant displacement after applying the acid (red circles) .....	100
Figure 46 –	Relationship between enhancement in transmissivity and rock texture after acidizing for all samples. Smooth and rough fracture surfaces are represented by circles and squares, respectively. Surface roughness and carbonate content (Table 5 and Figure 45) impact the chemical dissolution,	

	mainly on surfaces with pre-existing roughness and in rocks with a grain-supported texture (Samples J14, J24, and J44) more than samples with a fine-grained matrix and smooth fracture surfaces (Samples G13 and M12) .....	101
Figure 47 –	Shear stress and shear strain diagram for Jandaíra Formation rocks with smooth (continuous lines) and rough (dashed lines) surfaces .....	102
Figure 48 –	Fracture transmissivity variations with shear strain from a torsion displacement applied on rocks of the Jandaíra Formation. Squares represent rocks with rough surfaces, and circles represent smooth ones .....	103
Figure 49 –	Transmissivity as a function of shear displacement due to torsion – Jandaíra Formation rocks with rough (filled squares - J15 and J44) and smooth surfaces (filled circles - J33 and J16); and experimental data (empty triangles) and fitted logistic model (lines) developed by Cardona, Finkbeiner and Santamarina (2021) .....	104
Figure A1-1–	Sketch of the cross-sectional area of the sample and sample's shell .....	130
Figure A1-2–	Sketch of a top and side view of a specimen .....	131
Figure A4-1–	Top view of a hollow cylinder relating an infinitesimal area element of it .....	137
Figure A5-1–	Shaft over pure torsion. A- Deformation of the shaft caused by torque ( $M$ ). B- Shear strain ( $\gamma$ ) of the shaft caused by torsion. C- Shear stress acting on an element subjected to torsion. D- Distribution of the shear stress ( $\tau$ ) along the radius of the shaft.....	139
Figure A6-1–	Cantilever beam deflection scheme when experiencing an end load .....	141

## LIST OF SYMBOLS

$A_s$	Sample area (cylinder area) [ $\text{m}^2$ ]
$A$	Cross-sectional area of the sample [ $\text{m}^2$ ]
$A_{in}$	Cross-sectional area of the tube's hole or internal area [ $\text{m}^2$ ]
$A'$	Cross-sectional area of the shell's sample area [ $\text{m}^2$ ]
$A_H$	Fitting parameter in Lomize's hydraulic aperture model
$A_{rong}$	Constant of Rong's model
$b$	Width of a rectangular cross-section of a beam
$B_H$	Fitting parameter in Partir and Cheng's hydraulic aperture model
$B_{rong}$	Constant of Rong's model
$c$	Ratio true contact area to fracture apparent area
$c, c_1, c_2$	Constants
$C_H$	Fitting parameter in Partir and Cheng's hydraulic aperture model
$C_p$	Peak curvature [mm]
$D_{in}$	Inner diameter or diameter of the tube's hole [m]
$D_{out}$	Outer diameter or diameter of the specimen [m]
$E$	Young's modulus [MPa]/ rock stiffness [MPa/m]
$F$	Force [N]
$\bar{F}$	Vector force
$g$	Gravity [ $\text{m/s}^2$ ]
$G$	Shear modulus [MPa]
$h$	Height of the sample/height of a rectangular cross-section of a beam [m]
$h_d$	Correlation distance
$h_0$	Hydraulic aperture at zero normal stress [mm]
$I$	Inertial moment of a beam [ $\text{m}^4$ ]
$k$	Permeability coefficient [ $\text{m}^2$ ]
$K_I$	Intrinsic permeability [ $\text{m}^2$ ]
$K_G$	Geotechnical permeability [ $\frac{\text{m}}{\text{s}}$ ]
$K_{ni}$	Initial normal stiffness [MPa/m]
$K_{n0}$	Initial fracture stiffness [MPa/m]
$Ku$	Kurtosis
JCS	Compressive strength
JRC	Roughness coefficient
$l$	Length of the beam [m]

$L$	Sample/material length [cm]
$L_f$	Fracture length in the direction of flow [mm]
$l_r$	Sampling length [mm]
$\vec{M}$	Vector torque
$M$	Torque [N.m]
$M_s$	Mean slope [°]
$m$	Number of divisions of the roughness profile
$n$	Number of points
$P$	Fluid pressure [MPa]
$\bar{P}$	Average pressure through the sample [MPa]
$P_a$	Atmospheric pressure [MPa]
$P_i$	Pressure in the internal limit [MPa]
$P_e$	Pressure in the external limit [MPa]
$p_f$	Fluid pressure [MPa]
$Q$	Flow rate [m <sup>3</sup> /s]
$R_a$	Average roughness [mm]
$RMS$	Root-mean-square [mm]
$RSm$	Mean width [mm]
$r$	Radius of the sample [m]
$\vec{r}$	Vector radius of the sample
$r_{in}$	Inner radius or radius of the tube's hole [m]
$r_{out}$	Outer radius or radius $r$ of the specimen [m]
$S_c$	Uniaxial compressive strength [MPa]
$Sk$	Skewness
$S_{rong}$	Ratio between normal stress and maximum principal stress
$T$	Fracture transmissivity [cm <sup>2</sup> /s]
$T_c$	Characteristic fracture transmissivity [cm <sup>2</sup> /s]
$X_{si}$	Width of the roughness profile elements [mm]
$\nu_f$	Poisson's ratio
$V_m$	Maximum fracture closure [mm]
$W_0$	Initial fracture aperture [mm]
$W_{Lei}$	Lei's fracture aperture model [mm]
$W_h$	Hydraulic aperture [mm]
$W_m$	Mechanical aperture [mm]
$W_{Rong}$	Rong's fracture aperture model [mm]
$W_{Zob}$	Zoback's fracture aperture model [mm]



$X_i$	Asperities' width [mm]
$Z_i$	Asperities' height [mm]
$\beta$	Constant
$\theta$	Slope at the free end of a cantilever beam/torsion angle [rad]
$\varphi_b$	Internal friction angle [rad]
$d\varphi$	Torsion angle of a cross-section
$\rho$	Fluid density [kg/m <sup>3</sup> ] / radius at any point inside a shaft [rad]
$\gamma$	Shear strain/proportionality constant
$\mu$	Fluid viscosity [Pa s]
$\Delta V_j$	Fracture closure [m]
$\sigma_n$	Normal stress [MPa]
$\sigma$	Total stress [MPa]
$\sigma'$	Effective normal stress [MPa]
$\sigma_{min}$	Least principal stress [MPa]
$\sigma_c$	Characteristic effective stress [MPa]
$\lambda$	Lamé constant [MPa]
$\lambda a$	Average wavelength [mm]
$\eta$	Fracture transmissivity sensitivity
$\delta_{max}$	Maximum deflection of a cantilever beam [m]
$\delta_n$	Fracture normal displacement [mm]
$\delta_s$	Fracture shear displacement [mm]
$\delta_{sc}$	Characteristic shear displacement [mm]
$T_{\delta 0}$	Asymptote when fracture transmissivity tends to zero
$T_{\delta \infty}$	Asymptote when fracture transmissivity tends to infinite
$\tau_s$	Shear stress [MPa]
$\mu_G$	Mean of the geometric aperture [mm]
$\mu_G$	Standard deviation of the geometric aperture [mm]
$\gamma$	Semivariogram
$\zeta$	Fitting parameter

## TABLE OF CONTENTS

<b>SECTION 1 – INITIAL CONSIDERATIONS .....</b>	<b>24</b>
CHAPTER 1 - INTRODUCTION .....	24
1.1    CONTEXT .....	24
1.2    OBJECTIVES .....	27
1.2.1    General Objective .....	27
1.2.2    Specific objectives .....	28
1.3    PREVIOUS EXPERIMENTAL WORK .....	28
1.4    STUDIED ROCKS .....	29
1.5    THESIS ORGANIZATION .....	30
CHAPTER 2 – STATE OF KNOWLEDGE .....	32
2.1    GEOLOGICAL SETTINGS.....	32
2.1.1    Carbonate deposits of the Paraíba Basin.....	33
2.1.1.1    María Farinha Formation (Danian).....	35
2.1.1.2    Gramame Formation (Maastrichtian) .....	37
2.1.2    Potiguar Basin .....	38
2.1.2.1    Jandaíra Formation (Turonian–early Campanian).....	40
2.2    ROCK-FLUID INTERACTIONS.....	41
2.2.1    Geomechanical alterations .....	42
2.2.1.1    Geomechanical alterations due to stress variations .....	46
2.2.1.2    Geomechanical alterations due to acidizing .....	49
2.2.2    Chemical alterations on carbonate rocks .....	50
CHAPTER 3 – THEORETICAL FRAMEWORK.....	55
3.1    CARBONATE ROCKS.....	55
3.1.1    Diagenesis in carbonate rocks .....	56
3.1.2    Properties of a carbonate rock reservoir .....	58
3.1.3    Carbonate rock classifications .....	59
3.1.3.1    Classification of Folk (1962).....	59

3.1.3.2	Classification of Dunham (1962).....	61
3.1.3.3	Dependent properties of carbonate rocks .....	64
3.1.3.3.1	Porosity in carbonate rocks.....	64
3.1.3.3.2	Permeability in carbonate rocks .....	65
3.2	NATURAL FRACTURES .....	67
3.2.1	Fracture properties .....	67
3.2.1.1	Fracture aperture and morphology.....	67
3.2.1.2	Fracture roughness.....	69
3.2.1.2.1	Characteristics of surface roughness in fractures.....	70
3.2.1.2.2	Roughness measurement and analysis .....	70
3.2.1.3	Hydraulic transmissivity .....	72
<b>SECTION 2 – LABORATORY PROCEDURES .....</b>		<b>74</b>
CHAPTER 4 – FRACTURE TRANSMISSIVITY EXPERIMENTS.....		74
4.1	MATERIALS AND SAMPLE PREPARATION .....	74
4.2	EXPERIMENTAL DEVICE AND SETUP .....	76
4.2.1	Experimental measurements and accessories.....	77
4.3	EXPERIMENTAL METHODOLOGY .....	78
4.3.1	Chemical dissolution test procedure .....	78
4.3.2	Torsion test procedure .....	79
4.4	CALCULATED VARIABLES .....	80
CHAPTER 5 – ROCK PROPERTY ANALYSIS.....		82
5.1	MICROSCOPIC CHARACTERIZATION .....	82
5.2	GEOCHEMICAL CHARACTERIZATION .....	83
5.3	FRACTURE SURFACE CHARACTERIZATION .....	84
<b>SECTION 3 – RESULTS AND ANALYSIS.....</b>		<b>87</b>
CHAPTER 6 – ROCK CHARACTERIZATION.....		87
6.1	PETROGRAPHY AND CATHODOLUMINESCENCE .....	87

6.2	GEOCHEMICAL ANALYSIS .....	89
6.3	FRACTURE ROUGHNESS UNDER ACID FLOW .....	91
	CHAPTER 7 – FRACTURE TRANSMISSIVITY .....	94
7.1	FRACTURE TRANSMISSIVITY AS A FUNCTION OF EFFECTIVE NORMAL STRESS	94
7.1.1	Chemo–hydro–mechanical coupling: fracture transmissivity changes due to chemical dissolution .....	97
7.1.2	Chemo–hydro–mechanical coupling: vertical displacement changes due to chemical dissolution .....	99
7.2	CHEMICAL DISSOLUTION: MINERALOGY, ROCK TEXTURE, AND ROUGHNESS .....	100
7.3	FRACTURE TRANSMISSIVITY AS A FUNCTION OF SHEAR STRESS	101
	<b>SECTION 4 – CONCLUDING REMARKS .....</b>	<b>106</b>
	CHAPTER 8 – DISCUSSION, CONCLUSIONS AND RECOMMENDATIONS .....	106
8.1	FINAL DISCUSSION .....	106
8.2	CONCLUSIONS .....	108
8.3	FUTURE WORK .....	109
	BIBLIOGRAPHIC REFERENCES .....	111
	APPENDAGES .....	129

## SECTION 1 – INITIAL CONSIDERATIONS

### CHAPTER 1 - INTRODUCTION

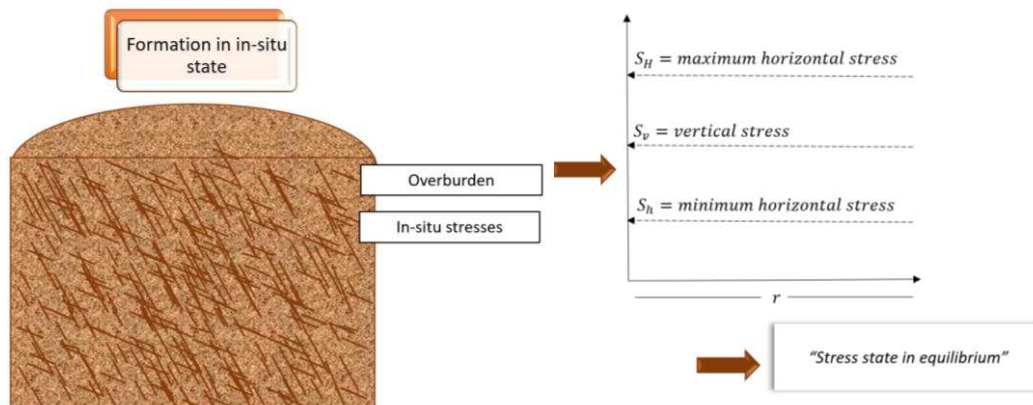
Chapter 1 provides an overview of the relevance and motivation to study fracture transmissivity behavior during hydromechanical and chemical changes on carbonate rocks. Chapter 1 includes a context, objectives, previous experimental study, studied rocks, and thesis organization.

#### 1.1 CONTEXT

A naturally fractured carbonate rock in an *in-situ* stress state is subject only to the overburden and the existing *in-situ* stresses, meaning the system is in equilibrium (Figure 5). However, during well drilling, the stress state of the formation changes as the main stresses are altered and new stresses appear around the well (

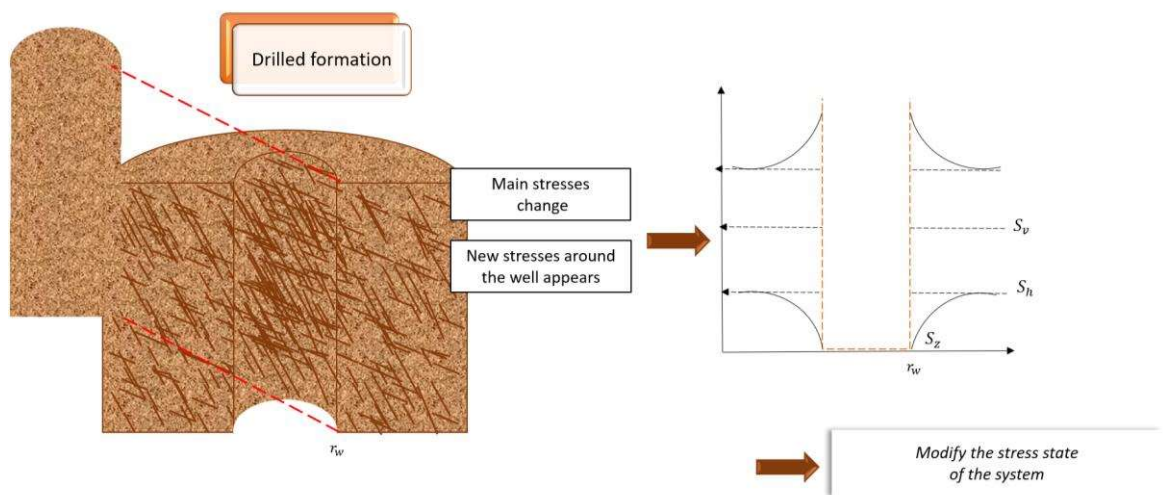
Figure 2). Consequently, the introduction of drilling fluids replaces the rock and increases stress anisotropy, particularly at the wellbore face (Fjaer et al. 2008; Rodríguez, 2017; Rodríguez and Osorio, 2019).

Figure 1- Rock formation *in in-situ* stress state is in equilibrium conditions.



Source: author

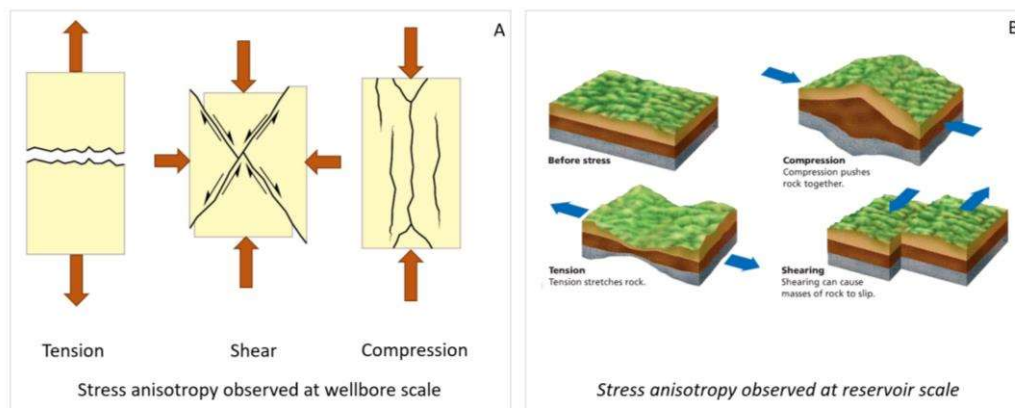
Figure 2- Drilling rock modifies the stress state of the system.



Source: author

Stress anisotropy can be observed at the wellbore scale, where fractures may locally experience compression, tension, and shear (Figure 3). Similarly, these effects can be seen at the reservoir scale, caused by processes such as seismic activity, and fault reactivation, among others. The response to stress anisotropy depends on the type of material: brittle rocks (e.g., those composed of silica) tend to fail with little or no plastic deformation, while ductile rocks (e.g., those rich in clay minerals) can undergo significant plastic deformation before failing. At both the wellbore and reservoir scales, stress anisotropy can alter the intrinsic and mechanical properties of rocks and fractures, potentially leading to a reduction in permeability during oil production activities.

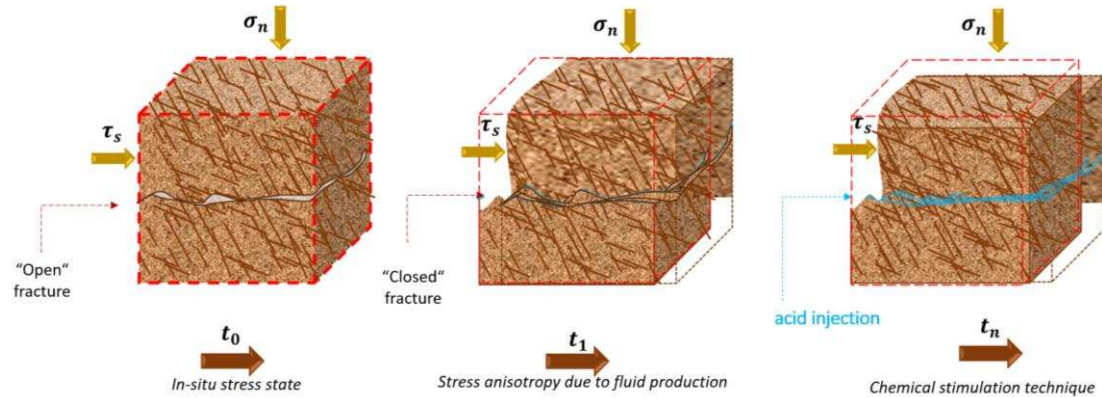
Figure 3- Stress anisotropy effects observed at the wellbore and reservoir scale.



Source: modified from <https://www.files.ethz.ch/structuralgeology> and <https://tr.pinterest.com>

Chemical stimulation techniques, such as matrix acidification and acid fracturing, have been developed to manage these decreases in production by removing the damage (Dong; Zhu; Hill 2001, 2002), as illustrated in Figure 4.

Figure 4- Fracture deformation over time due to hydromechanical and chemical effects.



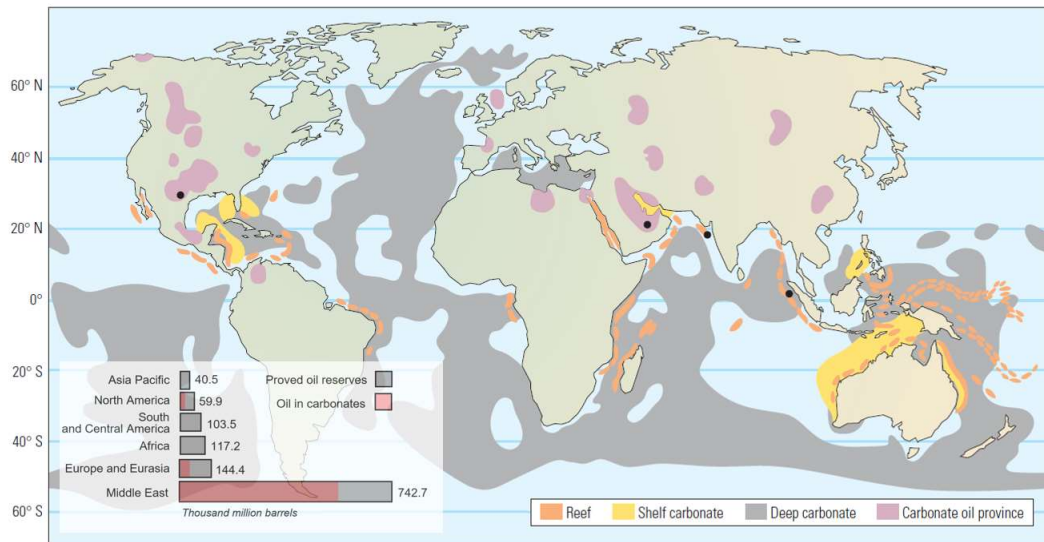
Source: author

When the fractured reservoir is composed of carbonate rock, it is important to understand its reactive nature, as this introduces additional challenges for acid treatment applications (Jin et al. 2020; Wu; Szabian; Sharma, 2020). Diagenesis processes on carbonate rocks result in changes in physical and chemical properties that define the distribution and nature of porosity. The fluid flow pathways result from complex structural elements like vugs, faults, joints, breccias, fractures, and microfractures, causing carbonate rocks to exhibit varying degrees of natural fractures (Araújo et al., 2021; Forstner and Laubach, 2022). Carbonate reservoirs are economically significant in the oil and gas industry, as they contain more than 60 percent of the world's oil and 40 percent of the world's gas reserves (Figure 5). Ahoua and Hincapie (2008) highlight the importance of carbonate reservoirs compared to other types, noting that carbonate rocks hold approximately 3,000 billion barrels of oil and 3,000 trillion standard cubic feet (SCF) of gas.

Understanding fracture deformation, influenced by hydromechanical and chemical effects, is essential for developing high-quality reservoir models. This understanding depends on factors such as stress anisotropy, rock petrophysical and poro-mechanical properties, and fracture attributes (Rodríguez and Osorio, 2019). The study aimed to conduct experiments to observe these effects in relation to rock

characteristics like texture, surface roughness, and mineral composition. It sought to provide insights into fracture transmissivity behavior under acidizing, as well as normal and shear stresses.

Figure 5- World map of the distribution of carbonate reserves.



Source: Modified of Ahoua and Hincapie (2008, p. 21); Akbar et al. (2015, p. 7)

The experiments were carried out using carbonate rock samples from the Potiguar and Paraíba basins in Northeastern Brazil. These samples varied in composition, texture, carbonate content, and roughness. The results revealed how rock texture, surface roughness, and mineral composition affected the outcomes of acidification and the influence of shear stress from torsion displacement on fracture transmissivity.

## 1.2 OBJECTIVES

### 1.2.1 General Objective

The main objective of this research is to investigate how roughness, rock texture, and mineral composition of carbonate rocks affect fluid flow through fractures due to chemo-hydro-mechanical alterations.



### 1.2.2 Specific objectives

The specific objectives of this study are:

- a) Develop and apply an experimental protocol using the Torsional Ring Shear Device to include fracture surfaces with asperities, aiming to study the influence of roughness in response to acid presence. Previous experimental protocols have only examined smooth surfaces.
- b) Conduct experiments to estimate fracture transmissivity and vertical displacement variations as a function of normal stress, both before and after applying acid treatment to fracture surfaces with varying degrees of roughness.
- c) Analyze the mechanical and chemical effects on fluid flow concerning properties such as roughness, mineral composition, and rock texture.
- d) Compare the laboratory results of fracture transmissivity changes due to shear stress with findings from previous studies.

### 1.3 PREVIOUS EXPERIMENTAL WORK

We conducted experiments using the Torsional Ring Shear Device developed by Cardona, Finkbeiner and Santamarina (2021). In their study, Cardona, Finkbeiner, and Santamarina injected an HCl solution into pre-fractured limestone samples from the Middle East, which resulted in smooth fractured surfaces. Their findings suggested that acidification improved fracture transmissivity without significantly altering vertical displacement. They proposed that the acid preferentially affected the free fracture planes, leaving the contact areas relatively unchanged. Additionally, Cardona, Finkbeiner, and Santamarina described the mechanical effects of fracture deformation due to normal effective stress and torsion displacement, demonstrating that fracture transmissivity as a function of shear displacement is influenced by roughness, matedness, and normal stress.

Building on their work, we extended the study to further investigate the impact of fracture surface roughness, rock texture, and mineral composition on fracture transmissivity. Our research focused on how these factors interact with normal stress, torsion displacement, and chemical dissolution in various Brazilian carbonate rocks.

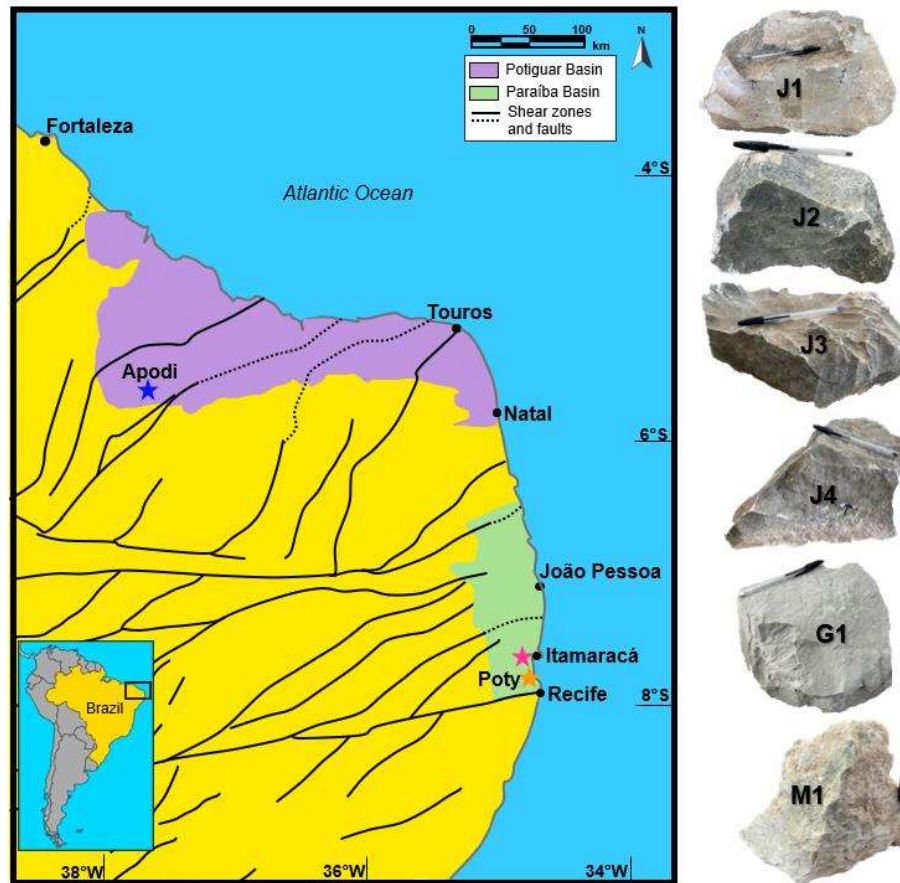
#### 1.4 STUDIED ROCKS

The studied carbonate rocks exhibit various diagenetic aspects, including late alteration phases resulting from exhumation and meteoric influences (Barbosa, 2004; Barbosa et al., 2007; Córdoba, 2004). They present similarities to carbonate successions found in the Pre-salt and Post-salt rocks of the Campos and Santos basins on Brazil's southeastern margin. Therefore, despite the general nature of the study, the information provided can be valuable for reservoir analog applications. For instance, the *María Farinha* and *Gramame* formations are lithologically and depositional similar to the post-salt successions of the Campos Basin (*Macaé Group* – *Quissamã* and *Outeiros* formations) (Okubo, 2014; Okubo et al., 2015). Similarly, the *Jandaíra* Formation shares textural similarities with the carbonate deposits of the *Barra Velha* Formation in the pre-salt Santos Basin (Sartorato; Tonietto; Pereira, 2020).

Figure 6 shows a map of Northeastern Brazil and its continental margin, highlighting the coastal zones of the *Paraíba* Basin, located between João Pessoa and Recife, and the *Potiguar* Basin, located west of Natal. The locations of the outcrops from which rock samples were collected are marked with stars (Figure 6).

Samples from the *Paraíba* Basin include the *Gramame* (Maastrichtian) and *Maria Farinha* (Danian) formations (Barbosa, 2004; Barbosa et al., 2007). Samples from the *Potiguar* Basin include the *Jandaíra* Formation (Turonian-Campanian) (Córdoba et al., 2007). Specifically, samples from the *Jandaíra* Formation (J1 to J4) were collected from outcrops near Apodi city (*Potiguar* Basin; blue star in Figure 6), while samples from the *María Farinha* and *Gramame* formations (M1 and G1) were collected from outcrops at the *Poty Quarry* and *Itamaracá Island* (*Paraíba* Basin; orange and red stars, respectively, Figure 6).

Figure 6 - Map of northeastern Brazil and its continental margin. The coastal zone of two marginal basins is depicted, Paraíba Basin, to the north of Recife, and Potiguar Basin, to the west of Natal. The locations of the outcrops where the samples were collected are marked with stars, J1 to J4 (Jandaíra Fm.) near the Apodi Ciy (blue star), M1 and G1 (Gramame and Maria Farinha Fms), in the Poty Quarry and Itamaracá Island (orange and red star).



Source: author

## 1.5 THESIS ORGANIZATION

The thesis is organized into four main sections, each encompassing various chapters.

Section 1, titled "Initial Considerations," includes Chapters 1 to 3. Chapter 1 introduces the problem and objectives of the study. Chapter 2 reviews the geological settings of the Maria Farinha, Gramame, and Jandaíra formations and provides a literature review on rock-fluid interactions. Chapter 3 presents the theoretical framework, focusing on key concepts related to carbonate rocks and natural fractures.

Section 2 covers Chapters 4 and 5, which detail the laboratory procedures for the fracture transmissivity experiments. Chapter 4 describes the sample preparation, experimental device, methodology, and calculated variables. Chapter 5 outlines the methodology developed for rock characterization, including microscopic, geochemical, and roughness analyses.

Section 3 consists of Chapters 6 and 7, which present the results and analysis. Chapter 6 discusses the results of rock characterization, while Chapter 7 examines changes in fracture transmissivity as influenced by effective normal stress, chemical dissolution, and shear stress.

Section 4 is dedicated to final considerations and includes Chapter 8, which summarizes the final discussion, conclusions, and suggestions for future work. The appendices, which provide basic concepts and details of the development of equations used in this research, are presented at the end of the thesis.

## CHAPTER 2 – STATE OF KNOWLEDGE

Chapter 2 provides a comprehensive literature review of previous research on various aspects of the Brazilian rocks studied in this research. It covers the geological evolution, petrographic, geochemical, depositional, diagenetic, and structural characteristics of these rocks. Additionally, Chapter 2 reviews and discusses studies on rock-fluid interactions, focusing on methodologies, experiments, models, criteria, and tools used to evaluate geomechanical changes resulting from stress variations and acidification. The chapter also examines research on alterations in carbonate rocks due to chemical effects.

### 2.1 GEOLOGICAL SETTINGS

Outcrop rocks are valuable analogs for studying reservoir behavior (e.g., Brazilian Pre-salt and Post-salt rocks) and processes during exploration, production, and stimulation. Researchers use these outcrops to compare with subsurface data, applying various methodologies to validate the accuracy of their findings. Studies have demonstrated the importance of using outcrop analogs for reservoirs, revealing that outcrop characteristics often correlate well with subsurface results, both mechanically and chemically (Becker et al., 2018; Forstner and Laubach, 2022; Ghosh et al., 2018; Homuth and Sass, 2014; Laubach et al., 2014). Consequently, analog studies are employed to understand, characterize, and model subsurface rocks.

However, outcrop rocks can display distinctive features due to uplift or near-surface exposure processes, such as telodiagenesis (late diagenesis), dissolution from meteoric fluids, and cracking. It is crucial to determine whether the rocks used in experiments have undergone such alterations and to distinguish these from earlier diagenetic events (eo- and meso-diagenesis).

This research focuses on carbonate rocks collected from outcrops in the coastal zones of the Paraíba and Potiguar basins in northeastern Brazil, between the cities of Recife and Natal (Figure 6). Specifically, the rocks from the Jandaíra, Gramame, and Maria Farinha formations show varying degrees of exposure-related diagenetic effects, such as dolomitization, crack formation, and karstification. To address this, we

conducted a petrographic analysis to describe both earlier and recent stages of diagenesis, helping to identify the effects related to telodiagenesis. Furthermore, the outcrop rocks selected for this study consist only of intact rock portions without natural fractures, making it unlikely that telodiagenesis has significantly altered their matrix mineralogy.

### **2.1.1 Carbonate deposits of the Paraíba Basin**

Initially, the Pernambuco-Paraíba Basin was regarded as a continuous sedimentary belt extending from the Cretaceous to the Quaternary Lineament (Brito, 1979 qtd. in (Barbosa, 2004)). However, advances in geological knowledge have revealed the existence of two distinct basins, separated by the Pernambuco Lineament (Lima Filho, 1998; Lima Filho; Barbosa; Souza, 2006). Consequently, the Paraíba Basin was defined as the region between the Pernambuco Lineament and Touro's Peak (Lima Filho; Barbosa; Souza, 2006). Based on the stratigraphic analysis, Barbosa (2004, 2007) proposed extending the Paraíba Basin from the Pernambuco Lineament to Mamanguape's Peak.

Asmus (1984) detailed the evolution of the Paraíba Basin as an independent basin on the Brazilian continental margin during the South Atlantic's opening when Africa separated from South America (El Gadi and Brookfield, 1999; Mabesoone and Alheiros, 1988). The Paraíba Basin is classified as a rift passive margin that was deposited from the Coniacian?-Santonian to the Paleocene (Barbosa, 2004; Kegel, 1954; Neumann et al., 2009). It consists of a sedimentary succession featuring continental and fluvial sandstones, calciferous sandstones, marls, and limestones.

Figure 7 illustrates the progression of knowledge regarding the stratigraphy and definition of the Paraíba Basin from 1967 (Beurlen, 1967), 1993 by Mabesoone qtd. in Nascimento-Silva et al. (2011), and the most recent studies by Barbosa in 2007. The latest stratigraphic studies of the Paraíba Basin reveal a Precambrian crystalline basement, overlain by Cretaceous sediments including the Beberibe, Itamaracá, and Gramame formations, Tertiary sediments of the Maria Farinha Formation, and Quaternary sediments of the Barreiras Formation at the top (though not shown in Figure 7, as reported by Barbosa, 2007).

Figure 7 – Different proposed stratigraphic columns over time for the Paraíba Basin defined by (Beurlen, 1967), (Nascimento-Silva et al., 2011), and (Barbosa, 2007).

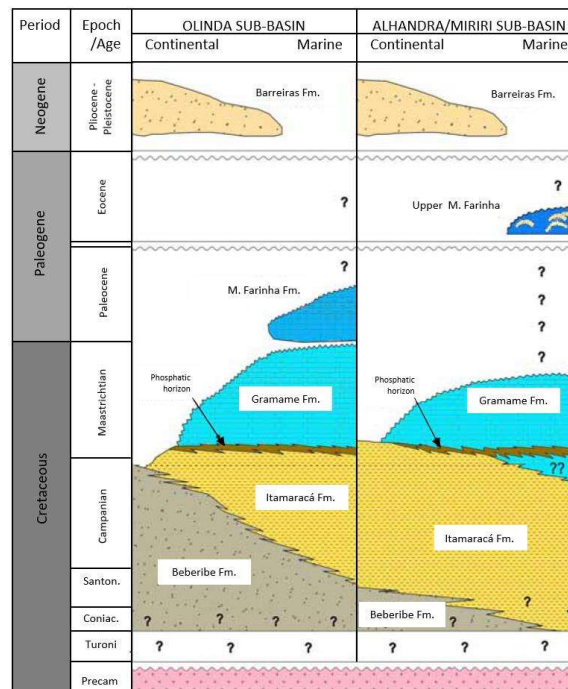
Beurlen, 1967					Mabesoone et al., 1993			Barbosa, 2007						
Pernambuco-Paraíba Basin					Pernambuco-Paraíba Basin: Olinda, Alhandra and Miriri Sub-basins			Paraíba Basin						
								Olinda Sub-basin			Alhandra and Miriri Sub-basins			
P a r a í b a	Age	Stratigraphy	Lithofacies		Lithology	Paraíba Group	Period/Age		Stratigraphy	Period	Age	Stratigraphy		
	Eocene (?) Paleocene	Maria Farinha Formation	Regression marine carbonate sequence		Fine and coarse limestone, carbonate mudstone		Tertiary	Eocene Paleocene	Maria Farinha Formation (35m)	Tertiary	Eocene	?		Upper Maria Farinha Formation
												Paleocene	Maria Farinha Formation	?
	Maastrichtian	Gramame Formation	Parallel Stratification	Carbonate	Marl		Cretaceous	Maastrichtian	Gramame Formation (40m)	Cretaceous	Maastrichtian	Gramame Formation	Gramame Formation	
				Coastal	Carbonate sandstone and calcarenite						Campanian	Itamaracá Formation	Itamaracá Formation	
				Phosphatic	Phosphatic calcarenite						?	?		
	Campanian-Santonian	Beberibe Formation	Parallel Stratification	Fluvial	Medium sandstone and conglomerate		Cretaceous	Campanian-Santonian	Beberibe Formation ( ±300m)	Cretaceous	Coniacian-Santonian-Campanian	Beberibe Formation	Beberibe Formation	
				Estuarine	White sandstone and rounded						?	?		
				Lagoon	Silt						?			
	Precambrian		Crystalline Basement				Precambrian	Crystalline Basement		Precambrian	Crystalline Basement			

Source: Nascimento-Silva et al. (2011, p. 383)

The Paraíba Basin is bordered to the south by the Pernambuco Shear Zone and to the north by the Patos Shear Zone, located north of João Pessoa (Barbosa et al., 2007). The sedimentary succession of the Paraíba Basin includes several key formations: the Beberibe Formation, consisting of fluvial-lacustrine sandstones (Beurlen, 1967); the Itamaracá Formation, characterized by calcareous sandstones and siltstones with marine fossils that indicate a continent-ocean environmental transition (Barbosa, 2004; Beurlen, 1967; Kegel, 1954; Santos et al., 1994); the Gramame Formation, made up of limestones and marls deposited during a marine transgression (Barbosa, 2004; Santos et al., 1994); the Maria Farinha Formation, which contains marine sediments similar to those in the Gramame Formation and represents a regressive phase of the basin (Barbosa, 2004, 2007); and the Barreiras Formation, composed of sandy clay sediments (Mabesoone and Alheiros, 1988).

Figure 8 illustrates the stratigraphic column proposed (Barbosa, 2004; Barbosa; Lima Filho; Neumann, 2003), and subsequently modified by Barbosa (2004, 2007), based on data collected from the Olinda and Alhandra/Miriri sub-basins.

Figure 8 – Comparison of the stratigraphic column of the Paraíba Basin concerning Olinda and Alhandra/Miriri sub-basins.



Source: Modified from Barbosa (2007, p. 29)

#### 2.1.1.1 Maria Farinha Formation (Danian)

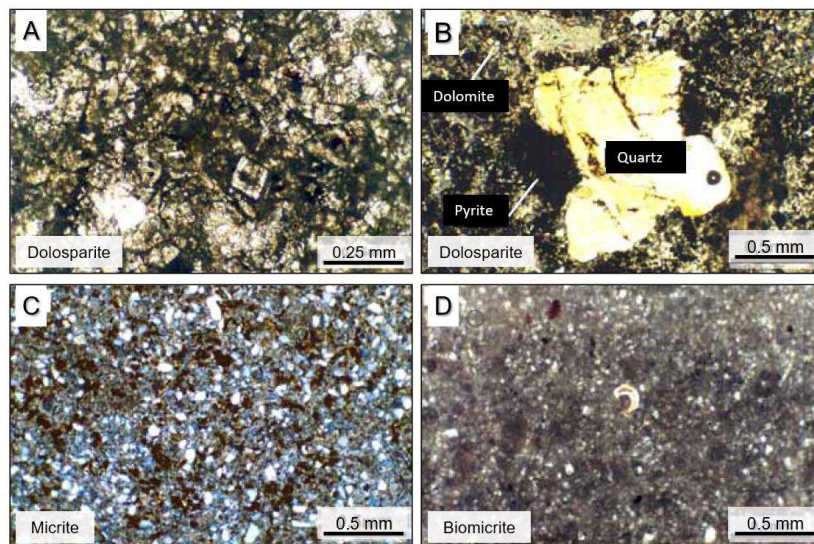
The sedimentation of the Maria Farinha Formation in the Paraíba Basin represents the beginning of a regressive phase (Barbosa, 2004; Beurlen, 1967) that occurred during the lowest stage of the Paleocene Epoch (Danian). Shallowing-upward cycles of marly-limestone and marl beds, associated with a shallow platform, dominate the Maria Farinha Formation (Barbosa and Lima Filho, 2006; Barbosa, 2004; Beurlen, 1967; Córdoba et al., 2007). El Gadi and Brookfield (1999) describe the lower part of the formation as graded bioclastic limestone interbedded with marls and shales, while the upper portion consists predominantly of limestones. The presence of benthonic and planktonic foraminifers supports the formation's association with a shallow water environment.

The microfacies within the Maria Farinha Formation include bioclastic mudstones, wackestones, and packstones, with siliciclastic particles indicating terrigenous influence towards the formation's deposition (Barbosa; Neumann; Lima Filho, 2007; Nascimento-Silva et al., 2011). The regressive phase led to an increased



contribution of clay and detrital siliciclastic materials, as illustrated in Figure 9B to Figure 9D. Gertsch et al. (2013) note the presence of clay minerals such as kaolinite, illite, and smectite, along with detrital siliciclastic components, including quartz and feldspar grains of 1 to 2 mm reported by Barbosa (2007). Dolomitization is evident in regions with high meteoric influence, as shown in Figure 9A and Figure 9B. Additionally, Barbosa (2007) highlights diagenesis processes that have increased porosity through dissolution.

Figure 9 – Thin section samples for different facies of the Maria Farinha Formation. Ponta do Funil samples A) and B) Dolosparite with grains of quartz and pyrite (Nichols // 10x and Nichols X / 4x). Poty Quarry samples: C) micrite with high clay and quartz content (Nichols X / 4x); and D) biomicrite (*mudstone*) with fine crystals of quartz, pyrite, and bioclasts (Nichols X / 4x).



Source: Modified from Barbosa (2007, p. 138)

Conglomerate calcareous sediments (Albertão, 1993, qtd. in Barbosa, 2004) and the extinction of marine plankton (Barbosa, 2007) mark the Tertiary-Cretaceous boundary, corresponding to the Gramame Formation. Barbosa (2007) observed that sediments in the central region of the Olinda Sub-basin at Maria Farinha exhibit facies and microfacies similar to those in the Gramame Formation. However, detrital quartz is relatively rare in the Gramame Formation compared to the upper portion of the Maria Farinha Formation (Barbosa, 2007).

Beurlen (1967) described the Maria Farinha Formation sediments as being restricted to the Recife and Goiana River Valley coastal strip within the Olinda Sub-basin. This observation implies that the marine environment in the basin became

restricted after the Maastrichtian. Consequently, Beurlen (1967) identified two distinct facies within the Maria Farinha Formation: pure carbonates, which are occasionally recrystallized in the upper part, and detrital carbonates, marly limestones, and clays in the lower part.

#### 2.1.1.2 Gramame Formation (Maastrichtian)

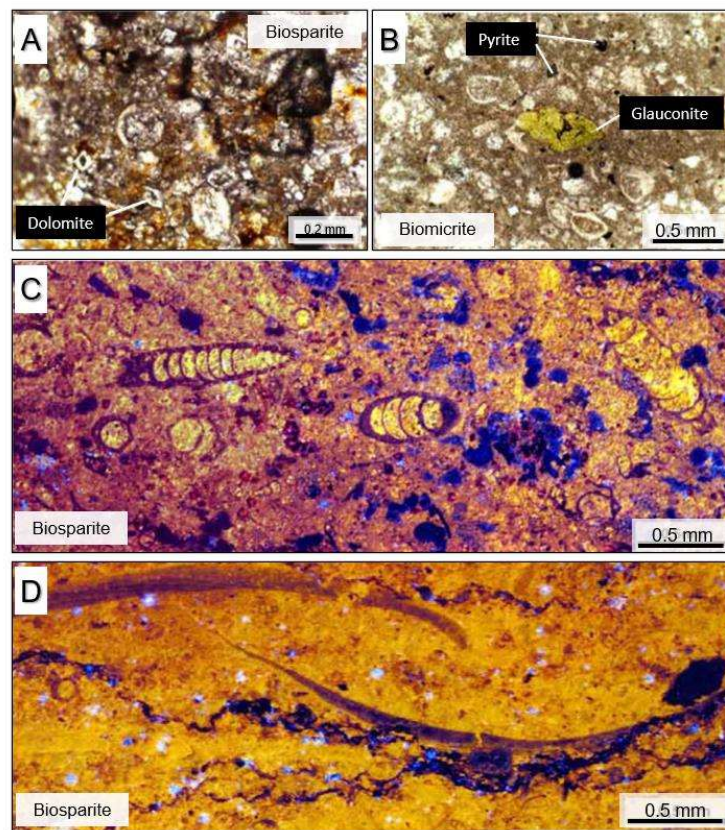
The Gramame Formation, deposited during the Maastrichtian, represents a shallow platform system characterized by shallowing-upward cycles of marly limestones and marls. The presence of a distinctive paleofauna, including planktonic foraminifera, indicates a low to moderate energy deposition environment typical of a shallow platform regime (Barbosa, 2004, 2007; Barbosa; Lima Filho; Neumann, 2003). The formation was also influenced by estuarine conditions, with a continuous influx of terrigenous sediments (Barbosa et al., 2007; El Gadi and Brookfield, 1999; Nascimento-Silva et al., 2011).

The Gramame Formation is rich in fossils such as bony fish, crustaceans, selachians, reptiles, echinoderms, and mollusks (Barbosa, 2004, 2007). However, a reduction in invertebrate fauna occurred at the end of the Maastrichtian, likely due to environmental crises at the close of the Cretaceous (Barbosa, 2004; Barbosa and Lima Filho, 2006; Gertsch et al., 2013). During the Cretaceous-Tertiary transition, a regressive event increased the energy of the depositional environment, shifting from low to high energy and enhancing the contribution of terrigenous particles to the Gramame Formation, which led to changes in sedimentary facies (Barbosa, 2004; Barbosa and Lima Filho, 2006; Barbosa; Lima Filho; Neumann, 2003). This event also marks an erosive unconformity and the beginning of the deposition of the Maria Farinha Formation.

The Gramame Formation features microfacies such as mudstones, wackestones, and packstones containing bioclasts and siliciclastic grains (Barbosa and Lima Filho, 2006; Barbosa, 2007; Barbosa et al., 2007; Córdoba et al., 2007; El Gadi and Brookfield, 1999; Gertsch et al., 2013). Barbosa (2007) notes dolomitization in coastal regions due to meteoric influences (Figure 10A) and documents diagenetic events associated with dolomitization, as well as the presence of pyrite, phosphate, and

glauconite (Figure 10B). Figure 10C displays a cathodoluminescent image of the Gramame Formation, showing foraminifera within a matrix of spatic calcite (Barbosa, 2004, 2007). Additionally, Figure 10D illustrates a biosparite with microlaminations of clay minerals, such as illite, smectite, chlorite, and kaolinite (Barbosa, 2007).

Figure 10 - Thin section samples of Gramame Formation. A) PL-01-PE *wackestone* with dolomite crystals (Nichols X / 4x); B) *wackestone* of Poty Quarry with bioclast, pyrite and glauconite (Nichols X / 4x); and *wackestone to packstone* samples of Itapessoca mine (cathodoluminescence / 4x): C) with high bioclasts content (e.g., foraminiferous), and D) microlaminations of clay minerals.



Source: Modified from Barbosa (2007, p. 133)

### 2.1.2 Potiguar Basin

The Potiguar Basin, situated in northeastern Brazil and bordered by the states of Rio Grande do Norte and Ceará, limits to the east by the Pernambuco-Paraíba Basin (marked by the Touros Peak), to the northeast by the Ceará Basin (defined by Fortaleza Peak), and to the south by crystalline basement rocks (Córdoba, 2001; Pessoa Neto et al., 2007).

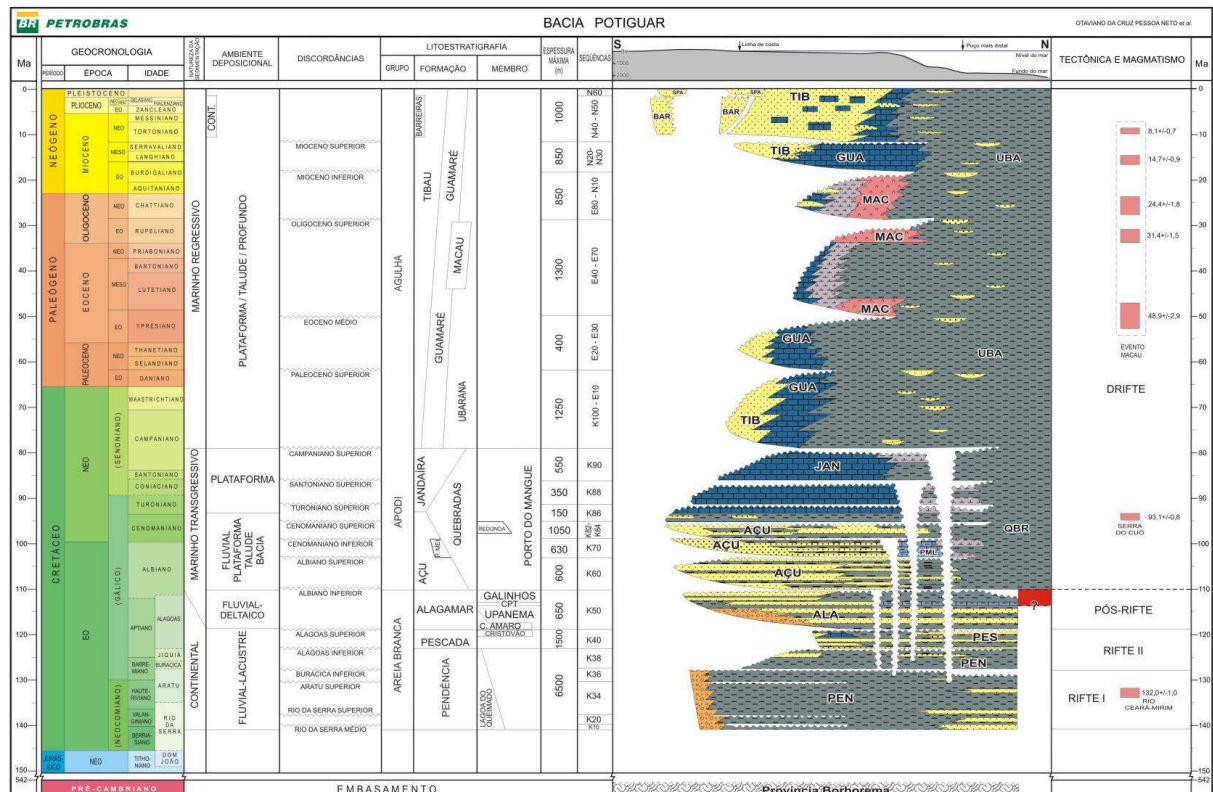
This region is part of the eastern Brazilian equatorial margin, where a series of rift basins formed during the Cretaceous period. These basins originated from crustal stretching that began in the Mesozoic era, leading to the fragmentation of the Gondwana Supercontinent and the subsequent separation of the South American and African tectonic plates. This tectonic process culminated in the formation of the Atlantic Ocean (Araújo et al., 2021; Bertani, 1990 qtd. in Portella and Fabianovicz, 2017; Costa de Melo et al., 2016; de Castro et al., 2012; De Matos, 1992). The rifting of Pangea gave rise to several continental basins, including the Pernambuco-Paraíba, Araripe, Tucano, Rio do Peixe, Jatobá, and Potiguar Basins Córdoba (2001); De Castro et al. (2012) and Pessoa Neto et al. (2007).

According to Bertani (1990), qtd. in Portella and Fabianovicz (2017), the lithostratigraphic units of the Potiguar Basin are related to three major tectonic events: rift, transitional, and drift (see the right side of Figure 11). Pessoa Neto et al. (2007) and Portella and Fabianovicz (2017), classify the lithostratigraphic units of the Potiguar Basin into three main groups: Areia Branca, Apodi, and Agulha.

The Areia Branca Group includes sediments from the Pendência, Pescada, and Alagamar formations, representing a fluvial-deltaic continental phase. The Apodi Group is characterized by the Açu, Ponta de Mel, Jandaíra, and Urbana formations, associated with a marine transgressive phase marked by substantial carbonate deposition. The Agulhas Group signifies the marine regressive phase, comprising clastic and carbonatic rocks from the Ubarana, Guaramaré, Tibau, and Barreiras formations (Córdoba, 2001).



Figure 11 – Stratigraphic column of Potiguar Basin relating the lithostratigraphic units with the depositional system and tectonic events.



Source: Pessoa Neto et al. (2007, p. 369)

### 2.1.2.1 Jandaíra Formation (Turonian–early Campanian)

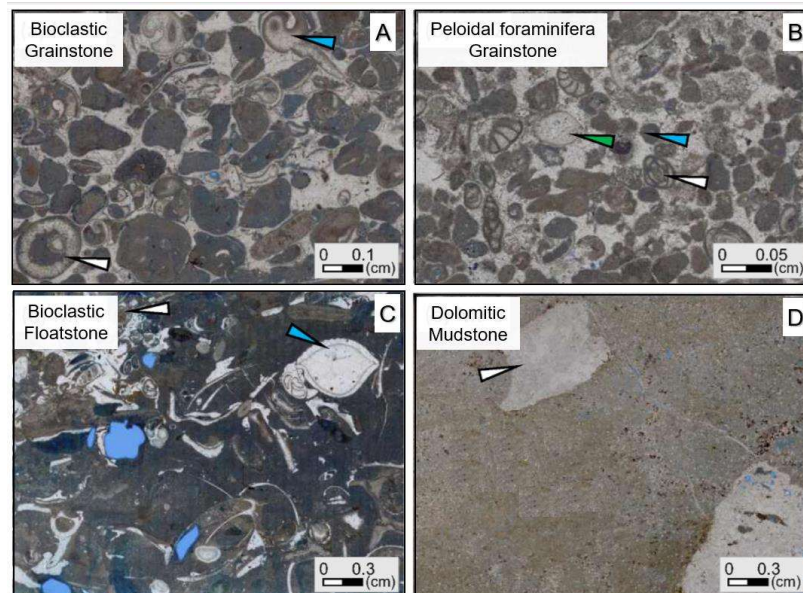
The Jandaíra Formation, deposited during the Turonian to early Campanian, lies above the siliciclastic rocks of the Açu Formation and is overlain by the Barreiras Formation (Córdoba, 2001). Bertani (1990), qtd. in Portella and Fabianovicz (2017), describe the Jandaíra Formation as representing a marine transgressive phase of the Potiguar Basin during the drift event. Córdoba (2001) identified three facies associations related to the depositional systems of the Jandaíra Formation: 1) shallow water, 2) intermediate-depth water, and 3) deeper waters.

The Jandaíra Formation represents a succession of shallow marine sediments formed in a mixed siliciclastic-carbonate ramp (Córdoba, 2001; Miranda et al., 2012). The lithofacies are predominantly composed of bioclastic limestones but also include marls and limestones with siliciclastics. Araújo et al. (2021); Bagni et al. (2022); Córdoba, (2001); and Santos et al. (2015) report that the highest concentration of

fossils in the Potiguar Basin occurred during the deposition of the Jandaíra Formation. This includes planktonic and benthic foraminifera, ostracods, red and green algae, mollusks, echinoids, oolites, peloids, bryozoans, and miliolids.

The Jandaíra Formation features a range of depositional textures, including bioclastic rudstones, grainstones, packstones, floatstones, wackstones, and mudstones, as illustrated in Figure 12A to Figure 12D (Bagni et al., 2022; Córdoba, 2001). Bagni et al. (2022) note that the rocks of the Jandaíra Formation are primarily composed of calcite but also contain silica and dolomite. Dolomite is observed as trace minerals alongside apatite, K-feldspar, and pyrite in subtidal deposits. The study further highlights that grain size, sedimentary structures, cement composition, and the presence of silica and magnesium vary depending on the type of deposit (e.g., subtidal or peritidal).

Figure 12 – Petrographic thin sections of Jandaíra Formation. A) bioclastic grainstone with bivalves, green algae, gastropods, and miliolids. B) peloidal foraminifera grainstone; C) peloidal grainstone with skeletal grains of bivalves and echinoderms; and D) bioclastic floatstone with skeletal grains and echinoderms fragments.



Source: Bagni et al. (2022, p. 6)

## 2.2 ROCK-FLUID INTERACTIONS

Bennion (1999, 2002) defines formation damage as "any process that causes a reduction in the inherent natural productivity of a gas or oil-producing formation or a

reduction in water or gas injection into an injector well." Formation damage can be either reversible or irreversible and may result from mechanical, chemical, biological, or thermal alterations. Bentosa (2010) discusses both controllable and uncontrollable mechanical and chemical factors crucial for understanding changes in oil productivity. Controllable mechanical variables include well trajectory (such as azimuth and inclination), weight, and type of drilling mud. Conversely, uncontrollable mechanical factors encompass the rock's stress state, pore pressure, strength, and elastic properties. Additionally, uncontrollable chemical factors, such as the rock's mineralogy and fluid transport mechanisms, can influence the interaction between rock and fluid.

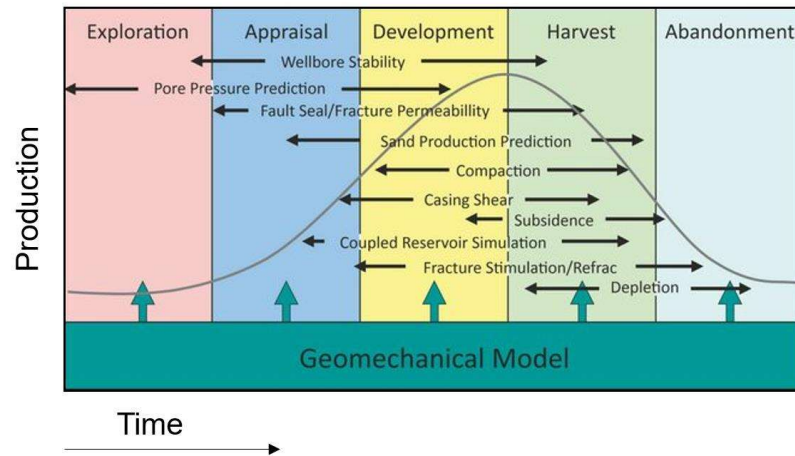
### **2.2.1 Geomechanical alterations**

Geomechanical formation damage refers to the reduction in permeability, particularly near the wellbore, caused by changes in pressure and temperature (Bennion, 2002). Variations in pressure due to tectonic environments and oil/gas production activities affect fluid flow pathways and the properties of rock and fractures, including roughness, stiffness, strength, porosity, hydraulic conductivity, and mineralogy. Fluid production and injection create stress anisotropy, leading to the deformation of the porous and fractured medium.

Advancements in understanding have highlighted the importance of studying geomechanics throughout a reservoir's life to prevent or mitigate decreases in productivity over time. Figure 13 illustrates the various stages of a reservoir's life cycle—exploration, development, production, and abandonment—and the role of geomechanics in each stage.

One reason the oil industry uses geomechanical models is to analyze stress-sensitive reservoirs, aiming to understand changes in permeability over time and space. Nelson (2007) emphasizes the need for interdisciplinary approaches to study the properties of rocks, fractures, geologic media, and fluids, using experimental, numerical, and analytical models to diagnose permeability reductions.

Figure 13 – Importance of the geomechanical model of a reservoir production over time, from exploration until abandonment.



Source: Zoback (2007)

Tovar and Salazar (2007) describe permeability changes due to fluid production as occurring preferentially at the wellbore face because of stress anisotropy. They attribute these changes to the type of rock failure and the petrophysical properties of the rock, particularly its porosity. Rhett and Teufel (1992) explored the relationship between matrix permeability and stress paths through laboratory measurements under real reservoir conditions (non-isotropic). Their research underscores the importance of understanding in-situ stress early in reservoir production and monitoring stress variations by periodically measuring changes in pore pressure. Bin et al. (1995) attribute a decrease in reservoir productivity to stress anisotropy caused by fluid production and the type of rock. They highlight that rock texture, mineralogy, and compaction are directly related to a formation's "stress sensitivity," as mineralogical heterogeneity (e.g., clay minerals) can deform pores and fractures in response to stress variations. Paluszny and Matthai (2008) developed a methodology to calculate the effective permeability of rock (matrix-fracture) using finite element methods. They propose that fracture geometry and aperture are the most influential factors affecting fluid flow variations under stress changes.

Petunin et al. (2011) calculated permeability and porosity in homogeneous and fractured plugs of sandstones and carbonates. They used a modified Carman-Kozeny model, relating permeability to porosity, tortuosity, fracture plane area, and shape factors. Their observations indicate that 1) carbonates exhibit greater stress-



dependent permeability than sandstones, and 2) fractured plugs show a more significant permeability decrease compared to homogeneous plugs. Their research underscores the impact of lithology and rock fracturing on rock and fracture deformability as a function of stress.

Petrographic analysis and X-ray diffraction (XRD) assess the impact of drilling fluid invasion within formations. Kersey (1986) proposed a methodology to characterize and quantify permeability losses in fractures and microfractures. Krueger (1988) observed on a microscopic scale how clay minerals and grain distribution affect rock void spaces and conductivity channels in response to stress alterations from drilling and production. Takahashi and Koide (1995) studied changes in pore size, shape, and orientation due to compaction effects from stress variations.

Al-Harthy et al. (1998); Crawford and Smart (1994) estimated stress anisotropy using “true triaxial test” equipment. In this test, the vertical principal stresses ( $S_v$ ), minimum horizontal ( $S_h$ ), and maximum horizontal ( $S_H$ ) stresses are different ( $S_v \neq S_h \neq S_H$ ), simulating reservoir conditions. They found significant permeability reduction when rocks were subjected to true triaxial stress conditions compared to conventional triaxial conditions in the laboratory ( $S_v \neq S_h = S_H$ ). These studies emphasize the importance of conducting experiments under realistic conditions to validate geomechanical models. Similarly, Bruno; Bovberg; Nakagawa (1991); Holt (1990); McKee; Bumb; Koenig (1988); Oskan (2013); Teufel (1987); Zhang et al. (1999); Zhang et al. (2000) conducted experimental work to understand stress-dependent permeability.

Soares and Ferreira (2002) proposed a methodology for analyzing reservoir deformations resulting from increased effective stresses due to fluid production. This method includes conducting uniaxial tests, measuring permeability, and analyzing S and P waves to identify rock structures in response to changes in wave velocity. Their study identified plastic and elastic zones and stress paths to determine when rock deformation becomes irreversible due to increased effective stress from fluid production. Similarly, Gale (1982) reported irreversible deformability for natural and induced fractures during loading and unloading flow rate-stress cycles. Brittle materials tend to fail suddenly without plastic deformation when stressed. Ductile materials (e.g.,

rocks rich in clay minerals) can experience significant plastic deformation before fracturing. These materials elongate or deform rather than fail immediately, allowing them to absorb energy before failure and making them more resistant to sudden fracture (Beer; Jhonston; Dewolf, 2006; Hibbeler, 2009; Timoshenko and Gere, 1993).

Sijing and Xingtang (1991) mapped natural fracture zones using seismic and geophysical data to qualitatively identify and delimit areas potentially susceptible to geomechanical damage in stress-sensitive reservoirs. Tarrahi, Jafarpour, and Ghassemi (2013) define rock attributes such as permeability, unconfined compressive strength (UCS), cohesion, and Young's Modulus by mapping these properties based on micro-seismic events registered during fluid injection. Their study evaluates rock deformability over time by analyzing spatial changes in the rock's physical properties.

Ostensen (1987) examined how pressure drawdown affects reservoir permeability through core analysis and well-testing data. The researcher reported a 30% reduction in permeability due to stress dependence, emphasizing that production is influenced by the permeability-stress relationship under pressure drawdown conditions. Pinzon; Chen; Teufel (2001) identified diagnostic indicators for categorizing a system as stress-sensitive by determining time-rate-pressure dependency from transient tests, unusual drawdown values, and irregular skin values (i.e., total damage). Bin et al. (1995) compared drawdown and build-up test results, proposing that both tests are necessary and complementary for describing and evaluating permeability variations in a reservoir. Their research highlights a complete dependence of permeability variations on stress.

Geomechanical experiments often involve destructive testing of rock specimens, which can limit data acquisition. To address this, studies have been developed to obtain data without destroying samples. Pan, Hsieh, and Liao (2008) proposed a methodology for obtaining rock mechanical data through numerical simulations, specifically using a block-in-matrix test. They simulated and analyzed the behavior of a matrix of colluvial material (i.e., angular blocks of shale and clay) in relation to the size, shape, and distribution of the clasts. The study found that rock strength, block orientation, and size are key variables affecting the deformability of the deposit in response to stress variations.

#### 2.2.1.1 Geomechanical alterations due to stress variations

To a greater or lesser extent, a fractured reservoir contains multiple sets of inherent fractures, whether induced or natural. These fractures can define the principal pathways for fluids, controlling flow channels and pore pressure distributions. A naturally fractured reservoir under in-situ stress is a system in equilibrium. Drilling the well induces changes in the stress state of the rock (Fjaer et al., 2008). Replacing the rock with drilling fluids further varies the stress near the wellbore, changing the intrinsic properties of the fractured rock and the fluids it contains. This redistribution of stresses can deform the fractures, reducing the fluid flow channels and fracture transmissivity. Understanding the deformability of fractures implies knowing the impact of the physical properties and attributes of fractures in response to alterations caused by anthropogenic processes. Thus, multiple studies have produced analytical, experimental, and numerical models for evaluating fracture permeability performance due to stress variations (e.g., Buchsteiner and Warpinski, 1993; Economides; Buchsteiner; Warpinski, 1994; Jin; Somerville; Smart, 2000; Jones, 1975). These models include principal stresses, effective normal stress, shear stress, and rock and fracture properties (e.g., mineralogy, compressibility, stiffness, frequency, aperture, and closure mechanism).

Goodman (1976), qtd. in Yuting et al. (2000), introduces the term "normal stiffness" of the fracture, describing the variation in the rate of normal stress as a function of the normal displacements. Subsequently, Bandis; Lumsden; Barton, (1983) present experimental studies showing the variation of fracture deformability under normal and shear stresses, suggesting a hyperbolic function to describe the relationship between stress and aperture/closure of the fractures. Rodríguez; Guimarães; Maciel (2022) studied the influence of fracture normal stiffness on its performance during fluid production. The study suggests fractures with low stiffness are sensitive to closure, especially near the well, where stress anisotropy is higher, preventing maximum cumulative production over time.

Rodríguez (2017); Rodríguez and Osorio (2019) propose a methodology to evaluate the impact of fracture orientation and aperture, effective normal stress, and fluid rate on fracture deformability in stress-sensitive systems. They observed the

maximum decrease in fracture permeability at depths where the fracture intersects the well.

Finkbeiner; Barton; Zoback (1997) characterize fractures by core logging and interpretation of conventional logs (e.g., caliper and temperature) to identify potentially open or critically stressed fractures. The model outputs include lithological and morphological characteristics and fracture distribution, analyzing principal stresses on planes of weakness as a function of stress and depth.

Barton; Zoback; Moos (1995) propose a methodology to determine fracture orientations favorable for optimal fluid production as a function of the stress state. Dorta et al. (2001) highlight fracture orientation as the most influential attribute in permeability variations, while Song et al. (1998) suggest structural configuration and rock lithology as the main characteristics determining fracture flow channel frequency, spatial distribution, and interconnectivity.

Safari and Ghassemi (2010) developed a poroelastic fully coupled 3D model to study fracture deformations varying the flow rate. Researchers analyze how changes in pore pressure produce a mismatch between fracture planes, changing the fracture aperture. Similarly, Zhou and Ghassemi (2009) suggest fracture mismatch decreases over time in response to increased pore pressure due to normal stress variations.

The data obtained experimentally are used to calibrate numerical models on larger scales, such as the reservoir scale. Therefore, researchers develop more robust and efficient numerical models to evaluate rock properties and changes in fracture permeability in response to stress variations (Archer, 2008; Bagheri and Settari, 2005; Bai et al., 2002; Baker and Kuppe, 2000; Bertuzzi et al., 1998; Davies, 1999, 2001; Du and Wong, 2002; Farahmand and Diederichs, 2014; Giraldo; Chen; Teufel, 2000; Kasap and Bush, 2003; Min et al., 2004; Ordoñez et al., 2001; Raghavan and Chin, 2004; Yuting et al., 2000). Hosseinian; Rasouli; Bahrami (2010) investigate how to represent fracture morphology in permeability models, developing a numerical and analytical model incorporating synthetic velocity profiles with computational fluid dynamics analysis. They observe that fracture apertures are more sensitive to closure due to stress path variation than their geometry, roughness, or shape. Multu and Pollar

(2006) propose a mathematical algorithm to determine fracture aperture/closure by studying the impact of fracture roughness.

Osorio; Chen; Teufel (1997) coupled a fluid-flow/geomechanical simulator and determined that permeability distribution decreases in a porous medium as production time increases, highlighting that the maximum decrease in fracture permeability occurs near the well. Furthermore, Osorio; Chen; Teufel; Schaffer (1998) studied how Young's modulus controls the permeability behavior of different reservoir rock layers.

Olsson (1992) investigates fluid flow rate changes in an artificial fracture by applying constant normal stress and inducing radial flow during rotary shear, examining fluid flow dependence on shear stress, normal stress, and fracture slip on smooth and rough fracture surfaces. The experiments show that sliding a smooth fracture increases the flow rate by 20%, while further sliding reduces it to less than half of the original value. In contrast, sliding a rougher fracture at constant normal stress rapidly decreases the flow rate to less than 40% of its original rate, with wear being the most important parameter during fracture slip.

Paterson and Olgaard (2000) developed an experimental setup to investigate torsional deformation mechanics, exploring carbonate rocks' rheological characteristics under high temperature and pressure. They suggest that studying axial deformation with torsion reveals variations in the three principal stresses, providing a broader view of strain history on flow stress compared to traditional axial deformation tests, and simulating non-coaxial deformation scenarios observed in complex tectonic regions. Shear tests and rotary shear testing under constant normal stress enhance comprehension of rock joint behavior under underground conditions (Jing and Stephansson, 1995). Studies develop compression-torsion apparatus to measure shear stress and shear strain, studying rock friction during earthquakes (Di Toro et al., 2010), sliding resistance, slip speeds, slip displacements (Rajagopalan and Prakash, 1999), and frictional resistance of the rocks (Yuan and Prakash, 2008).

Xu and Freitas (1988) applied shear displacement of natural and artificial fractures using a rotary shear apparatus to study the shear stress responses of the rock. The shear displacement, calculated from the measured torque, increases when

rock experiences high normal and shear stress, especially on filled fractures. Smooth surfaces experienced rapid and constant deformation at low shear strain, while rough surfaces reached higher shear stress, resulting in irregular deformation.

#### 2.2.1.2 Geomechanical alterations due to acidizing

Several studies have reported that acidizing treatments can significantly affect the petrophysical and mechanical properties of carbonate rocks, including Young's modulus, Poisson's ratio, cohesion, uniaxial compressive stress (UCS), and friction angle, as described below:

Oliveira et al. (2020) explored the behavior of shear strength in carbonate rocks subjected to chemical variations by applying an HCl solution to Brazilian carbonate rocks. The study found that chemical dissolution of the rock alters cohesion, friction angle, roughness coefficient, and shear strength, as reactive fluids impact the rock's porosity. The loss of calcium minerals due to acid attacks plays a key role in these strength changes.

Galindo et al. (2021) created synthetic carbonate rocks to conduct their experiments. These artificial rocks, which have petrophysical and geomechanical properties similar to natural carbonate rocks, revealed that prolonged contact with acid under constant vertical stress (oedometric conditions) induces vertical strain in the sample. Chemical dissolution weakens the rocks, leading to increased effective horizontal stress over time and reduced rock strength due to variations in its elastic domain. Alameedy et al. (2023); Liang et al. (2023); McGuire; Elsworth; Karcz (2011) describe how changes in acid exposure time and the pH of solutions induce mechanical degradation of the rocks such as elastic properties and hardness. The authors show that the stress state impacts rock changes during matrix acidizing.

Alameedy et al. (2022) investigated the effects of acid treatments on the geomechanical properties of carbonate rocks by integrating results from acid core-flood experiments, computed tomography, and measurements of mechanical and petrophysical properties using acoustic velocities. The presence of acid modifies the rock's compressibility, leading to decreased Young's modulus and increased Poisson's

ratio. Mustafa et al. (2022) studied the behavior of chalk, limestone, and dolomite rocks under various acid injection rates, using acoustic measurements, XRD tests, hammer techniques, and numerical simulations to assess mineralogy, hardness, Young's modulus, and Poisson's ratio in the formation of wormholes due to acidizing. They observed that rock hardness decreased by 47-77% after acidification, while Young's modulus was reduced by 33%. Lai et al. (2022) expose a reduction trend in hardness and Young's modulus after acidizing depending on the acid concentration.

Parandeh et al. (2023) examined the effects of hydrochloric acid injection on Young's modulus and UCS under different loading conditions. Their experiments varied the concentration of the HCl solution and acid injection rate. Findings indicated that significant changes in rock strength occurred primarily during the initial contact with acid, where dissolution is most intense.

Nino-Penaloza et al. (2015) investigated the impact of fracture topography characteristics on Austin Chalk and San Andres dolomite rocks during acidizing. They found that fracture conductivity resulting from acidizing is influenced by several factors, including acid injection rate, temperature, rock-acid exposure time, and rock texture. The study reported a decrease in rock strength of approximately 12% and 30% for acid-rock exposure times of five and ten minutes, respectively.

Gong and Lacote (1998); Hassan et al. (2022) examined the behavior of fracture conductivity due to acidizing, considering factors such as surface roughness, acid injection rate, mechanical properties of the rock, and contact time between acid and rock. Their research indicated that prolonged contact between rock and acid increases roughness and enhances conductivity. However, the presence of acid decreases the rock's compressive strength, leading to the deformation of asperities under stress and potential fracture closure.

### **2.2.2 Chemical alterations on carbonate rocks**

Ng and Santamarina (2022) suggest that combining depositional environments with processes such as compaction, dissolution, and recrystallization can alter the micro-scale properties of carbonate rocks. These changes affect pore size, fabric, and

grain heterogeneity, which in turn influence fracture roughness, rock brittleness, and strength.

Wayne (2008) discusses how diagenetic processes in carbonates can modify biogenic constituents, mineralogy, and texture, particularly in the presence of reactive fluids. Mumallah (1996) categorizes the effects of acid on carbonate rock into two types: (1) uncontrolled variables, such as intrinsic rock properties like permeability, porosity, fabric, and texture, and (2) controlled variables, including acid concentration, pH, system pressure, and injection rate. The study emphasizes that fluid dynamics and flow channel configurations impact not only fracture properties but also hydro-mechanical and chemical effects during production, injection, and stimulation.

Engineers have developed stimulation treatments to address fracture deformability, maintain open fractures, remove damage, and enhance productivity. For example, acid fracturing involves injecting acid into pre-existing fractures to increase fracture aperture through the dissolution of carbonate minerals. This chemical dissolution etches the fracture walls, facilitating fluid flow even when fractures close due to pressure drawdown. Xiao et al. (2020) describe acid-etched fracture patterns as a function of dissolution rates and different HCl concentrations. Higher HCl concentrations lead to significant morphological differences, such as deep pits primarily at the contact points between the rock and acid injection. Several authors report common etching patterns, including irregular roughness, channels, uniform textures, tensile features (Neumann et al., 2012), and turbulence (Pournik et al., 2009).

Gou et al. (2021) investigate the effects of acid fracturing on fracture morphology and conductivity, concluding that acid smoothing strengthens the peaks of fractures more than the valleys. The study shows significant improvements in conductivity after two cycles of acid fracturing due to etching patterns that favor fluid flow. Conductivity is higher in fractures with pre-existing roughness. Asadollahpour et al. (2018) analyze hydraulic conductivity improvements in response to acid on rough fracture surfaces of limestone, finding that fractures with initial roughness exhibit higher etching patterns and greater rock dissolution. Chemical dissolution creates mismatches between fracture faces, increasing fracture aperture in some cases and enhancing fracture



conductivity. Similarly, Neumann et al. (2012) suggest that mismatched surfaces increase acid conductivity.

Al-Momin; Zhu; Hill (2014) demonstrate that acid creates etching patterns that improve conductivity more on rough surfaces than on smooth ones. Chen et al. (2021) find that fracture conductivity increases on rough surfaces because the acid penetrates deeper zones and smooths high points, creating a fracture plane mismatch that enhances fluid conductivity at low closure stress. The authors also note that increasing the acid injection rate results in higher dissolution and roughness on previous fracture surfaces. Dong; Hill; Zhu (1999) report that fracture etching patterns due to acidizing are directly related to the initial fracture aperture, with larger initial apertures producing deeper and wider channels. Conversely, small initial apertures reduce the size of channels on rough surfaces. Mou; Zhu; Hill (2010) describe fracture etching patterns as strongly dependent on mineralogy and roughness distribution on the fracture surface.

Nino-Penaloza et al. (2015) studied the effects of texture on acid-etching patterns using samples with rough and smooth surfaces. Acid treatment generates roughness in both types of surfaces: irregular etching in smooth surfaces and deepening cavities in rough ones. Acid-etching roughness increases conductivity in both cases, but asperities that keep fractures open deform more easily during loading in low-stress rocks. Wu; Szabian; Sharma (2020) investigate the effects of acid-etching on fracture morphology, conductivity, and mechanical properties in shales (composed of 3-75% clay and 2-83% carbonate). The study classifies samples by roughness ( $>0.006$  mm for low roughness and  $>0.043$  mm for high roughness). Conductivity improves more in high-roughness samples than in low-roughness ones. Roughness increases after acidizing in carbonate-rich samples, but this increment is not always related to high carbonate content. The distribution of carbonate minerals affects fracture topography after acidizing, creating isolated pits in low-roughness samples and small channels in high-roughness samples. The study also suggests that the loss of carbonate minerals due to dissolution decreases rock hardness.

Hassan et al. (2022) evaluate how rock hardness and roughness affect conductivity improvements due to acid treatments. They attribute rock hardness to

elemental composition: rocks with 90 wt% calcite are weaker, while those with 95% dolomite are harder. Results show higher conductivity in weaker samples because HCl injection etches the surface more easily compared to harder samples. Lai et al. (2019) suggest that rocks with high mechanical properties exhibit high conductivity even with prolonged acid exposure. They describe prolonged contact time between acid and rock at low closure stress as leading to high dissolution and consequently high conductivity. Additionally, conductivity is high at high closure stress for short contact times, even with low mass dissolution. Al-Momin; Zhu; Hill (2014) note an optimal contact time for acid and rock; extending the contact time does not significantly change fracture conductivity when injecting the same quantity of acid (Pournik et al., 2007).

Jin et al. (2020) developed an experimental setup to evaluate acid fracturing efficiency on rocks with homogeneous and heterogeneous mineralogy and grain distribution. Heterogeneous samples, containing insoluble minerals like clays and quartz distributed in the flow direction, favor fluid flow and maintain fracture openness even under high closure stress. In contrast, homogeneous samples show significantly reduced fracture conductivity at high closure stress. The authors conclude that conductivity enhancement due to acidizing is optimized when insoluble minerals align with the flow direction. Guo et al. (2017) describe that roughness after acidizing increases to varying degrees depending on the position between the fracture plane and the bedding plane (i.e., perpendicular roughness is higher than parallel). The presence of carbonate minerals also promotes acid-etching roughness in both directions. Jia et al. (2017) study hydraulic aperture evolution and roughness variations as a function of pH, noting that acid pH removes calcite, leaving quartz as the principal rock constituent. The dissolution of calcite results in high etching roughness and increased fracture aperture.

Numerical models often accompany experimental data to calibrate simulations studying acid etching patterns (Dong; Zhu; Hill 2001, 2002), propose fracture conductivity correlations as a function of normal and shear stress (Deng; Mou; Hill 2011; Zhang; Jin; Zhu 2018), account for asperities (Lacote, 1999), couple stress and fluid transport mechanisms (Gou et al., 2021), and develop machine learning techniques (Hassan, Tariq, Al-abdrabalnabi, et al., 2022).

Cardona; Finkbeiner; Santamarina (2021) developed acidification experiments by injecting an HCl solution into a limestone fractured with a smooth surface. The acidizing process increased fracture transmissivity, with minimal changes in the fracture's vertical displacement. The authors suggest that acid acts preferentially, smoothing high points while keeping the actual contact fracture area largely unaltered. Cardona (2020) describes a reduction in fracture transmissivity in response to axial loading when the asperity wavelength is longer (indicating greater roughness).

## CHAPTER 3 – THEORETICAL FRAMEWORK

This chapter includes definitions and concepts about the nature of carbonate and fracture characteristics. The theoretical framework outlined here provides the basis for understanding the concepts used in the development of this research.

### 3.1 CARBONATE ROCKS

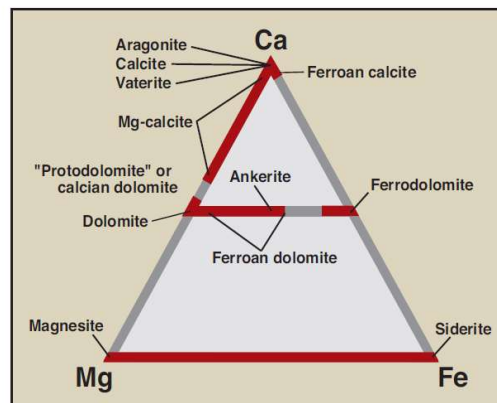
Inorganic compounds formed from the ionic bonding of the anion  $(CO_3)^{2-}$  and metallic cations such as Ca, Fe, Mg, Zn, Mn, Sr, and Cu are chemically defined as carbonates. The bond between the carbonates and the metallic cation is not as strong as the internal bond within the carbon trioxide ( $CO_3$ ). The internal structure of carbonates breaks down in the presence of hydrogen ions, producing carbon dioxide ( $CO_2$ ). This reaction, which produces fizz when acid comes into contact with carbonate rock, distinguishes carbonates from noncarbonates (Wayne, 2008). The fizz is a characteristic feature of carbonate rock and helps differentiate them. Notably, dolostones fizz less in the presence of acid compared to limestones. Limestone is a carbonate rock composed mainly of calcium carbonate, while dolostone is rich in dolomite. Carbonate rocks with mixed terrigenous mud and fine-grained calcite are called marl.

Carbonate rocks result from large accumulations of fossils, microorganisms, biota, and inorganic particles. Chilingar; Bissell; Fairbridge (1967) describe carbonate rocks as sedimentary rocks composed of biochemical, chemical, and clastic components. The dominant cations in the most common carbonate rocks are  $Ca^{2+}$ ,  $Mg^{2+}$ , and  $Fe^{2+}$  (Figure 14 **Erro! Fonte de referência não encontrada.**). Scholle and Ulmer-Scholle (2005) explain that carbonate rocks are primarily composed of one or two carbonate minerals (mainly calcite and dolomite) with various other minerals such as silica, detrital grains, phosphate, glauconite, and evaporite.

Calcium carbonate originates from the dissolution in seawater and freshwater. Acidic water controls the dissolution of calcite and dolomite. Calcium is present due to weathering of rocks formed by calcium-rich minerals, such as plagioclase. The calcium dissolved in seawater allows reef-building and marine organisms to use calcium

carbonate to create their skeletal parts. Carbonate precipitation favors the formation of reefs in tropical and subtropical areas with warm water. The dissolution of carbonate rocks produces karst, caves, depressions, underground channels, and fluid conduits. These channels can cover large areas and connect fractures, enhancing the fluid flow of a reservoir.

Figure 14- Ternary diagram of the general compositions of the full spectrum of carbonates.



Source: Scholle and Ulmer-Scholle (2005, p. 8)

Carbonate rocks have unique characteristics that distinguish them from siliciclastic rocks. Wayne (2008) summarizes the differences: (1) carbonate rock deposition, mineralogy, and texture are associated with detrital, chemical, and biological processes, while siliciclastic rock deposition is related to a parent rock and fluvial transport; (2) biological activity influences the composition and shape of these rocks since carbonates are mainly composed of biogenic constituents. Biogenic constituents "consume" the particles and grains of the rock, modifying the shape and size of the void space. Additionally, boring and burrowing organisms may affect the stratification and extent of the rock mass; (3) components of carbonate rocks are susceptible to modification by diagenetic processes such as dissolution, recrystallization, and cementation, among others.

### 3.1.1 Diagenesis in carbonate rocks

Diagenesis processes refer to the physical, chemical, and biological changes that occur in carbonate rocks after their initial deposition but before they reach the stage of metamorphism (Morrow and McIlreath, 1990, qtd. in Córdoba, 2001). Diagenesis

involves the transformation of particles and sediments into solid rocks, affecting rock texture, mineral composition, porosity (Eberli et al., 2003), and permeability. Tucker; Wright; Dickson (1990) as well as Tucker and Bathurst (1990), describe six principal diagenetic processes:

a) Micritization: This process produces fine-grained, microcrystalline carbonate particles called micrite. It involves the alteration of skeletal fragments, ooids, or other carbonate grains into micrite through chemical processes. Micrite formation often occurs in pore spaces and can contribute to cementation.

b) Cementation: Cementation occurs when pore fluids are supersaturated, causing carbonate minerals to precipitate and fill the void spaces between grains, binding them to form a rock with high cohesion and strength.

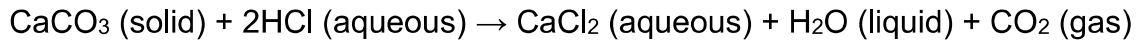
c) Neomorphism: This process includes recrystallization and substitution. Substitution occurs when a more stable mineral with the same chemical composition replaces the original mineral. Recrystallization involves the replacement of smaller crystal sizes with larger ones.

d) Dolomitization: Dolomitization is the replacement of calcium carbonate minerals (usually calcite) with dolomite ( $\text{CaMg}(\text{CO}_3)_2$ ). This can occur through several mechanisms, such as the introduction of magnesium-rich fluids, evaporation, and thermal effects, significantly altering the rock's mineralogy.

e) Compaction: Diagenesis begins with the deposition of carbonate sediments, which over time become compacted under the weight of overlying layers, leading to the expulsion of pore water and reduction of pore space.

f) Dissolution: Dissolution involves the gradual chemical removal of carbonate minerals from the rock matrix due to acidic fluids, creating voids or cavities within the rock, often increasing porosity and permeability.

A classic example of an acid-base reaction is the chemical interaction between calcite ( $\text{CaCO}_3$ ) and hydrochloric acid (HCl), as demonstrated by the following reaction (Lund et al., 1975):



This reaction illustrates the dissolution of calcium carbonate in hydrochloric acid, producing soluble calcium chloride, water, and carbon dioxide. The characteristic effervescence is due to the release of carbon dioxide gas, which is the basis for the dissolution of calcite-based materials.

### **3.1.2 Properties of a carbonate rock reservoir**

The porosity and permeability of carbonate rocks result from various processes that define the rock properties characterizing a reservoir. Wayne (2008) identifies fabric, grain type, texture, mineralogical composition, and sedimentary structures as key properties of carbonate rock reservoirs, providing insights into rock formation and diagenesis to predict fluid flow. Key properties include (Chilingar; Bissell; Fairbridge 1967; Dunham, 1962; Scholle and Ulmer-Scholle, 2005; Wayne, 2008):

a) Texture: The texture of a carbonate rock refers to the arrangement and characteristics of mineral grains and the size of the matrix and particles within the rock. Grain size can vary significantly, from fine-grained (microcrystalline) to coarse-grained (macrocrystalline), affecting the rock's appearance and porosity.

b) Sorting: Sorting refers to the uniformity in grain size within a rock. Well-sorted carbonate rocks have grains of relatively uniform size, while poorly sorted rocks have a wide range of grain sizes, impacting porosity and permeability.

c) Pore Space: Texture reveals the distribution and type of pore spaces, including primary pores formed during sedimentation and secondary pores created during diagenesis. Texture indicates pore connectivity and the types of cement filling the pores.

d) Fabric: Fabric refers to the orientation and relationships between mineral grains. It can range from well-developed crystal orientations (fabric-selective) to random arrangements, impacting the mechanical properties and anisotropy of the rock.

e) Type of Grains (Bioclasts and Fossils): The presence and distribution of fossils and bioclasts provide valuable information about the depositional environment and rock evolution.

f) Matrix: Some carbonate rocks contain a matrix material between mineral grains, composed of fine-grained carbonate material, clay, or silica. The nature and abundance of the matrix influence the rock's porosity and permeability.

### **3.1.3 Carbonate rock classifications**

Carbonate rocks are commonly classified based on observable features that group the rocks into categories. The objective of these classifications is to group rocks by their characteristics to reflect genetic attributes and understand mechanisms of formation, environments of deposition, and similar factors.

Geologists and sedimentologists have proposed numerous classifications to categorize carbonate rocks and comprehend their characteristics and depositional environments. However, Scholle and Ulmer-Scholle (2005) suggest that the classifications by Folk (1959/62) and Dunham (1962), along with others that represent variations of the Dunham scheme, are the most common and useful. These classifications propose to classify carbonate rocks based on 1) the type of grains (e.g., skeletal fragments, ooids, pellets/peloids, intraclasts, and non-carbonate detritus); 2) the presence of carbonate mud or matrix; and 3) the nature of the pores (whether open or filled).

#### **3.1.3.1 Classification of Folk (1962)**

The Folk classification focuses on the composition and texture of carbonate rocks. It categorizes carbonate rocks based on their grain type and the respective quantity of grains (allochems), cement, pore space, or matrix (Scholle and Ulmer-





Figure 17 represents the third component of the Folk classification, which is used to describe the grain or crystal size of the rock. This diagram presents a scale of the grains and transported constituents of the carbonates, such as pellets, ooids, intraclasts, and fossils.

Figure 17 – Scale of grains and crystals in a carbonate rock, proposed by Folk, 1962.

	Transported Constituents	Authigenic Constituents	
64 mm	Very coarse calcirudite	Extremely coarsely crystalline	4 mm
16 mm	Coarse calcirudite		
4 mm	Medium calcirudite		
1 mm	Fine calcirudite	Very coarsely crystalline	1 mm
0.5 mm	Coarse calcarenite	Coarsely crystalline	0.25 mm
0.25 mm	Medium calcarenite		
0.125 mm	Fine calcarenite		
0.062 mm	Very fine calcarenite	Medium crystalline	0.062 mm
0.031 mm	Coarse calcilutite	Finely crystalline	0.016 mm
0.016 mm	Medium calcilutite		
0.008 mm	Fine calcilutite	Very finely crystalline	0.004 mm
	Very fine calcilutite	Aphanocrystalline	

Source: Scholle and Ulmer-Scholle (2005, p. 285)

### 3.1.3.2 Classification of Dunham (1962)

The Dunham classification primarily categorizes carbonate rocks based on their texture and the proportion of allochems (grains) relative to matrix content. Figure 18 illustrates Dunham's classification scheme, which includes the following major categories (Dunham, 1962):

- Grainstone: Composed predominantly of well-sorted carbonate grains, such as sand-sized fragments of shells, skeletal material, or ooids. It typically has a high proportion of grains with little to no matrix.
- Packstone: Contains a mixture of carbonate grains and a matrix of fine-grained material. It often includes recognizable fossil fragments and has a variable grain-to-matrix ratio.

- Wackestone: Exhibits a higher proportion of matrix than grains, featuring a mix of carbonate grains, often microcrystalline, and matrix. Fossils are generally not as distinct as in Packstone.
- Mudstone: Consists mostly of fine-grained matrix with few, if any, discernible carbonate grains. It lacks well-defined grain boundaries and is often microcrystalline.
- Boundstone: A special category emphasizing the presence of bound or encrusted organisms, such as corals or algae, as the primary framework builders. It can be found within other categories (e.g., boundstone-wackestone).



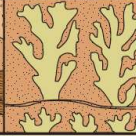
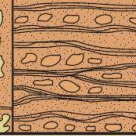
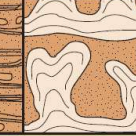
Figure 18 – Classification of sedimentary texture for carbonate rocks proposed by Dunham, 1962.

DEPOSITIONAL TEXTURE RECOGNIZABLE					DEPOSITIONAL TEXTURE NOT RECOGNIZABLE
Original Components Not Bound Together During Deposition				Original Components Bound Together During Deposition	
Contains mud			Lacks mud and is grain-supported		
Mud-supported		Grain-supported			
< 10% grains	> 10% grains				
Mud-stone	Wacke-stone	Packstone	Grain-stone	Boundstone	Crystalline carbonate  (Subdivisions based on texture or diagenesis)

Source: Scholle and Ulmer-Scholle (2005, p. 287)

Figure 19 shows the Embry and Klovan (1971) classification, which builds on Dunham's 1962 scheme. In this classification, the term "floatstone" replaces Dunham's "packstone," and the designation "rudstone" is introduced for coarser, grain-supported biogenic limestones. Additionally, when describing an organically bound rock, it can be referred to as a "bafflestone," a "bindstone," or a "framestone," depending on the nature of the organic structures. These latter three terms, in particular, have gained widespread acceptance among researchers working on reefs, bioherms, and other biogenic carbonate formations.

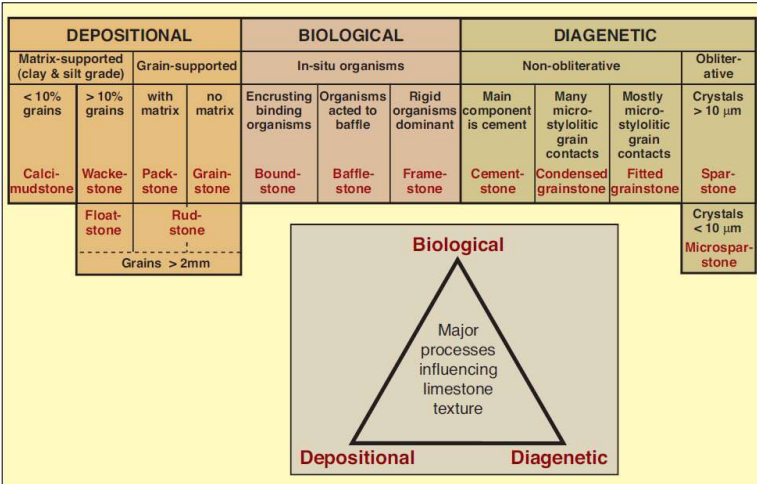
Figure 19 - The Embry and Klovan (1971) classification modified from the Dunham scheme.

Original Components Not Organically Bound During Deposition		Original Components Organically Bound During Deposition		
> 10% grains >2 mm		Organisms acted as baffles	Organisms encrusted and bound	Organisms built a rigid framework
Matrix- supported	Supported by components larger than 2 mm			
Floatstone	Rudstone	Bafflestone	Bindstone	Framestone
				

Source: Scholle and Ulmer-Scholle (2005, p. 287)

Figure 20 illustrates the fundamental elements of Wright's (1992) classification, underscoring the differentiation between carbonate strata and the influence of depositional mechanisms (physical), biological activities, and diagenetic processes. This classification includes terms like "cementstone," "condensed grainstone," and "fitted grainstone," which describe limestone types enriched in cement or chemically compacted.

Figure 20 - The Wright (1992) classification modified from the Dunham, Embry-Klovan previous classifications.



Source: Scholle and Ulmer-Scholle (2005, p. 287)

### 3.1.3.3 Dependent properties of carbonate rocks

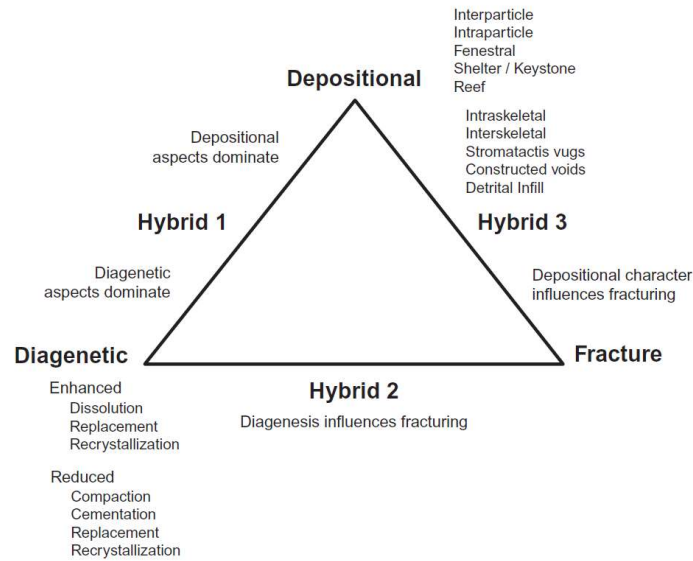
Wayne (2008) discussed that the permeability, porosity, and bulk density of carbonate rocks are derived from their fabric, texture, and mineralogical composition. Consequently, permeability and porosity are important properties that characterize the capacity to store hydrocarbons and the quality of geological reservoirs.

#### 3.1.3.3.1 *Porosity in carbonate rocks*

Porosity is the percentage of open spaces or voids within the rock's structure. In carbonate rocks, these voids result from various factors, including the dissolution of minerals, the presence of pore spaces between grains, and the development of fractures and cavities due to geological processes. There are two primary types of porosity in carbonate rocks (Chilingar; Bissell; Fairbridg 1967; Chilingarian; Mazzullo; Rieke 1992; Lucia, 2007): primary porosity and secondary porosity. Primary porosity originates during the initial deposition and lithification of the carbonate sediment and includes interparticle porosity, which refers to spaces or gaps between individual carbonate grains such as ooids, peloids, and skeletal fragments, and intraparticle porosity, which indicates internal pores such as the internal chambers within bivalve shells. Secondary porosity develops after the rock has formed due to various processes, such as dissolution porosity, which occurs when acidic fluids expose carbonate minerals; as groundwater or hydrocarbons flow through the rock, they can dissolve portions of the mineral matrix, creating voids and enhancing porosity. Dissolution porosity is often responsible for creating caves and karst landscapes in carbonate formations (Fjaer et al., 2008). Fracture porosity results from tectonic forces, stress, and other geological processes that form fractures and faults in carbonate rocks, serving as conduits for fluid migration and storage, and increasing the overall porosity of the rock. Vug porosity refers to irregularly shaped cavities or voids that form within carbonate rocks due to dissolution or other processes.

Wayne (2008) proposes a classification for carbonate porosity based on their genetic processes. Figure 21 presents a classification of carbonate porosity resulting from three principal genetic events: deposition, diagenesis, and mechanical fracturing.

Figure 21 – Ternary diagram of a genetic classification for porosity in carbonate rock.



Source: Wayne (2008, p. 43)

#### 3.1.3.3.2 Permeability in carbonate rocks

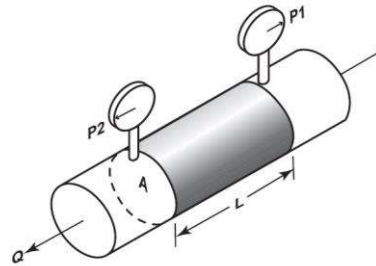
Darcy's law, a fundamental principle in fluid dynamics, describes how fluids flow through porous media and defines permeability. In 1856, Henry Darcy conducted experiments by filling a cylinder with sand and gravel and passing water through the column to measure the flow rate. These experiments were conducted under atmospheric pressure conditions, focusing on the impact of the textural characteristics of the material.

Figure 22 shows the laboratory setup, modified from Darcy's experiments, used to measure permeability in reservoir rock samples. A sample with a length ( $dL$ ) and cross-sectional area ( $A$ ) is fully saturated with a fluid of dynamic viscosity ( $\mu$ ). The fluid flows through the length  $dL$  of the rock sample at a specified rate, represented as  $Q$ . Steady-state conditions are maintained throughout the experiment, with the upstream pressure denoted as  $P$  and the downstream pressure as  $(P - dP)$ . In Equation (1) in Wayne (2008),  $k$  denotes the permeability coefficient and refers to rock properties.

$$\frac{Q}{A} = \frac{k}{\mu} \frac{dP}{dL} \quad (1)$$



Figure 22 – Equipment, modified from Darcy apparatus, to measure permeability as a function of fluid viscosity and pressure.



Source: Wayne (2008, p. 45)

From Darcy's law, permeability could be expressed in units of Darcy or millidarcy (mD),  $\text{cm}^2$ ,  $\text{m}^2$  ( $K_I$ ). Or alternatively Darcy's velocity in [m/s] or its equivalents ( $K_G$ ). Equation (2) denotes the relation between  $K_I$  and  $K_G$ .

$$K_I = \frac{\mu}{\rho g} K_G \quad (2)$$

where  $\rho$  corresponds to the fluid density, and  $g$  represents gravity.

According to North (1985) qtd. in Wayne (2008) carbonate reservoir permeability can be qualitatively classified as poor to fair (<1-15 mD), moderate (15-50 mD), good (50-250 mD), very good (250-1000), excellent (>1000). It is important to note that these permeability classifications serve as general guidelines rather than strict rules, and actual permeability may vary depending on specific conditions and factors.

The permeability of rocks can vary according to their texture and fabric. Wayne (2008) explains that carbonate permeability depends more on the geometry of the pore throats than on the dimensions of the larger pores. For instance, narrow, poorly connected throats can restrict fluid flow even if the pores are large. Natural fractures and vugs (i.e., larger voids) can enhance permeability by providing additional pathways for fluid flow. However, their contribution depends on the extent and connectivity of these features. The size and uniformity of the grains that make up the rock can influence permeability. Well-sorted rocks with uniform grain sizes tend to have higher permeability compared to poorly sorted rocks with a wide range of grain sizes.

Diagenesis processes, such as compaction, recrystallization, and cementation, can significantly affect carbonate permeability. For example, cementation can reduce permeability by filling pore spaces and throats.

## 3.2 NATURAL FRACTURES

Stearns (1990) qtd. in Aguilera (1995) describes a natural fracture as a macroscopic planar discontinuity caused by stresses exceeding rock strength. Nelson (2001) describes a fractures as a macroscopic planar discontinuity of the rock that occurs naturally due to physical deformation or diagenetic processes.

A naturally fractured reservoir contains multiple sets of inherently created fractures. All reservoirs contain fractures to a greater or lesser extent. Fractures define the pathways for fluids, controlling fluid flow and pore pressure distributions. The fracture's geometry, orientation, aperture, density, stiffness, and roughness all impact the hydraulic transmissivity of the rock mass (Aguilera, 2003; Bandis; Lumsden, 1983; Nelson, 1979; Rodríguez, 2017).

### 3.2.1 Fracture properties

Some properties of fractures relevant to this research:

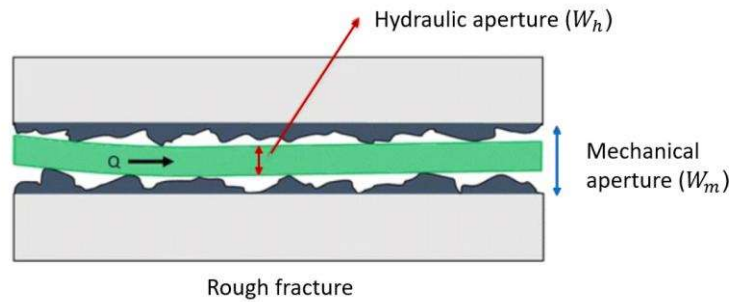
#### 3.2.1.1 Fracture aperture and morphology

The fracture aperture refers to the distance between two fracture planes, also known as the mechanical aperture. According to Nelson (2001), fracture aperture is measured perpendicularly to the direction of the fracture plane. The morphology of a fracture determines whether it is open or filled with mineralized material. The presence and characteristics of this filling material affect the rock's strength and the mechanical properties of the fractures. Suárez (1998) outlines several characteristics of the filling material that impact the strength of a filled fracture, including mineralogy, gradation, grain size, water content, permeability, roughness, fracture intensity, degree of weathering, and expansive potential.



The mechanical aperture ( $W_m$ ) is a physical measurement of the real separation between fracture surfaces, while the hydraulic aperture ( $W_h$ ) represents the effective aperture for fluid flow. Figure 23 illustrates a schematic representation of both the hydraulic and mechanical apertures of a fracture.

Figure 23 – Representation of a hydraulic and mechanical apertures of a fracture with flow through it.



Source: Ghoochaninejad; Asef; Moallemi (2018, p. 144)

Researchers have developed various models through experiments and numerical simulations to estimate fracture aperture. Cardona (2020) provides a summary of empirical and theoretical models for calculating hydraulic aperture based on statistical parameters (see Table 1). Additionally, Table 1 includes models that relate aperture to normal and shear stress, as well as the rock's elastic and strength properties, as compiled by (Rodríguez, 2017).

Table 1 – Fracture aperture models from the literature

Model	References
$\frac{W_h^3}{\mu_G^3} = \left( \frac{\mu_G / \mu_m}{JRC^{2.5}} \right)^3$	Barton; Bandis; Bakhtar (1985); Esaki et al. (1999); Giacomini et al. (2008)
$\frac{W_h^3}{\mu_G^3} = \frac{1}{1 + A_H \left( \frac{2\mu_G}{s_G} \right)^{1.5}}$	Lomize (1951) qtd. in Cardona (2020); Brown (1987)
$\frac{W_h^3}{\mu_G^3} = \left( 1 - C_H e^{-B_H \left( \frac{\mu_G}{s_G} \right)} \right)$	Partir and Cheng (1978) qtd. in Cardona (2020)
$\frac{W_h^3}{\mu_G^3} = \frac{\mu_G (1 - c)}{s_G (1 + c)}$	Brown (1987)
$\frac{W_h^3}{\mu_G^3} = (1 - 2c)$	Li et al. (2008)
$\frac{W_h^3}{\mu_G^3} = \left[ 1 - 1.5 \left( \frac{s_G}{\mu_G} \right)^2 \right] (1 - 2c)$	Chen et al. (2017); Zimmerman and Bodvarsson (1996)

$\frac{W_h^3}{\mu_G^3} = (1 + 3(1 - 3\alpha)S^2 + \dots);$ $S = \frac{S_G}{\mu_G}; \alpha = \int \frac{\theta(\kappa)}{2\pi^2} d\kappa$	Inoue and Sugita (2003) qtd. in Cardona (2020); Auradou (2009)
$W_{0\text{Lei}} = \frac{\text{JRC}}{\sigma} \left( 0.2 \frac{S_c}{\text{JCS}} - 0.1 \right);$ $W_{\text{Lei}} = W_{0\text{Lei}} - \frac{1}{\frac{1}{V_m} + \frac{K_{n0}}{\sigma_n}}$	Lei et al. (2014)
$W_{\text{Zob}} = \frac{2(p_f - \sigma_{\min})L_f(1 - v_f)}{E}$	Zoback (2007)
$W_{\text{Rong}} = \frac{(1 - A_{\text{rong}})(1 - B_{\text{rong}})}{(1 - A_{\text{rong}}B_{\text{rong}})} W_0$ $A_{\text{rong}} = 1 - e^{\left(-\frac{\sigma_n}{\lambda + 2G}\right)};$ $B_{\text{Rong}} = 1 - e^{\left(\frac{1}{2G}\right)\left[\left((\tan^{-1}(\tau_s/S_{\text{Rong}}) - (\varphi_b)) * ( \tau_s ) - \left(\frac{S_{\text{Rong}}}{2}\right)(\ln(1 + ( \tau_s ^2/S_{\text{Rong}}^2)))\right)\right]}$	Rong et al. (2013)

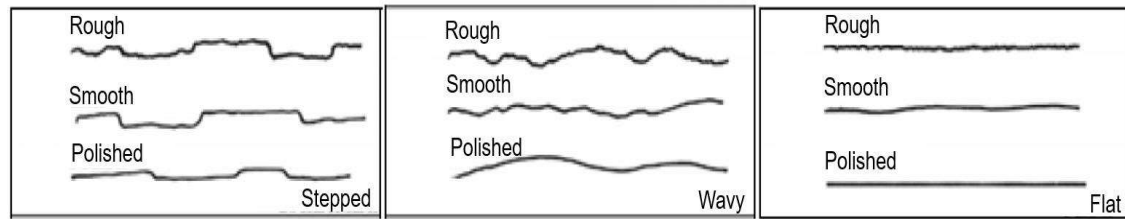
Source: Cardona (2020, p. 84); Rodríguez (2017)

### 3.2.1.2 Fracture roughness

Fracture roughness refers to the surface texture or the set of irregularities and asperities on a fracture surface (see Figure 23). Each fracture plane has a corresponding surface, and each surface exhibits unique roughness characteristics. The contact between two fracture surfaces can vary depending on the type of roughness, ranging from fully mated to unmated. Rougher surfaces create tortuous pathways, which increase frictional resistance to fluid flow, while smoother surfaces allow for faster fluid movement. Irregularities on the surfaces can cause variations in flow direction and velocity, affecting fluid distribution ((Thomas, 1999).

Hoek (1981), as cited in Camacho et al. (2009), categorizes the contact between two fracture surfaces into several types: discontinuous, stepped-rough, stepped-smooth, stepped-perfectly smooth (polished), wavy-rough, wavy-smooth, wavy-perfectly smooth (polished), flat-rough irregular, flat-smooth, flat-perfectly smooth (polished), and filled, which indicates no contact between the fracture planes (see Figure 24).

Figure 24 - Descriptive scale for roughness, proposed by Hoek-1981.



Source: Modified from Camacho et al. (2009, p. 61)

#### 3.2.1.2.1 Characteristics of surface roughness in fractures

Roughness in fracture planes refers to features used to describe and measure the asperities of a surface. According to Euskal Herriko Unibertsitatea (2011); Grupo Tecnología Mecánica (2017); Hommel Etamic (2022); Thomas (1999), these characteristics include:

- Scale: Surface roughness can be observed at various scales, from micro-roughness (microasperities and fine textures) to macro-roughness (large-scale undulations). Micro-roughness can be influenced by sedimentary textures, while macro-roughness often results from processes like acidizing.
- Amplitude: Amplitude represents the height of the surface's asperities or irregularities and directly affects the frictional resistance to fluid flow. Greater amplitude results in higher roughness.
- Wavelength: This is the distance between successive peaks or troughs on the fracture surface. Variations in wavelength can affect fluid flow pathways and the effective aperture of the fracture.
- Geometry: Surface roughness can manifest in various geometric forms, such as ridges, grooves, steps, and pits. The geometry of these features can influence the tortuosity of fluid flow paths.

#### 3.2.1.2.2 Roughness measurement and analysis

Several techniques can quantify fracture surface roughness, including laser profilometry, atomic force microscopy, and scanning electron microscopy. A profilometer measures surface topography by recording height variations. When using

a profilometer, peak-to-valley height and texture are key descriptors to distinguish between rough and smooth surfaces. The height and texture distribution result from various factors, including the sample's length and mineralogy Sayles and Thomas, 1978). Roughness parameters, such as curvature and slope, may vary depending on the measurement area, scale, resolution, and computational methods (Jacobs, Junge, Pastewka, 2017).

**Peak-to-Valley Height:** This measures the difference in height between the highest point (peak) and the lowest point (valley) on a surface. It helps quantify overall roughness or irregularities. Thomas (1999) describes height as the roughness orthogonal to the mean plane, while texture refers to roughness within the surface plane. Smooth surfaces have a relatively small peak-to-valley height due to minimal height variations, while rough surfaces show larger peak-to-valley heights because of irregularities, bumps, and valleys.

Profilometer devices collect data on height and texture roughness descriptors, such as the roughness index, mean width, arithmetical mean deviation, mean slope, and peak curvature. Table 2 presents common statistical parameters used to describe surface roughness in terms of height and texture.

Table 2 – Fracture roughness descriptors from height and texture.

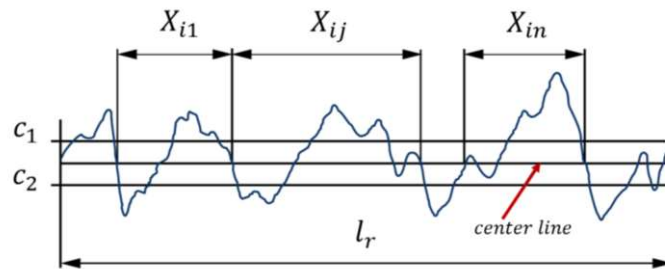
Height descriptor		Texture descriptor	
Average roughness, <b><math>R_a</math></b>	$R_a = \frac{1}{n} \sum_{i=1}^n  Z_i $	Mean slope, <b><math>Ms</math></b>	$Ms = \frac{1}{n-1} \sum_{i=1}^{n-1} \frac{Z_{i+1} - Z_i}{\Delta Z}$
Root-mean-square, <b><math>RMS</math></b>	$RMS = \sqrt{\sum_{i=1}^n Z_i^2 \frac{1}{n}}$	Average wavelength, <b><math>\lambda_a</math></b>	$\lambda_a = 2\pi \frac{R_a}{m}$
Skewness, <b><math>Sk</math></b>	$Sk = \frac{1}{nRMS^3} \sum_{i=1}^n Z_i^3$	Peak curvature, <b><math>C_p</math></b>	$C_p = \frac{1}{n-2} \sum_{i=1}^{n-2} \frac{2Z_i - Z_{i-1} - Z_{i+1}}{\Delta Z^2}$
Kurtosis, <b><math>Ku</math></b>	$Ku = \frac{1}{nRMS^4} \sum_{i=1}^n Z_i^4$	Semi variogram <b><math>\gamma</math></b>	$\gamma = \frac{1}{2(n-h_d)} \sum_{i=1}^{n-h_d} Z_{i+h_d} - Z_i$
mean width, <b><math>RS_m</math></b>	$RS_m = \frac{1}{n} \sum_{i=1}^n X_i$		

$Z_i$ : height;  $n$ : number of points;  $X_i$ : width;  $h_d$ : correlation distance

Source: modified from Cardona (2020, p. 71)

For example, the mean width of profile elements (RSm) represents the average width of roughness profile elements within the sampling length ( $l_r$ ). This measurement is obtained by defining height thresholds ( $c_1$  and  $c_2$ ) that correspond to the surface function (see Figure 25). The measurement of this parameter adheres to the ISO 4287 standard (Hommel Etamic, 2022).

Figure 25 – Example of a roughness profile and elements to define the mean width (RSm).



Source: Modified from Hommel Etamic (2022)

### 3.2.1.3 Hydraulic transmissivity

To understand hydraulic transmissivity, it is essential to first describe hydraulic conductivity or permeability (see Section 3.1.3.3.2 – Permeability in Carbonate Rocks). According to Dielman (2005), hydraulic conductivity is a property that governs fluid flow through porous media. Specifically, it measures how effectively a geologic formation or porous medium transmits a given fluid. In contrast, transmissibility (or transmissivity) is a related concept that describes the capacity of a fluid to flow through a specified thickness ( $h$ ) of a medium, such as a fracture. Transmissibility is calculated by multiplying the effective hydraulic conductivity of a formation or aquifer by the thickness of that unit.

$$T = kh \quad (3)$$

Table 3 presents models of fracture transmissivity as a function of normal stress (Gale, 1982 qtd. in Cardona, 2020; Gutierrez; Øino; Nygård, 2000; Swan, 1983; Walsh, 1981) and as a function of shear displacement (Nguyen and Selvadurai, 1998; Olsson and Barton, 2001; Plesha, 1987; Tezuka; Tamagawa; Watanabe 2005).

Table 3 – Fracture transmissivity models

Model	References
$T = T_{\sigma_{\infty}} + (T_{\sigma_0} - T_{\sigma_{\infty}}) \left( \frac{\sigma' + \sigma_c}{\sigma_c} \right)^{-\gamma}$	Gale (1982) qtd. in Cardona (2020)
$T = T_{\sigma_{\infty}} + (T_{\sigma_0} - T_{\sigma_{\infty}}) \exp \left( -\gamma \frac{\sigma'}{\sigma_c} \right)$	Gutierrez; Øino; Nygård (2000)
$T = T_c \left[ 1 - \xi \ln \left( \frac{1 \text{ MPa}}{\sigma' + \sigma_L} + \frac{1 \text{ MPa}}{\sigma_H} \right)^{-1} \right]^3$ $\sigma_H = e^{(1-3\sqrt{T_{\sigma_{\infty}}/T_c})/\xi}$ $\sigma_L = \frac{\sigma_H}{e^{(3\sqrt{T_{\sigma_0}/T_c} - 3\sqrt{T_{\sigma_{\infty}}/T_c})/\xi} - 1}$ $\xi = \frac{\sqrt{2}RMS}{h_0}$	Walsh (1981)
$T = T_c \left[ 1 - \zeta \ln \left( \frac{1 \text{ MPa}}{\sigma' + \sigma_L} + \frac{1 \text{ MPa}}{\sigma_H} \right)^{-1} \right]^2$ $\sigma_H = e^{(1-\sqrt{T_{\sigma_{\infty}}/T_c})/\zeta}$ $\sigma_L = \frac{\sigma_H}{e^{(\sqrt{T_{\sigma_0}/T_c} - \sqrt{T_{\sigma_{\infty}}/T_c})/\zeta} - 1}$	Swan (1983)
$T = \frac{\rho g}{12\mu} (\mu_G/\mu m)^{3/2} JRC_{mob}^3$	Olsson and Barton (2001)
$T = \frac{\rho g}{12\mu} (h_{H0} + f\Delta h)^3; f = f_0 \exp \left( -\int_0^{W^p} c_f dW^p \right)$	Nguyen and Selvadurai (1998); Plesha (1987)
$T = \frac{\rho g}{12\mu} \left( \frac{A_s}{1 + 9 \frac{\sigma_n}{B_s}} h_{H0} \right)^3$ $\text{where } A_s = \begin{cases} 1 & \text{before shear} \\ > 1 & \text{after shear} \end{cases}$	Tezuka; Tamagawa; Watanabe (2005)
$\frac{T(\delta_s) - T_{\delta_0}}{T_{\delta_{\infty}} - T_{\delta_0}} = \frac{e^{\left( \frac{1}{1+e^{\eta(1-\frac{\delta_s}{\delta_{sc}})}} - 1 \right)}}{1 - T_c} - T_c$ $\text{where } T_c = e^{\left( \frac{1}{1+e^{\eta}} - 1 \right)}$	Cardona; Finkbeiner; Santamarina (2001)

Source: Cardona (2020, p. 90)

Cardona; Finkbeiner; Santamarina (2001) propose an asymptotically model that exhibits a distinct S-shaped trend on a log-log scale to assess changes in fracture transmissivity as a function of shear displacement (see line 8 in Table 3). This model is characterized by four fitting parameters: the  $\eta$ -exponent, which represents the sensitivity of fracture transmissivity;  $\delta_{sc}$ , which denotes the displacement at maximum dilatancy or contractive rate; and the asymptotes  $T_{\delta_0}$  as  $T_s \rightarrow 0$  and  $T_{\delta_{\infty}}$  as  $\delta_s \rightarrow \infty$ .

## SECTION 2 – LABORATORY PROCEDURES

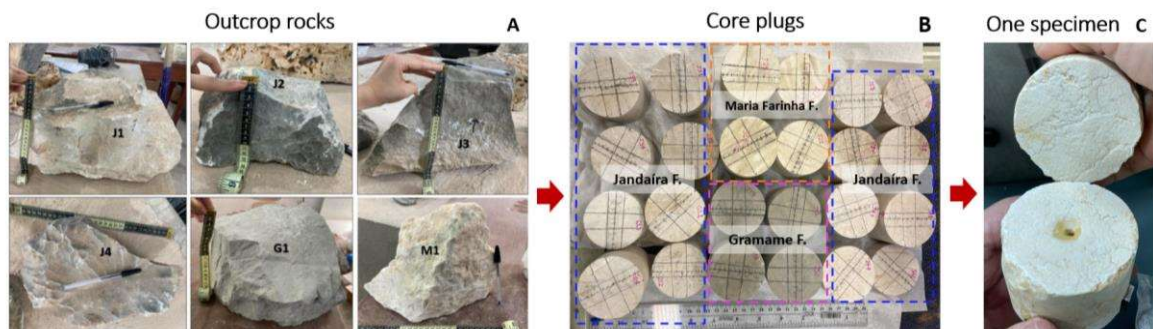
### CHAPTER 4 – FRACTURE TRANSMISSIVITY EXPERIMENTS

In this study, fracture transmissivity is estimated by subjecting fractures to chemical dissolution and torsional displacement under axial loading. Physical analyses, including petrography, whole-rock chemistry, and fracture-surface topography, are used to evaluate how normal stress, chemical dissolution, and shear stress affect fracture transmissivity along pre-formed fracture surfaces. The experiments involve both smooth and rough surfaces with various sedimentary textures.

#### 4.1 MATERIALS AND SAMPLE PREPARATION

As described in Section 1.4, the research uses outcrop samples from the Maria Farinha, Gramame, and Jandaíra formations (Figure 6). From each rock of Figure 26A was obtained four core plugs, twenty-four core plugs in total (Figure 26B). The experimental design considers two core plugs as one specimen (Figure 26C), using the contact surface between them to represent a fracture plane (non-matching surfaces). One pair of specimens was prepared with a smooth contact surface, and the other with a rough contact surface. These specimens are labeled accordingly, for example, J11 to J14 for the four subsamples of Sample J1.

Figure 26– From outcrop rocks of Maria Farinha, Gramame, and Jandaíra formations to core plugs and one specimen for the experiment

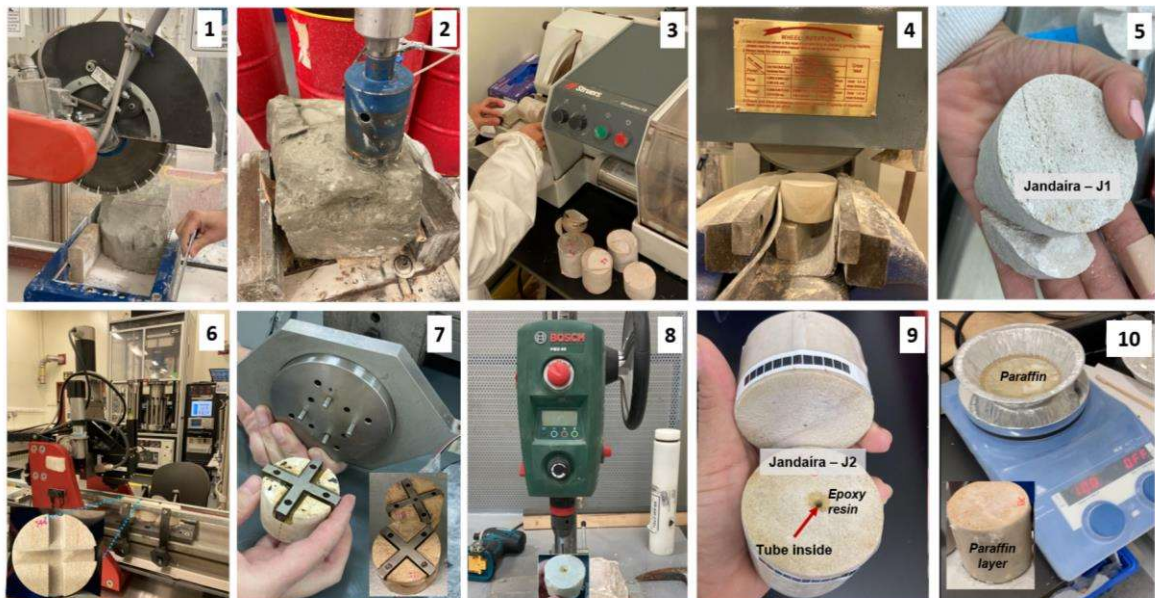


Source: author



The following routine was applied in the sample preparation (Figure 27): (1) the original blocks were cut into small pieces to facilitate sample preparation; (2) 55-mm-diameter plugs were drilled; (3) the plugs were cut to obtain 40–70-mm-long pieces; (4) the core ends were prepared with a surface grinder to obtain a pulish surface (only for samples used as smooth surface); (5) rough core-end surfaces were prepared by sandblasting (only for samples used as rough surface); exclusively for torsion test (6) and (7): the samples were scratched with a scratch test, and steel crosses were fixed with epoxy resin to assembly it in the equipment; (8) counterbored holes (18 mm; through-hole 3.5 mm in diameter) were drilled through the plugs from the other end; and (9) the internal (inlet) tube was fixed with epoxy resin to avoid leakage during the fluid injection; and (10) the edges were paraffined to prevent acid damage to the rock matrix (just for acidified samples).

Figure 27 - Sample preparation stages: (1) cutting blocks into smaller pieces; (2) subsample plugs; (3) cutting plugs to the required length; (4) smoothing sample surfaces; (5) roughening sample surfaces; (6) scratching the groove; (7) fixing steel cross; (8) drilling inner hole for pressure line to let fluid injection into the fracture plane; (9) sealing the inlet tube with epoxy, and (10) paraffining the perimeter of the samples.



Source: author

The torsion test was conducted on a few samples due to the breaking of it while creating the grooves. Consequently, only two pairs of rocks with smooth and rough surfaces were subjected to torsion testing after the samples had previously been utilized in the acidification tests.

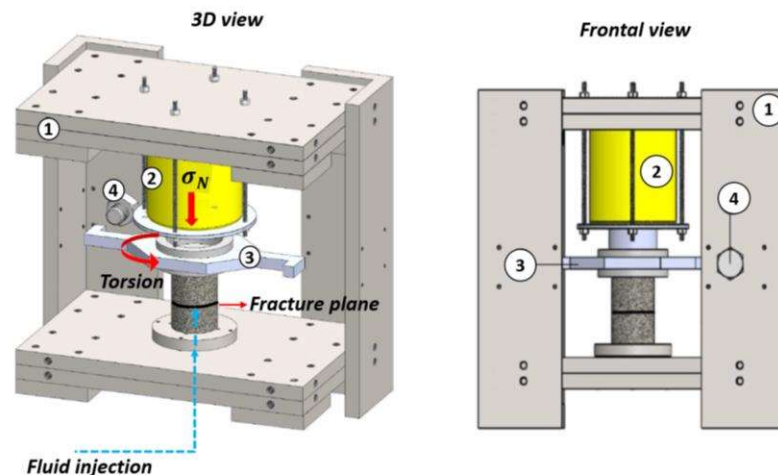


## 4.2 EXPERIMENTAL DEVICE AND SETUP

The experiments were conducted using a Torsional Ring Shear Device, custom-designed by Cardona (2020) at the Ali I. Al-Naimi Petroleum Engineering Research Center, KAUST University. This device is designed to assess the effects of surface roughness on the chemo-hydromechanical behavior of pre-existing fractures.

The torsional device enables fluid injection through a hole drilled into the plug sample (Step 8 in Figure 27) while simultaneously applying normal and shear stresses. Figure 28 provides both a 3D and frontal view of the device, which includes: (1) a steel frame; (2) a hydraulic cylinder for applying axial force; (3) a steel plate with two lever arms moved by (4) two horizontally mounted screws to apply torsional displacement (these are only adjusted during the torsion test); and (5) a flexible tube (indicated by the blue dashed line) that connects the pressure pump to the lower steel plate. This tube feeds fluid (water or acid) through an inner hole at the lower part of the sample, injecting it directly into the fracture plane. The fluid flows radially within the fracture, and since the sample is not confined in a jacket, the fluid runs down along the sides of the sample. The radial flow is normal to the shear direction. The pressure gradient is determined by the pressure within the tube and the atmospheric conditions.

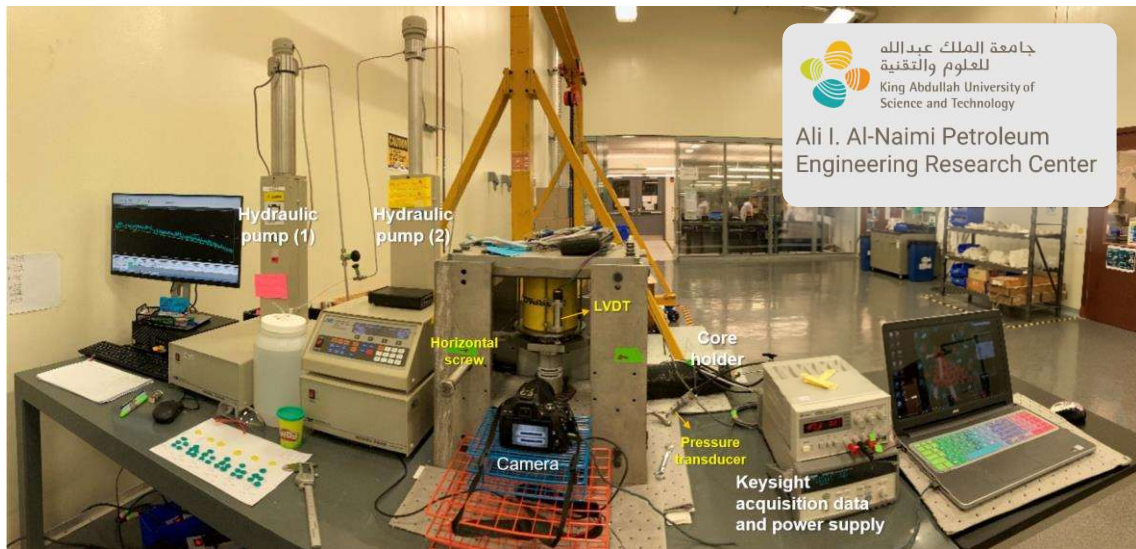
Figure 28 - The torsional shear device allows measuring the hydromechanical and chemical processes occurring along a pre-existing fracture surface (rough, smooth, mated, and unmated). The equipment comprises (1) a steel reaction frame, (2) an Enerpac cylinder (yellow), and (3) a steel plate with two lever arms moved by (4) two screws mounted horizontally.



Source: Modified from Cardona (2020, p. 86).

In addition to the Torsional Ring Shear Device, the experimental setup includes several other components: two hydraulic pumps, a core holder for the hydrochloric acid (HCl) solution, a data acquisition system, a power supply, two computers, and a camera (see Figure 29). Hydraulic pump (1) uses oil to control the Enerpac cylinder, while hydraulic pump (2) operates with water and manages the water/acid injection. The core holder is specifically adapted for acid injection and works in conjunction with pump (2). The camera is used to capture images of the fracture aperture throughout the experiments.

Figure 29 - Experimental setup and measurement accessories.

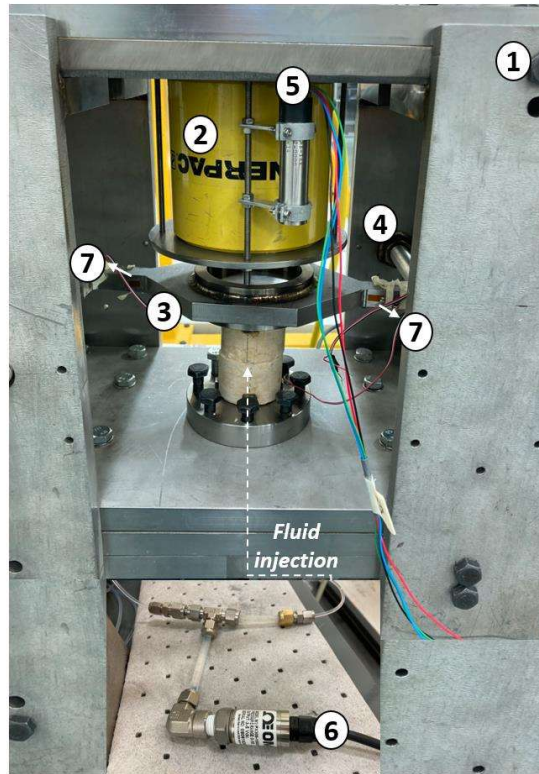


Source: author

#### 4.2.1 Experimental measurements and accessories

Vertical displacement, fluid pressure, and strain are measured directly during the experiments using a linear variable differential transducer-LVDT (5), a pressure transducer (6), and a set of four strain gauges (7), respectively (see Figure 30). The LVDT rod is installed in the Enerpac cylinder to record normal displacement during stress cycling. The pressure transducer, located in the fluid pathway between hydraulic pump (2) and the lower steel plate, monitors the injection pressure. During torsion tests, the strain gauges, positioned on the lever arm, measure the deformation of the steel plate and calculate the shear stress resulting from the applied torsion.

Figure 30 – Changes in fracture transmissivity were derived by measuring the sample's normal displacement with an LVDT rod (5) positioned along the Enerpac cylinder (yellow), the injection pressure monitored using a pressure transducer (6) connected to the pump pressure -not shown- before the injected fluid entered the specimen and fracture plane (white dashed line), and the shear displacement using two pairs of strain gauges (7) on each lever arm.



Source: author

### 4.3 EXPERIMENTAL METHODOLOGY

Two types of experiments are conducted using the Torsional Ring Shear Device: (1) an acidification test to investigate the chemo-hydromechanical effects on fracture transmissivity, and (2) a torsion displacement test to evaluate the impacts of normal and shear stresses (induced by torsional displacement) on fracture transmissivity. Both experiments are performed on different fracture surface roughnesses and rock mineralogies. The equipment's stress range reaches this study's aims, allowing the identification of basic phenomena during stress-acid-fracture interaction.

#### 4.3.1 Chemical dissolution test procedure

The chemical dissolution (or acidification) experiment follows these steps:

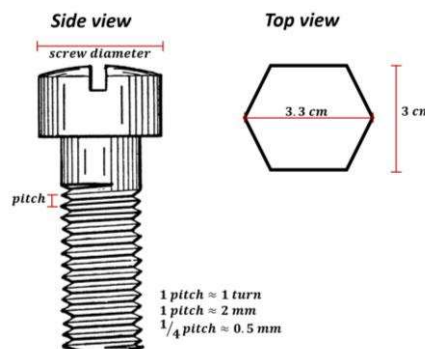
- 1- Pump (1) applies a normal loading and unloading cycle, while pump (2) maintains a constant flow rate of water injection into the fracture.
- 2- At the end of the unloading phase and without moving the sample, a normal stress of 0.55 MPa is applied using pump (1). Meanwhile, pump (2) injects 5 cm<sup>3</sup> of an HCl solution (0.01 mol/L concentration, pH = 2) into the fracture at a rate of 1 cm<sup>3</sup>/min for 5 minutes.
- 3- After the acid injection, the normal loading and unloading cycle described in step 1 is repeated.

#### 4.3.2 Torsion test procedure

The torsion experiment is conducted as follows:

- 1- Apply a normal stress of 0.6 MPa using pump (1), while maintaining a constant flow rate with pump (2) throughout the experiment.
- 2- Induce torsion by rotating the horizontal screws ( $\frac{1}{4}$  pitch or 0.5 mm Figure 30 and Figure 31) to apply torsional momentum to the lever arm. Simultaneously, pump (2) continues to inject water at a constant flow rate, as specified in step 1.
- 3- Repeat step 2 until fluid pressure and vertical displacement stabilize after each torsion. Approximately fifteen torsional displacements are applied to each sample.

Figure 31- Sketch of the side and top view of the screw. The screw's pitch applied during the torsion corresponds to one turn of the screw. Thus,  $\frac{1}{4}$  pitch is equal to 0.5 mm.



Source: author

#### 4.4 CALCULATED VARIABLES

Normal effective stress ( $\sigma'$ ) and fracture transmissivity ( $T$ ) are calculated in both chemical dissolution and torsion tests, while shear stress ( $\tau$ ) is determined only in the torsion experiment.

The normal effective stress is derived from a balancing force (for further details, refer to Appendix A1). Equation (4) describes normal effective stress as a function of the total stress ( $\sigma$ ), outer ( $D_{out}$ ) and inner ( $D_{in}$ ) diameter of the sample, pump pressure ( $P$ ), and the mean pressure ( $\bar{P}$ ).

$$\sigma' = \left( \frac{\sigma D_{out}^2 - P D_{in}^2}{D_{out}^2 - D_{in}^2} \right) - \bar{P} \quad (4)$$

$\bar{P}$  represents the average pressure between the inner and outer radius where the pressure distribution  $P(r)$  is obtained after integrating Darcy's law for a radial flow across a fracture. In equation (5) and (6),  $r_{in}$  and  $r_{out}$  correspond to the inner and outer radius, and  $P_{in}$  and  $P_{out}$  are the internal and external pressure, respectively. For further details on the derivation of equations (5) and (6), refer to Appendix A2.

$$P(r) = P_{out} + \frac{(P_{in} - P_{out}) \ln\left(\frac{r}{r_{out}}\right)}{\ln\left(\frac{r_{in}}{r_{out}}\right)} \quad (5)$$

$$\bar{P} = \frac{(P_{out} r_{out} - P_{in} r_{in}) + \frac{(r_{in} - r_{out})(P_{in} - P_{out})}{\ln\left(\frac{r_{in}}{r_{out}}\right)}}{r_{out} - r_{in}} \quad (6)$$

Fracture transmissivity is defined by integrating Darcy's law. For a comprehensive explanation of the derivation of  $T$ , see Appendix A3. Equation (7) represents fracture transmissivity as a function of flow rate ( $Q$ ), fluid density, gravity, outer and inner diameter of the sample, pump pressure, atmospheric pressure ( $P_{atm}$ ), and mean pressure.

$$T = \frac{Q \rho g}{P - P_{atm}} \left( \frac{\ln(D_{out}/D_{in})}{2\pi} \right) \quad (7)$$

Shear stress resulting from torsion displacement is obtained by integrating the torque moment on a hollow cylinder specimen. Equation (8) corresponds to shear stress as a function of internal and external diameters and the torque ( $M$ ). For detailed information on how equation (8) is derived, consult Appendix A4, A5, and A6.

$$\tau = \frac{12 M}{\pi(D_{out}^3 - D_{in}^3)} \quad (8)$$



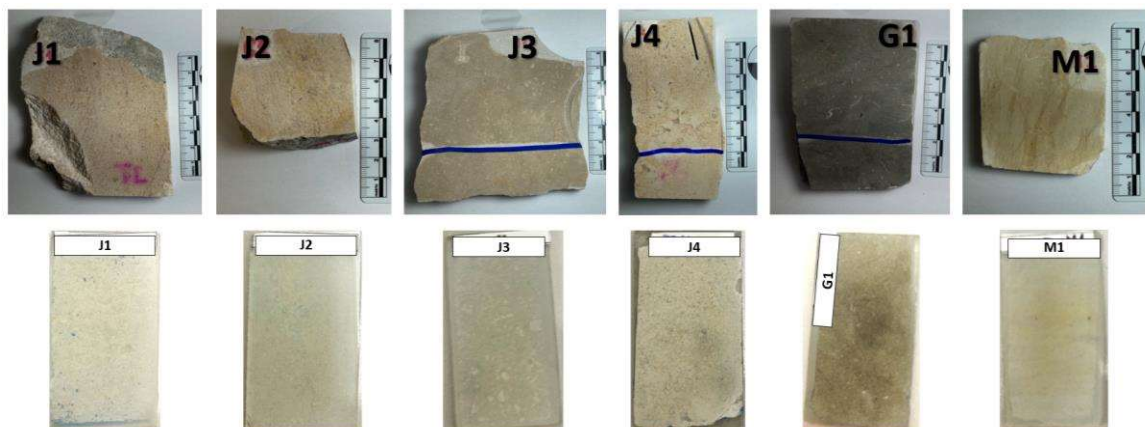
## CHAPTER 5 – ROCK PROPERTY ANALYSIS

Rock property analysis is a systematic investigation designed to evaluate and understand the physical, mechanical, chemical, and structural characteristics of rocks. This chapter explores rock characteristics and fracture attributes to better comprehend their behavior under stress and shear strain. The analysis in this research employs the following techniques and methodologies:

### 5.1 MICROSCOPIC CHARACTERIZATION

Microscopic characterization involves assessing rocks using petrographic and cathodoluminescence (CL) analyses. Figure 32 illustrates the rock specimens prepared for petrographic sectioning. During the preparation of thin sections, blue-dye epoxy impregnation is applied. This technique, described by Gardner (1980), enables visualization of the rock's void spaces on a micro-scale. Figure 32 also shows that the sections exhibit minimal impregnation of the blue-dye epoxy.

Figure 32- Rock specimens and thin section of Jandaíra, Gramame, and Maríá Farinha formations. The thin sections display low impregnation of the blue-dye epoxy.

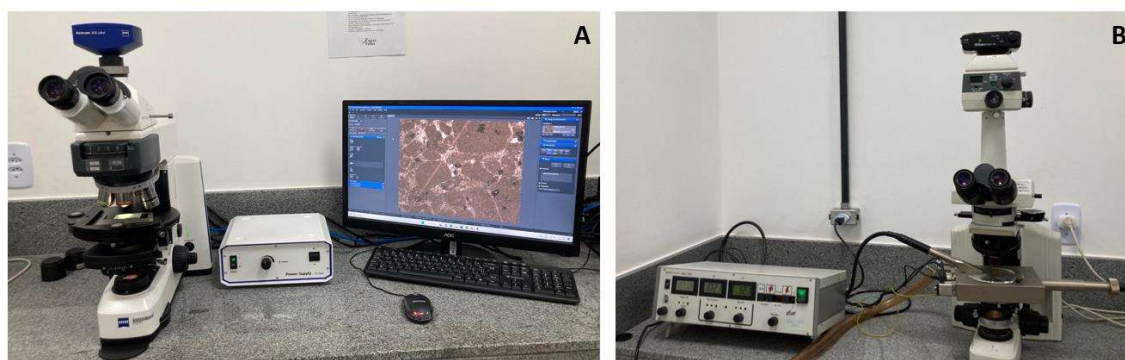


Source: author

Petrographic analysis examines the composition, texture, mineralogy, and structure of rock samples. Complementing petrographic descriptions, CL analysis helps identify diagenetic processes by revealing internal changes in the mineral crystalline structure. Figure 33A shows a Zeiss polarized-light microscope with an

integrated digital camera (Axiocam 305 color), used to develop petrographic descriptions of the rocks. Figure 33B depicts a Nikon Eclipse polarized petrographic microscope paired with an X-ray energy dispersive spectrometer, employed for cathodoluminescence analysis.

Figure 33- Petrographic and cathodoluminescence characterization using A- Zeiss polarized-light microscope equipped with an integrated digital camera Axiocam 305 color, and B- Nikon Eclipse polarized petrographic microscope coupled with an X-ray energy dispersive spectrometer.



Source: author

The classification of the samples followed the frameworks proposed by Dunham (1962) and Folk (1962). The identification of depositional environments was informed by previous studies of the Maria Farinha and Gramame Formations, as outlined by Barbosa (2004, 2007), and Jandaíra Formation, as reported in Córdoba (2001).

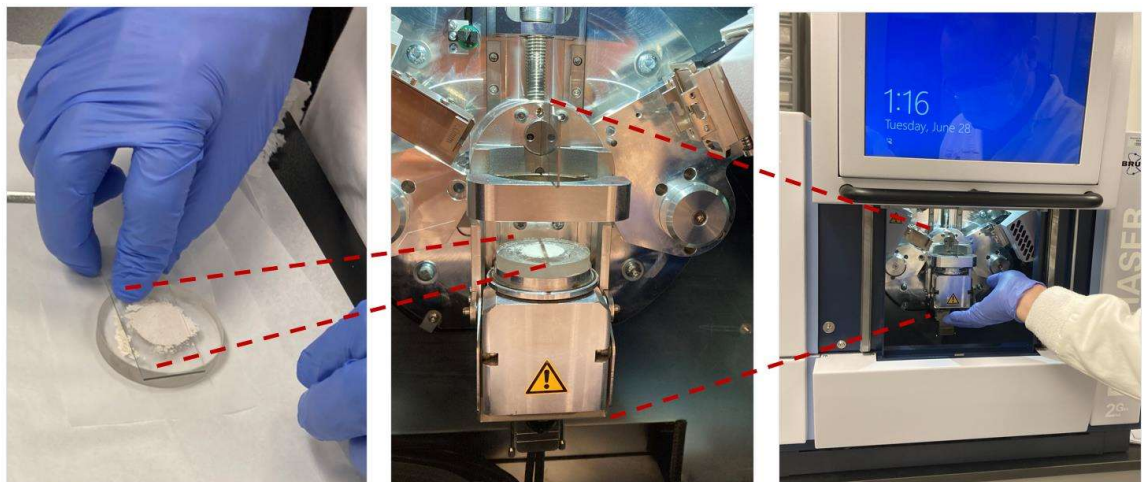
## 5.2 GEOCHEMICAL CHARACTERIZATION

The geochemical analysis comprised X-ray powder diffraction (XRD) and X-ray fluorescence (XRF) testing. For XRD analysis, the sample was first pulverized into a dry powder, which was then analyzed using a Bruker D2 Phaser diffractometer (Figure 34). The sample was placed at the center of the diffractometer and exposed to a high-energy X-ray beam. The X-rays were diffracted by the atoms in the sample at various angles, producing an X-ray diffraction pattern. This pattern was collected by a detector and used to determine the crystal structure of the sample. The position and intensity of the diffraction peaks in the pattern are related to the atomic arrangement within the sample, enabling the identification of its crystalline components using Bragg-Brentano geometry (Smith; Jenkins; Buhrke, 1998).



For XRF analysis, the powdered sample was dried in an oven at 110°C. A portion of the dried material was then compacted into pellets using an aluminum capsule and a pressure of 30 tons. These pellets were analyzed with a Rigaku X-ray fluorescence spectrometer ZSX Primus II, which is equipped with a rhodium tube and seven analyzing crystals. When X-rays interact with the material, the atoms absorb energy and become excited to higher energy levels. As the atoms return to their original energy levels, they emit radiation in the form of X-ray fluorescence. The XRF spectrometer measures the intensity of this emitted fluorescence, which is used to determine the chemical composition of the material. The intensity and spectrum of the emitted X-ray fluorescence are indicative of the material's composition (Smith; Jenkins; Buhrke, 1998; Vitha, 2015)

Figure 34- The J1 sample of the Jandaíra Formation was pulverized and prepared for X-ray powder diffraction (XRD) testing using the Bruker D2 Phaser diffractometer.

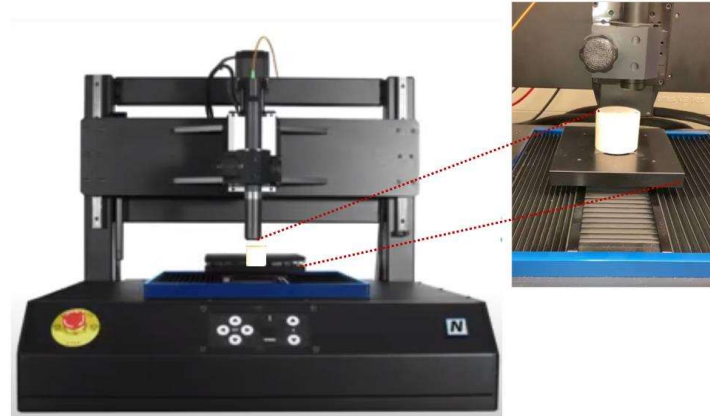


Source: author

### 5.3 FRACTURE SURFACE CHARACTERIZATION

The fracture surface roughness is analyzed using a Nanovea ST500 profilometer (Figure 35), which provides various parameters for characterizing surface roughness. This profilometer delivers quantitative data on surface roughness by measuring the heights of peaks and valleys.

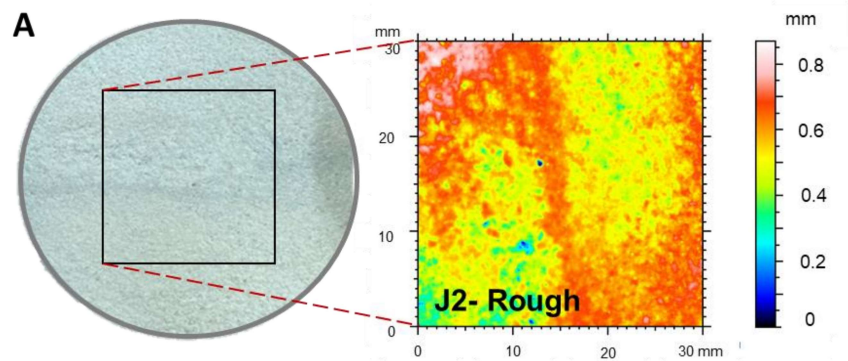
Figure 35- Nanovea ST500 profilometer device used to characterize fracture surfaces on all studied samples.

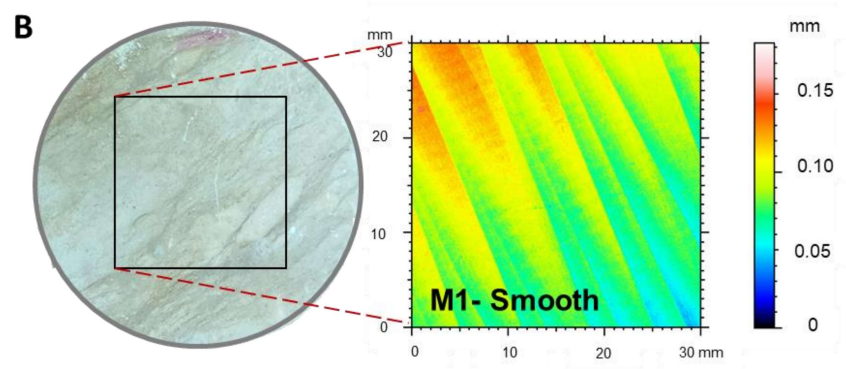


Source: author

In this research, roughness measurements refer to the arithmetic mean value of the width of surface asperities along the profile ( $RS_m$ ). The roughness of all studied surfaces was assessed before and after the application of acid. The profilometer scanned the rock specimens over a 60 x 60 mm area on the X–Y axis, at a scan speed of 20 mm/s, using an optical pen with a 10 mm width. Figure 36A and 36B illustrate profile scans of surfaces from samples of the Jandaíra and Maria Farinha formations, respectively. The peak-to-valley heights varied from 0 to 0.2 mm for smooth surfaces and from 0 to 0.9 mm for rough surfaces.

Figure 36- Plug sample cross sections (left) and roughness maps (right) for the: A Jandaíra Formation (Sample J2), with a rough fracture surface; and B María Farinha Formation (Sample M1), with a smooth fracture surface. The roughness scale ranges from blue (indicating low roughness) to red (indicating high roughness).





Source: author

## SECTION 3 – RESULTS AND ANALYSIS

### CHAPTER 6 – ROCK CHARACTERIZATION

This chapter presents the findings derived from the rock characteristics observed from the microscopy, chemical analysis, and scans of fracture surfaces.

#### 6.1 PETROGRAPHY AND CATHODOLUMINESCENCE

The microscopic characterization of the rocks studied in this research enables the following textural classification,

- *Mudstone to wackstone* (Samples M1 and G1)

Samples M1 and G1 are primarily mud-supported and composed of fine to very fine grains, indicating a low-energy setting. The grains in Sample M1 consist of diverse bioclasts, including foraminifera, bivalves, and shell fragments. Contrastingly, the grains in Sample G1 correspond to dolomite, formed by the replacement of the calcareous matrix, with some opaque minerals (probably pyrite), and local fragments of fish bones filled with sparite calcite. Samples M1 and G1 exhibit microlamination, with an alternating pattern of sparite calcite crystals and clay minerals. The microfacies of these samples are associated with biomicrite, local biosparite (see Sample M1 in Figure 37A), and dolomitized biomicrite (see Sample G1 in Figure 37B), suggesting their deposition occurs in low-energy settings, such as a shallow lagoon and/or carbonate bank with a high influence of terrigenous sediments, as described in previous studies. (Barbosa 2007; Barbosa and Lima Filho 2006; Gertsch et al., 2013).

- *Packstone* (Samples J1 and J2)

These samples contain bioclasts derived from foraminifera, bivalves, echinoderms, gastropods, and ostracods. Ooids with concentric and radial structures are observed only in Sample J1. Sample J2 has a lower bioclast content than J1 but is characterized by numerous elongated and semi-rounded pelletal grains. Sample J2 presents grains of different sizes arranged irregularly and filled with micrite and mosaic

calcite. The composition of the intergranular space exhibits variations from micrite to sparite (predominantly in Sample J2). The poor sorting and low matrix content indicate that these sediments are deposited in moderate- to high-energy conditions. Specifically, the microfacies are classed as biosparite (see Sample J1 in Figure 37C) and biopelsparite (see Sample J2 in Figure 37D), indicating a shallow-water environment, as has previously been described in the literature (Córdoba 2001; Santos et al., 2015).

- *Grainstone* (Sample J4)

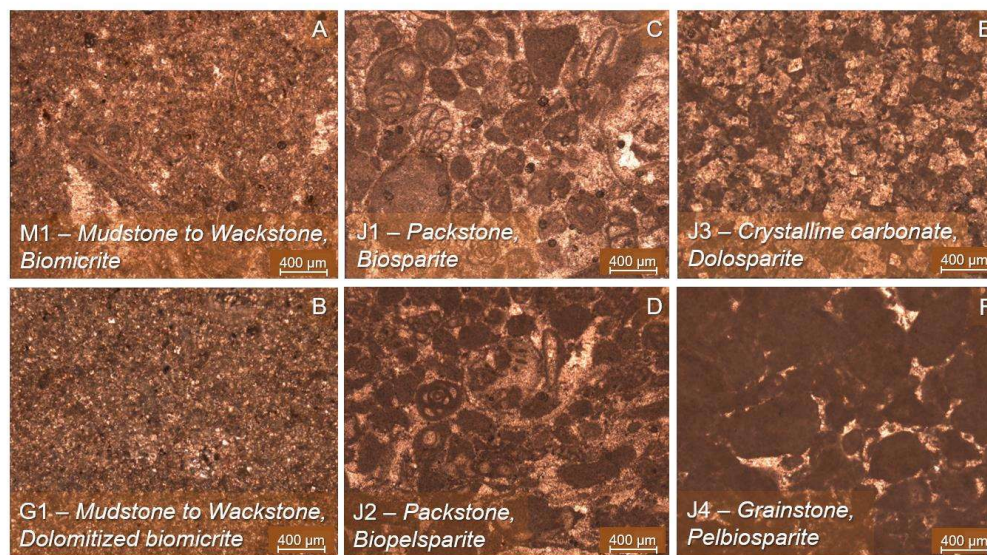
Sample J4 is grain-supported and composed of bioclastics and pellets. The intergranular space is filled with fine grains of calcite, generally in the form of sparite. The bioclasts correspond to small foraminifera fragments and shells. The grains are of medium to large size, with angular and semi-rounded shapes, indicating high-energy depositional conditions and poor sorting. Sample J4 is classed as a pelbiosparite (see Figure 37F), which is associated with shallow-water depositional environments (Córdoba 2001; Santos et al., 2015).

- *Crystalline carbonate* (Sample J3)

This sample is primarily composed of fine to very fine crystals of dolomite and some irregular pellets filled with micrite. The matrix content is low and consists of sparite. The bioclasts are well-sorted, indicating a low-energy depositional environment. The high dolomite content suggests a late diagenetic process that resulted in the formation of a dolosparite (Figure 37E). The texture is associated with a shallow-water carbonate facies (Córdoba 2001).



Figure 37- Illustrations from thin-sections of the samples. These carbonate rocks correspond to microfacies determined by sparite cement type (e.g., biosparite, biopelsparite, and dolosparite) and micrite matrix (e.g., biomicrite).



Source: author

## 6.2 GEOCHEMICAL ANALYSIS

Table 4 shows the samples' chemical composition based on the XRF analysis. Calcium (Ca) was dominant in all the samples, especially those from the Jandaíra Formation. The terrigenous content was higher in the Maria Farinha and Gramame formations, as demonstrated by the aluminum (Al) and silicon (Si) values.

Table 4- Geochemical composition of the Maria Farinha, Gramame, and Jandaíra formations. Major constituents are calcium oxide, aluminum oxide, and silicon dioxide. The results are expressed in weight percentage [wt %].

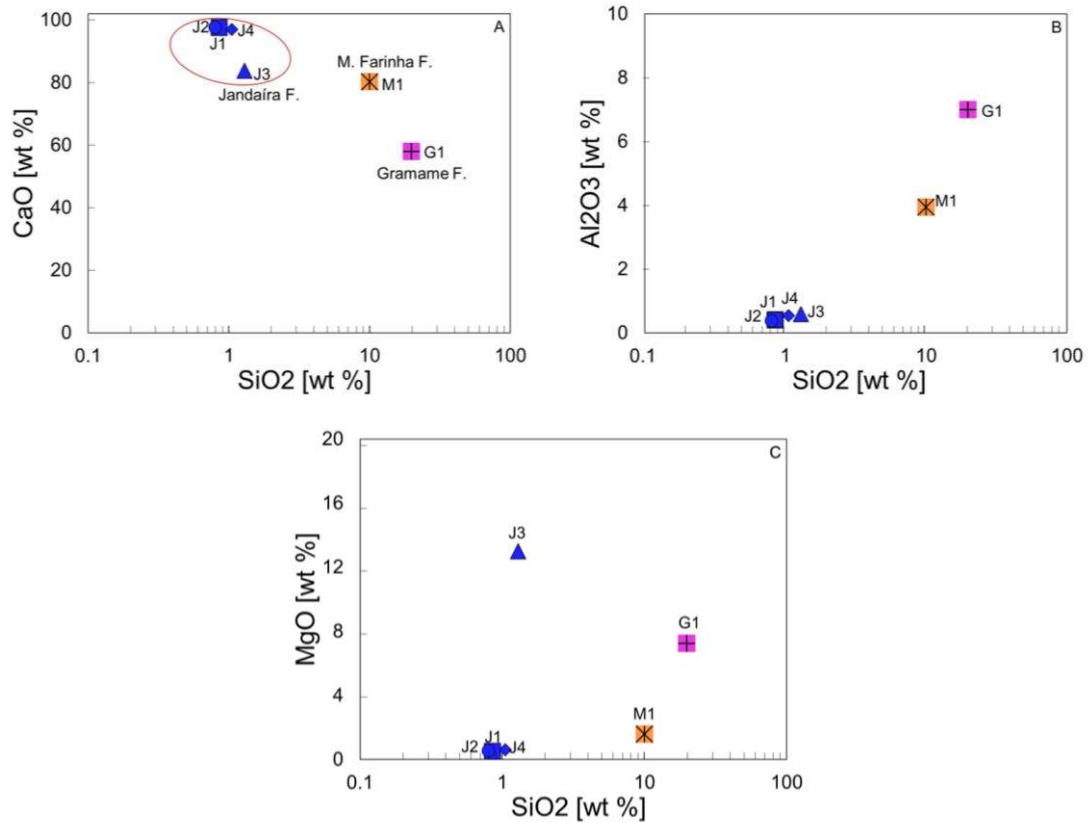
Formation	Sample	MgO	Al <sub>2</sub> O <sub>3</sub>	SiO <sub>2</sub>	P <sub>2</sub> O <sub>5</sub>	SO <sub>3</sub>	Cl	K <sub>2</sub> O	CaO	Fe <sub>2</sub> O <sub>3</sub> T
Jandaíra	J1	0.52	0.41	0.85	0.26	0.08	N.D.	0.03	97.64	0.15
	J2	0.54	0.38	0.8	0.28	0.09	0.01	0.03	97.62	0.19
	J3	13	0.59	1.29	0.31	0.2	0.02	0.08	83.78	0.17
	J4	0.62	0.54	1.05	0.26	0.16	0.06	0.05	97.04	0.16
Maria Farinha	M1	1.58	3.95	9.97	0.79	0.1	0.02	1.1	80.28	N.D.
Gramame	G1	7.26	7	19.77	0.5	1.3	0.46	2.12	58.05	2.56
Minor elements: Na <sub>2</sub> O, TiO <sub>2</sub> , V <sub>2</sub> O <sub>5</sub> , Cr <sub>2</sub> O <sub>3</sub> , MnO, NiO, ZnO, Rb <sub>2</sub> O, Y <sub>2</sub> O <sub>3</sub> , ZrO <sub>2</sub> , Nb <sub>2</sub> O <sub>5</sub>										

Source: author

Figure 38A shows a crossplot between the silica ( $\text{SiO}_2$ ) and calcium oxide ( $\text{CaO}$ ) contents of the specimens. Samples from the Jandaíra Formation exhibit high Ca and low  $\text{SiO}_2$  contents, suggesting a carbonate depositional environment. Contrastingly, samples from the Paraíba Basin have lower CaO values as the  $\text{SiO}_2$  content increases. This implies changes in the depositional environment, with a higher influx of continental sediments occurring during carbonate deposition (Barbosa 2007; Barbosa and Lima Filho 2006; Córdoba 2001). Clay minerals and silicate minerals can influence the strength of carbonate rocks, and how the surfaces of those rocks are affected by dissolution.

Figure 38B shows a correlation between the aluminum oxide ( $\text{Al}_2\text{O}_3$ ) and  $\text{SiO}_2$  contents of the samples, indicating the amount of clay minerals present in the rocks. As observed in Figure 38A, the samples from the Potiguar Basin differ in composition from those in the Paraíba Basin. Samples from the Maria Farinha and Gramame formations exhibit a positive relationship between Si and Al, indicating the presence of clay minerals (Barbosa 2004; Barbosa et al. 2007; Santos et al., 2015). Contrastingly, the Si and Al values are low in the Jandaíra Formation samples, suggesting a much lower influence of clay in their composition (Araújo et al., 2021; Córdoba 2001). Figure 38C presents a correlation between the samples' magnesium oxide ( $\text{MgO}$ ) and  $\text{SiO}_2$  contents. This correlation is useful for explaining whether the Mg relates to a siliciclastic or carbonate phase (Barbosa 2007; Pagel et al., 2000). In Sample G1, a positive correlation between  $\text{MgO}$  and  $\text{SiO}_2$  indicates a relationship between the  $\text{MgO}$  and the clay minerals in the siliciclastic phase. Barbosa (2007) reported the presence of glauconite in the Gramame Formation, linking it to the occurrence of Mg in the formation. Sample J3 shows a negative relationship between  $\text{MgO}$  and  $\text{SiO}_2$  that could link the presence of the  $\text{MgO}$  to a carbonate phase as a result of diagenetic changes (Barbosa 2007; Pagel et al., 2000). This is distinct from Samples J1, J2, and J4, which have the lowest  $\text{MgO}$  values. Sample M1 has low  $\text{MgO}$  values, which could be associated with a terrigenous phase, bringing clay minerals rich in potassium (K), Al, and Si, as Barbosa (2007) suggested.

Figure 38- Correlations of the elemental compositions of the samples: A- CaO vs SiO<sub>2</sub>, showing the influence of carbonate on the depositional system (carbonatic vs terrigenous); B- Al<sub>2</sub>O<sub>3</sub> vs SiO<sub>2</sub>, showing the influence of terrigenous components, such as detrital silicate minerals and clay minerals; and C- MgO vs SiO<sub>2</sub>, indicating the influence of siliciclastic vs carbonatic phases.



Source: author

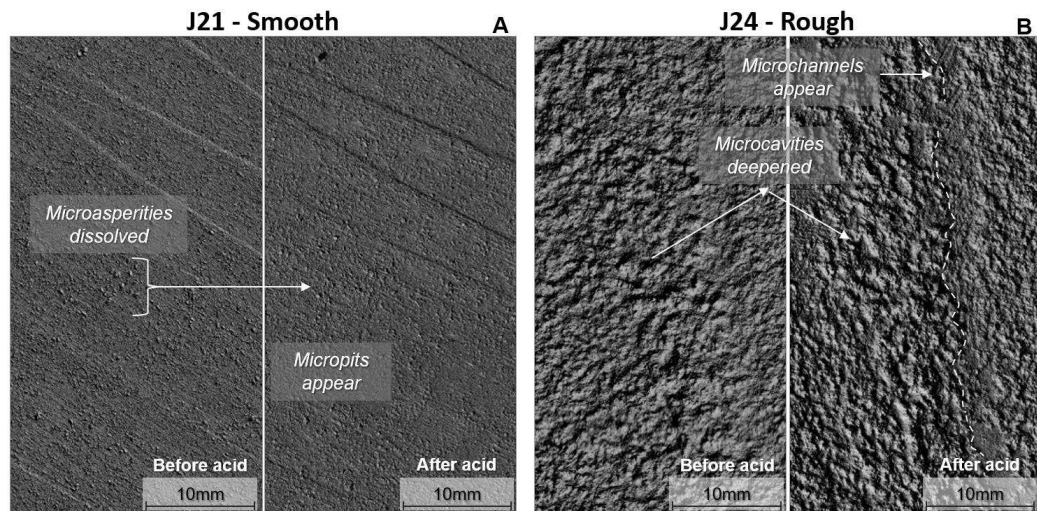
### 6.3 FRACTURE ROUGHNESS UNDER ACID FLOW

The smooth surfaces initially remained relatively unaltered after applying HCl to the sample surfaces. However, some microasperities (smooth surfaces, even when polished, are never truly smooth when viewed at high resolution) appeared to have dissolved (Figure 39A). Conversely, the samples with initially rough surfaces exhibited more prominent asperities after acidizing, which seems to have resulted from the deepening of pre-existing cavities (Figure 39B). The roughness increased on both the smooth and rough surfaces following acidizing but to different degrees. For instance, with the Jandaíra Formation samples, the average surface roughness of the smooth Sample J21 increased from 0.127 to 0.134 mm after acidizing, while the roughness of the rough Sample J24 increased from 0.331 to 0.387 mm. In general, two effects at the millimeter scale are observed: 1) local microasperities were dissolved on smooth



fracture surfaces, which developed micropitting and, thus, tended to become rougher; and 2) pre-existing cavities in initially rough fracture surfaces became deeper, tending to form channels. The deepening of these cavities due to the presence of the acid seems to have enhanced the pre-existing peaks.

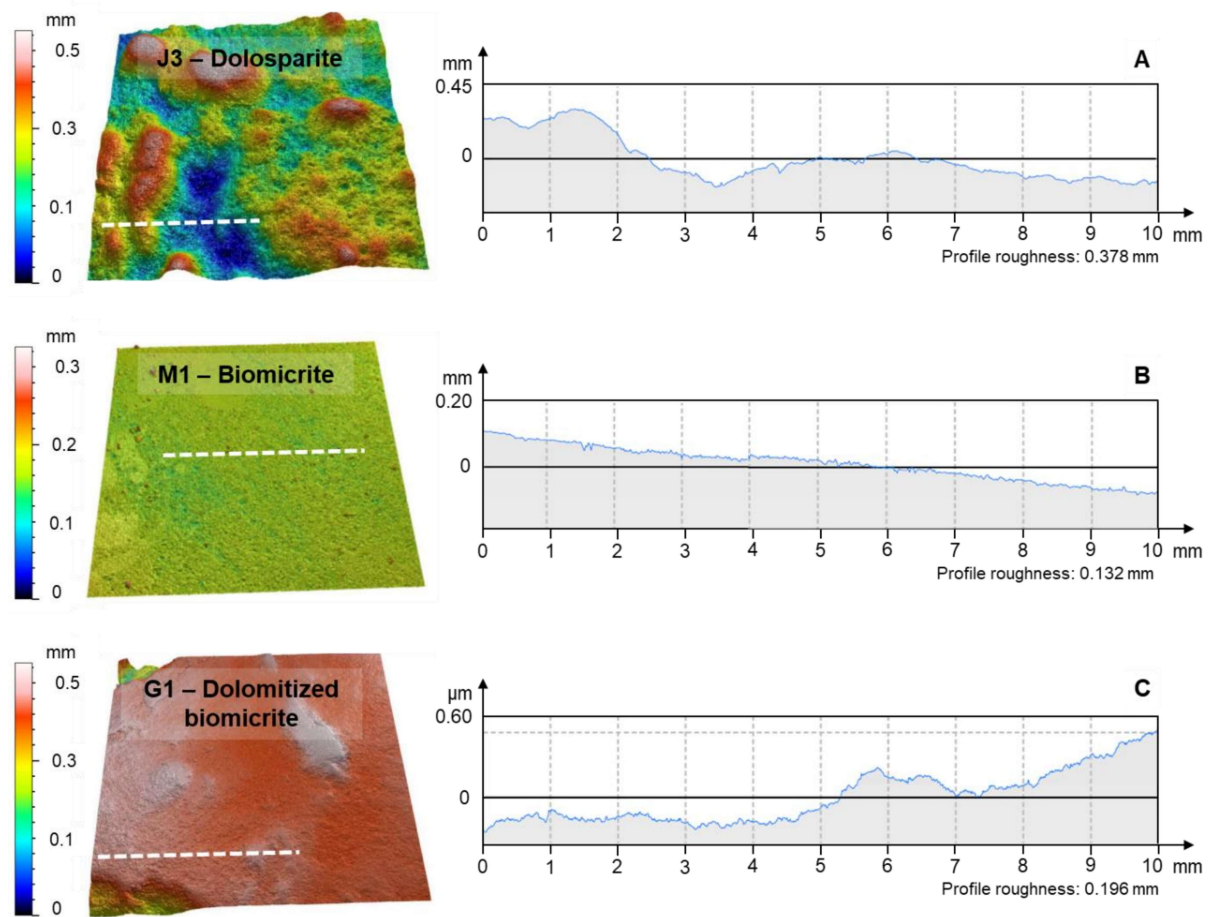
Figure 39- Comparison of images of fracture surfaces before and after acidizing the Jandaíra Formation samples: A- Smooth surface, J21; and B- Rough surface, J24. After acidizing, microasperities were smoothed on the smooth surface, while cavities were deepened on the rough surface.



Source: author

Figure 40 displays fracture topographies and roughness profiles (from along the dashed white lines) following the application of acid to Samples J3, M1, and G1. The grain size of the sample and the distribution of grains in the matrix governed the formation of a rougher or smoother topography on the fracture surface after acidizing (e.g., comparing J3 with M1). The carbonate rocks with high carbonate contents (i.e., calcite) tended to form deeper cavities in their fracture surfaces (Figure 40A). They were prone to channels forming, which resulted in an increase in roughness after acidizing. Contrastingly, the presence of clay minerals made the fracture surfaces more resistant to the acid and more prone to develop fine irregular reliefs without significantly altering surface roughness (Figure 40B and Figure 40C).

Figure 40- 3D views of rough fracture surfaces after application of the acid and their respective roughness profiles (from along the dashed white lines): A- Sample J3; B- Sample M1; and C- Sample G1. Their predominant mineralogical compositions are included. The values below each profile correspond to the average roughness along the profile. Asperity development after acidizing appears to be strongly related to each sample's mineralogy and texture.



Source: author

## CHAPTER 7 – FRACTURE TRANSMISSIVITY

Chapter 7 includes the results of the fracture transmissivity behavior when it is subjected to axial loading, chemical dissolution, and shear displacement by torsion.

### 7.1 FRACTURE TRANSMISSIVITY AS A FUNCTION OF EFFECTIVE NORMAL STRESS

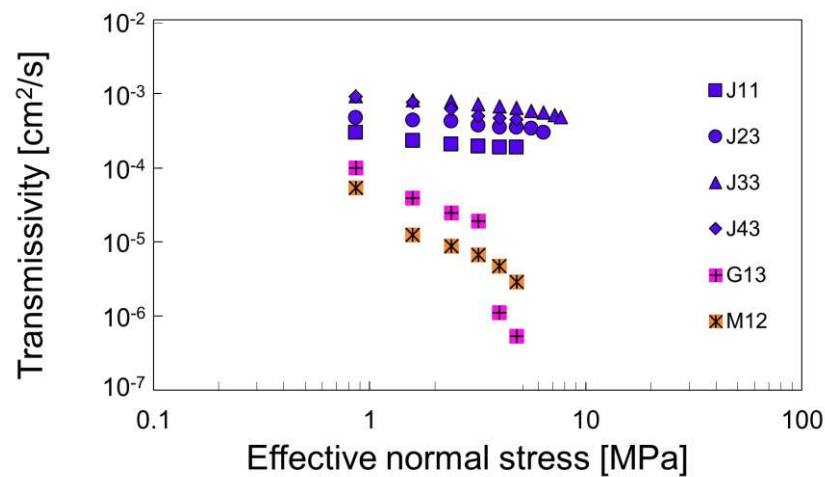
During the loading experiments, the increase in normal effective stress from 0.86 to 7.65 MPa decreased the transmissivity along all the fracture surfaces (e.g., samples with smooth fracture surfaces -Figure 41). We quantified this decrease in fracture transmissivity by comparing the change in transmissivity throughout the test with the initial transmissivity. All the samples had distinct mechanical apertures, even on their polished surfaces, due to the presence of microasperities.

Samples M12 and G13 exhibited strong variations in fracture transmissivity as a function of effective normal stress (Figure 41), with the fracture transmissivity decreasing by more than 90%, varying from  $5 \times 10^{-5}$  to  $2 \times 10^{-6}$  cm<sup>2</sup>/s in M12 and from  $1 \times 10^{-4}$  to  $5 \times 10^{-7}$  cm<sup>2</sup>/s in G13. This behavior is attributed to the presence of clay minerals (see Table 4 and Figure 38A). These minerals tend to present plasticity and thus deform more easily in response to the load (Rassouli & Zoback, 2018; Schoenball; Sahara; Kohl, 2014; Sone & Zoback, 2013).

The tests on samples mainly composed of calcite (see Samples J1 to J4 in Table 4 and Figure 38A) showed no significant reduction in transmissivity with increasing effective normal stress compared to samples from the Maria Farinha and Gramame formations. The reduction in fracture transmissivity in the Jandaíra Formation samples varied between  $1 \times 10^{-3}$  and  $2 \times 10^{-4}$  cm<sup>2</sup>/s. In addition, a reduction in fracture transmissivity occurred between 35 and 50% of the Jandaíra Formation samples. A possible explanation for this difference in transmissivity reduction in the Jandaíra Formation samples might be associated with the distinct initial mechanical aperture and the presence of chemical elements such as Mg and Al, particularly in Sample J33 (fracture transmissivity reduction = 50%).

In general, fracture transmissivity tended to decrease to  $2 \times 10^{-4}$  cm<sup>2</sup>/s in samples rich in Ca (Samples J1 to J4), despite the percentage differences in transmissivity reduction. Contrastingly, samples with more than a 10% clay mineral content displayed a significant decrease in fracture transmissivity with an increase in effective normal stress (Samples M12 and G13). Diagenetic processes and mineralogy (Ca and SiO<sub>2</sub> in the cement) (Bertotti et al., 2017) in the Jandaíra Formation samples might explain why the fracture asperities were able to sustain higher stress levels than the Maria Farinha and Gramame formation samples (Araújo et al. 2021; Bertotti et al., 2017). Silica cement can improve rock strength and reduce samples' dissolution susceptibility.

Figure 41- Fracture transmissivity evolution as a function of effective normal stress for samples with smooth surfaces. The presence of microasperities, which occur even in smooth surfaces, governed the different initial mechanical apertures and hydraulic behaviors for each sample.

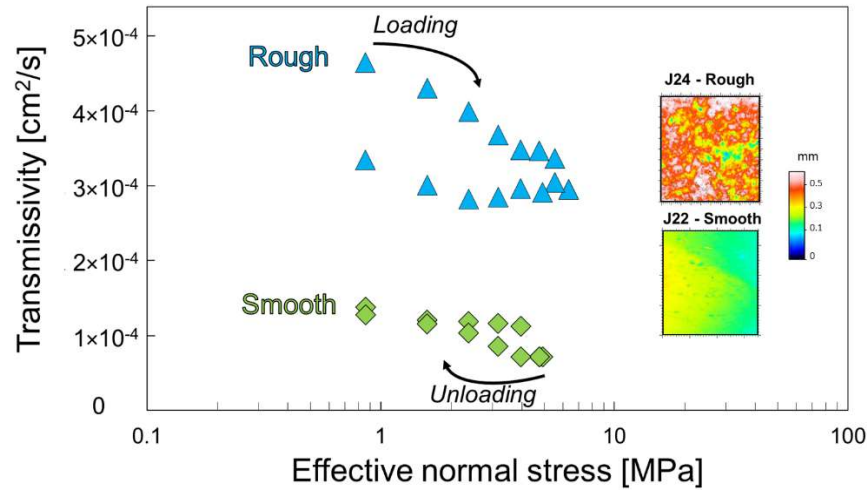


Source: author

Figure 42 compares the fracture transmissivity of a Jandaíra sample as a function of the effective normal stress for the smooth J22 (green diamonds) and rough J24 (blue triangles) samples during a loading and unloading cycle. The samples have fractures with average roughness values of 0.118 mm (smooth fracture surface) and 0.309 mm (rough fracture surface) (see insets in Figure 42). Both tests showed a reduction in fracture transmissivity with higher effective normal stress. The rough sample exhibited greater initial fracture transmissivity.

During loading, the transmissivity values along the rough fracture surface decreased from  $5 \times 10^{-4}$  to  $3 \times 10^{-4}$  cm<sup>2</sup>/s (Sample J24 in Figure 42). The interpretation is that the asperities not being strong enough to support the stress applied, even though the XRD analysis detected SiO<sub>2</sub>. Similarly, the transmissivity observed along the smooth fracture surface was also reduced during loading, from  $1 \times 10^{-4}$  to  $7 \times 10^{-5}$  cm<sup>2</sup>/s. The results for Sample J22 (Figure 42) show that the fracture transmissivity was almost constant, up to 4 MPa of effective normal stress, at this point, the transmissivity started to decrease.

Figure 42- Evolution of fracture transmissivity as a function of effective normal stress during loading and unloading for Sample J24 with a rough surface and Sample J22 with a smooth surface. The fracture transmissivity decreased in both cases, but to different degrees. The asperities on the rough fracture surface appeared to break irreversibly with loading, reducing the transmissivity to  $3 \times 10^{-4}$  cm<sup>2</sup>/s. During unloading, this loss of transmissivity was not recovered. Contrastingly, the smooth fracture surface showed quasi-flat initial fracture transmissivity behavior, but, at close to 4 MPa, it seems to suddenly lose transmissivity. Unlike the rough fracture surface, this loss in transmissivity was recovered during unloading, possibly due to there being a smaller difference between the mechanical and hydraulic apertures.



Source: author

The results in Figure 42 also reveal a permanent reduction in transmissivity in response to the stress cycle. This effect was particularly apparent in the rough J24 sample. The difference between the first loading point and the last unloading point showed a 28% reduction in transmissivity from the initial fracture transmissivity value, indicating an irreversible reduction in fracture transmissivity. Contrastingly, the loss of

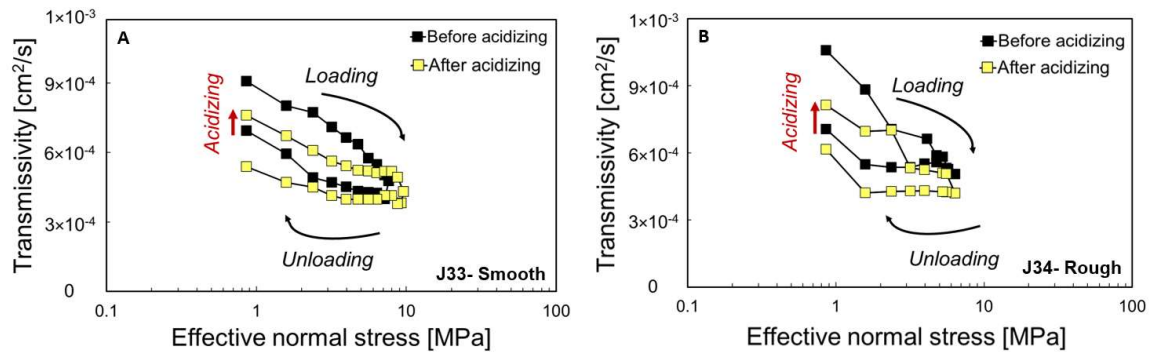
transmissivity in the smooth sample was only 7.5%, which is four times less than that observed along the rough fracture surface.

These results suggest that asperities on rough fracture surfaces may govern fluid flow along the fracture during loading. When a fracture is loaded normal to its plane, its asperities are likely prone to failure and uncoupled fracture faces, resulting in partial fracture closure and reduced transmissivity. This effect is more pronounced in rough fractures. For smoother fractures, the difference between mechanical aperture (i.e., physical measurement of the real separation between fracture surfaces, Ghoochaninejad et al. 2018) and hydraulic aperture (i.e., the effective aperture enabling fluid flow, Ghoochaninejad et al. 2018) will be smaller than in the rougher fracture.

#### **7.1.1 Chemo–hydro–mechanical coupling: fracture transmissivity changes due to chemical dissolution**

Figure 43A and Figure 43B show the evolution in fracture transmissivity with effective normal stress during loading/unloading cycles for Sample J3 with rough (J34) and smooth (J33) surfaces. The acid is applied to the fracture surfaces after the first cycle. The fracture transmissivity decreased as the effective normal stress increased during both loading stages before (black squares) and after (yellow squares) acidizing. Contrastingly, the fracture transmissivity increased during unloading. Also, the chemical dissolution of the carbonate led to an increase in fracture transmissivity (indicated in red arrows in Figure 43A and Figure 43B). The enhancement in fracture transmissivity is determined by the difference between the first point of the loading after the application of acid and the last point of the unloading before acidizing and comparing this value to the initial transmissivity (first point of the loading before the acid application). Then, the increase in transmissivity after acidizing was 9% for the smooth sample and 15% for the rough sample.

Figure 43- Evolution of fracture transmissivity with effective normal stress cycling before and after acidizing the: A- Smooth; and B- Rough fracture surfaces. Fracture transmissivity was improved by 9% on the smooth surface and 15% on the rough sample.



Source: author

Table 5 summarizes the experimental results of the increase in fracture transmissivity after acidizing for all samples tested. There was a greater improvement in the fracture transmissivity along the rough fracture surfaces than the smooth fracture surfaces, as determined for Samples J33 and J34 (Figure 43A and Figure 43B). Additionally, Table 5 shows each rock's Ca, SiO<sub>2</sub>, Al, and Mg contents (data from XRD shown in Table 4).

Table 5- Percentage increase in fracture transmissivity after acidizing with the respective elemental contents for samples with smooth and rough fracture surfaces, for a constant normal stress of 0.55 MPa.

Formation	Sample	Fracture surface	Transmissivity increase (%)	CaO (%)	SiO <sub>2</sub> (%)	Al <sub>2</sub> O <sub>3</sub> (%)	MgO (%)
Jandaíra	J14	rough	32.4	97.64	0.85	0.41	0.52
	J21	smooth	7.0	97.62	0.8	0.38	0.54
	J24	rough	25				
	J33	smooth	9.6	83.78	1.29	0.59	13.00
	J34	rough	15.4				
	J43	smooth	4.0	97.04	1.05	0.54	0.62
	J44	rough	21.6				
Gramame	G13	smooth	6.9	58.05	19.7	7	7.26
	G14	rough	10.3				
M. Farinha	M12	smooth	7.6	80.28	9.97	3.95	1.58

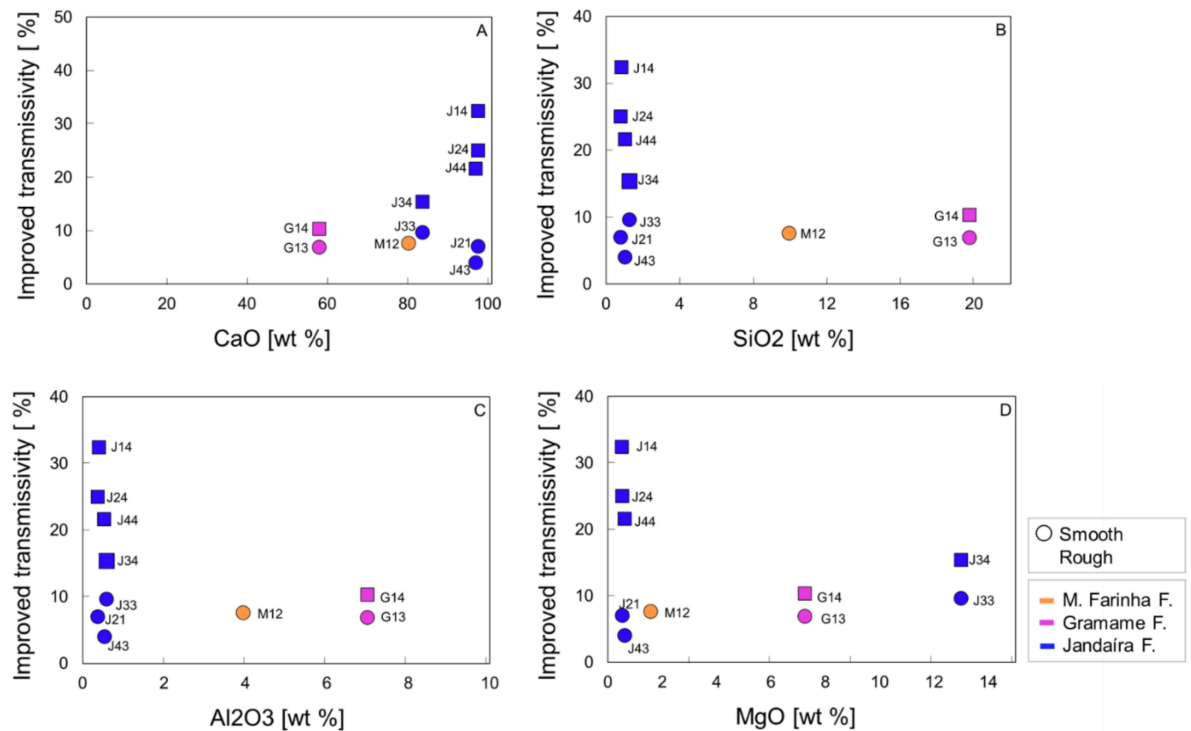
Source: author

Figure 44 presents the data obtained on the increase in fracture transmissivity associated with the different elemental compositions of the samples for Ca, Si, Al, and Mg. The dataset suggests that samples with high Ca contents and low SiO<sub>2</sub>, Al, and Mg.



Mg exhibited the most improvement after acidizing. This was mainly true for the Jandaíra Formation samples (J14, J24, and J44) with rough fracture surfaces (blue squares). Conversely, Samples J43, J21, and J33, which had smooth fracture surfaces (blue circles), showed less than a 7% improvement in fracture transmissivity despite their high Ca contents (83–97%). The rough and smooth surfaces of Samples M12, G13, and G14 showed similar improvements in fracture transmissivity to the smooth Jandaíra samples, regardless of their clay mineral content.

Figure 44- Relationship between increase in fracture transmissivity and content of: A- Ca; B- SiO<sub>2</sub>; C- Al; and D- Mg. The greatest improvement in fracture transmissivity relates to a high Ca content with low SiO<sub>2</sub>, Al, and Mg.



Source: author

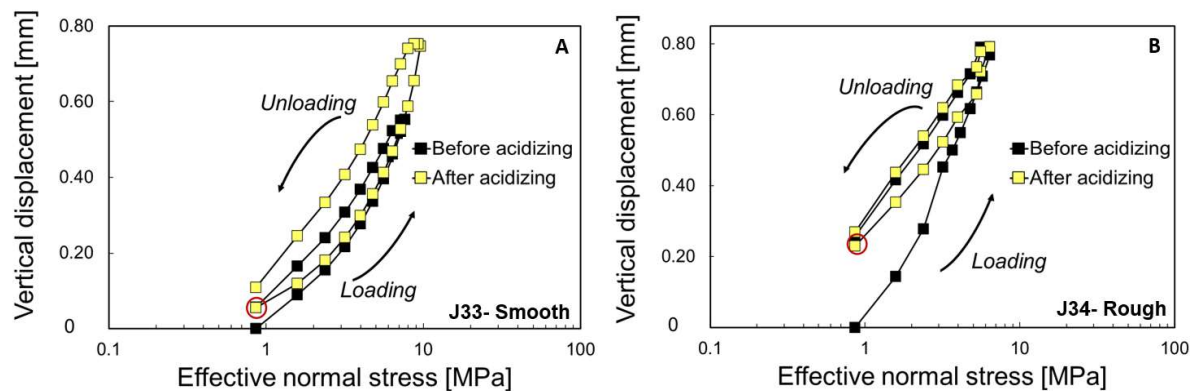
### 7.1.2 Chemo–hydro–mechanical coupling: vertical displacement changes due to chemical dissolution

Figure 45A and Figure 45B show the total vertical displacement (matrix and fracture) as a function of normal stress for the Jandaíra Formation samples with smooth and rough fracture surfaces (J33 and J34, respectively). Normal displacement increased non-linearly during loading. The loading/unloading cycle showed hysteretic behavior in both cases. Figure 45B indicates that the difference between loading and



unloading was more pronounced in the rough sample before the application of the acid. This effect might be explained by the asperities leading to a potential mismatch of the fracture surfaces due to the axial loading, as mentioned in Figure 42. In addition, no significant changes in vertical displacement after acidizing are observed (red circles in Figure 45). This may suggest that chemical dissolution did not modify the contact points between the fracture surfaces, the acid possibly tending to deepen pre-existing cavities, as indicated in Figure 39B.

Figure 45- Vertical displacement as a function of effective normal stress before and after acidizing samples with: A Smooth; and B Rough fracture surfaces. Displacement between the fracture planes evidences the mechanical effect of the fracture (within the same stress cycle). Contrastingly, there was insignificant displacement after applying the acid (red circles).



Source: author

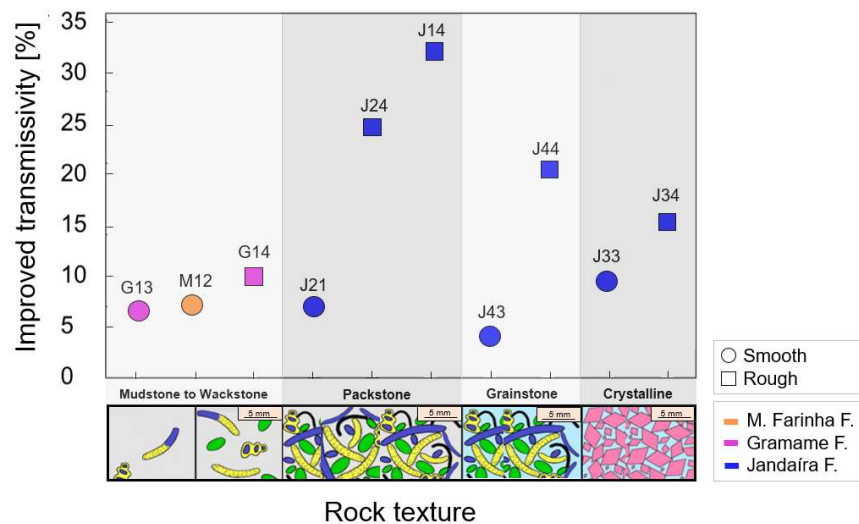
## 7.2 CHEMICAL DISSOLUTION: MINERALOGY, ROCK TEXTURE, AND ROUGHNESS

Figure 46 shows the increase in fracture transmissivity based on rock texture for the smooth (circles) and rough (squares) fracture surfaces. As mentioned, the samples with high Ca contents and rough fracture surfaces experienced improved fracture transmissivity over those with high Ca contents and smooth fracture surfaces. Conversely, the samples with high SiO<sub>2</sub> contents (i.e., relating to the presence of clay minerals in the Gramame and Maria Farinha formation samples) showed less improvement in transmissivity, even with pre-existing surface roughness.

Figure 46 shows samples with a fine-grained matrix (mudstone to wackstone/biomicrite), which exhibits less variation in transmissivity after acidification

despite having rough fracture surfaces (e.g., Sample G14) and more than 50% of carbonate content (Samples M12, G13, G14 - see Table 5 and Figure 44A). A higher grain/particle content in proportion to the rock matrix (Packstones to Grainstone/Biosparite) resulted in a greater increase in transmissivity after acidizing, specifically in samples with rougher surfaces and carbonate content of more than 97% (Samples J14, J24, and J44 in Table 5 and Figure 44A). Samples with a rock fabric dominated by coarse grains exhibited moderate improvements in fracture transmissivity, mainly those with rough fracture surfaces (Samples J33 and J34).

Figure 46- Relationship between enhancement in transmissivity and rock texture after acidizing for all samples. Smooth and rough fracture surfaces are represented by circles and squares, respectively. Surface roughness and carbonate content (Table 5 and Figure 44) impact the chemical dissolution, mainly on surfaces with pre-existing roughness and in rocks with a grain-supported texture (Samples J14, J24, and J44) more than samples with a fine-grained matrix and smooth fracture surfaces (Samples G13 and M12).



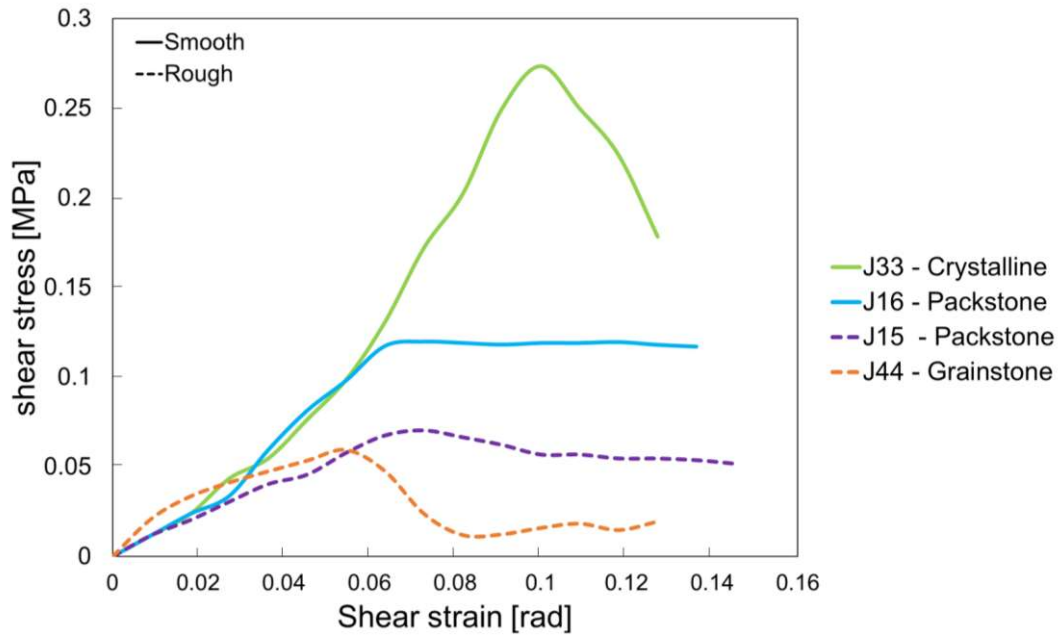
Source: author

### 7.3 FRACTURE TRANSMISSIVITY AS A FUNCTION OF SHEAR STRESS

Figure 47 shows the shear stress – shear strain diagram for Jandaíra Formation rocks with smooth (J33 and J16) and rough surfaces (J15 and J44). When the torque is applied, it causes an increase in the shear stress, particularly pronounced on rocks with smooth surfaces (continuous lines) concerning rough surfaces (dashed lines). Figure 47 illustrates that once the shear stress reaches its maximum value, it may either decrease or become constant. Notably, rock J33 exhibits an abrupt increase in

shear stress, leading to rapid deformation until it breaks at approximately 0.27 MPa. This is followed by a decrease in shear strain and gradual deformation. The crystalline texture of rock J33 suggests its brittleness, explaining the rapid increase in shear stress.

Figure 47- Shear stress and shear strain diagram for Jandaíra Formation rocks with smooth (continuous lines) and rough (dashed lines) surfaces.



Source: author

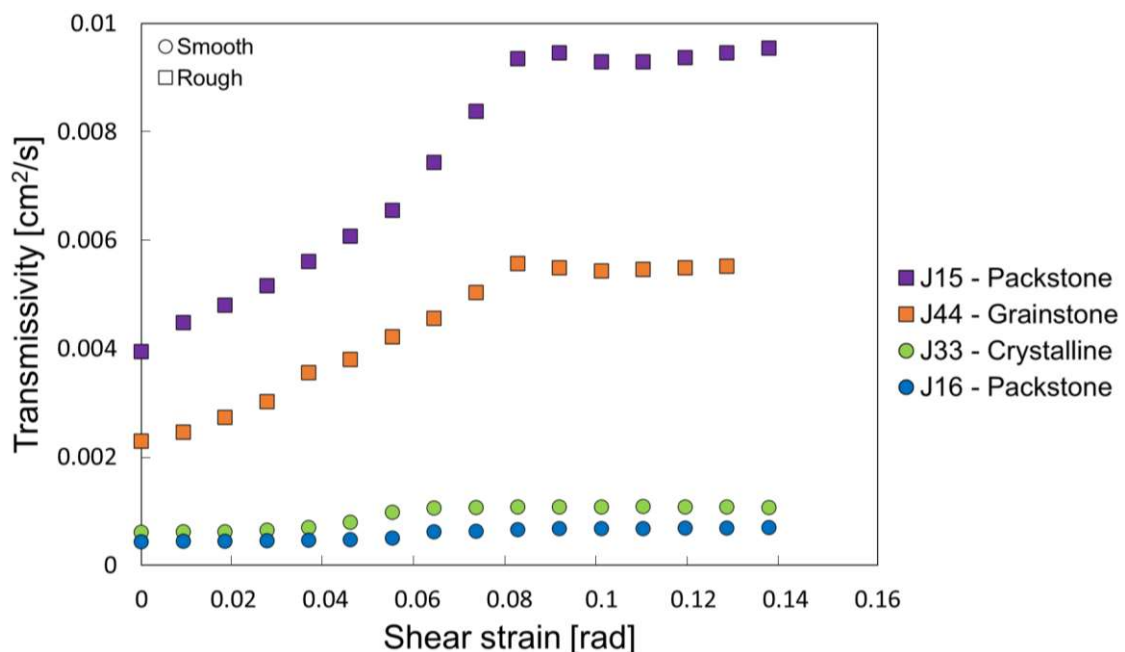
In contrast to rock J33, the torque on rough rocks, J15 and J44 (dashed lines), produces continuum strain at less stress. Rocks J15 and J44 also get a rupture point approximately at 0.07 MPa and 0.06 MPa. The presence of asperities could explain why rough samples first reach the rupture value compared to smooth surfaces. Rough surfaces support less shear stress than smooth surfaces because asperities could break, and the fracture plane would be reorganized when experiencing the torsion displacement.

From the maximum shear stress, rock J15 shows a minimal and gradual deformation at constant shear stress, probably because the asperities' reorganization favors keeping the fluid channel open. In contrast, rock J44 first shows a decrease in shear stress until it finally deforms at constant stress. The rock J16 with a smooth

surface behaves similarly to rocks with a rough surface. However, rock J16 deforms at uniform shear stress when it gets the maximum value (0.12 MPa).

As mentioned in previous results, initial fracture transmissivity is high for rough fractures because asperities favor higher initial mechanical aperture than smooth surfaces. Figure 48 displays fracture transmissivity variation as a function of shear strain. When subjected to torsion displacement, rough rocks (J15 and J44) increase transmissivity between 3-5% compared to smooth rocks (J16 and J33), which increase by less than 1%. Thus, rocks with smooth surfaces exhibit the least fracture transmissivity, which may be because they experienced higher shear stress and rapid rupture and deformation (e.g., rock J33 in Figure 47).

Figure 48- Fracture transmissivity variations with shear strain from a torsion displacement applied on rocks of the Jandaira Formation. Squares represent rocks with rough surfaces, and circles represent smooth ones.



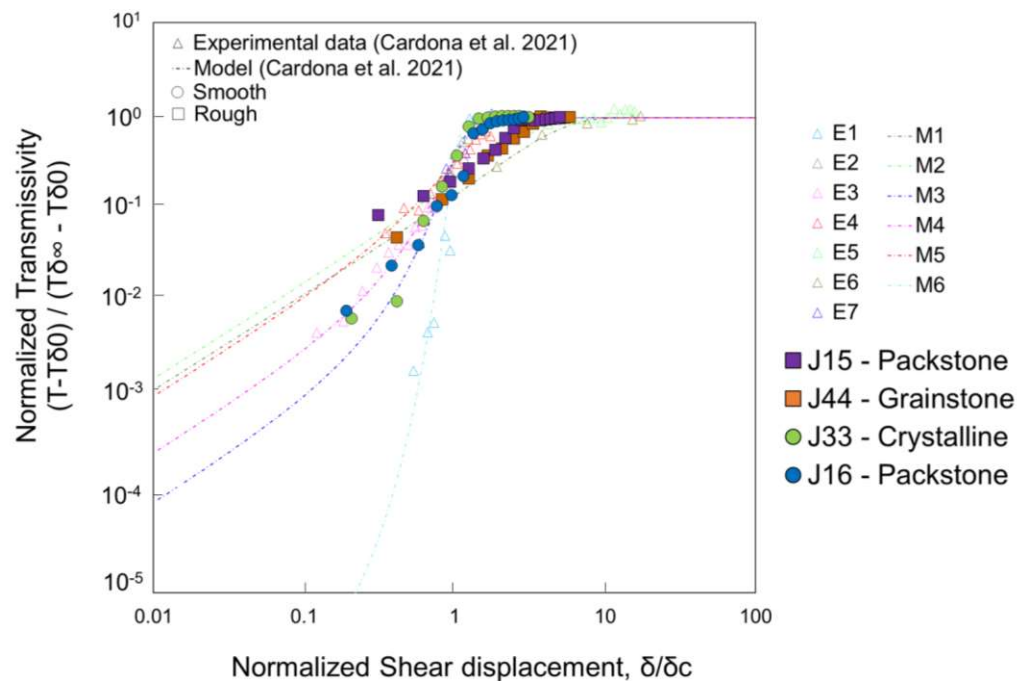
Source: author

Sample J15 reaches the maximum fracture transmissivity value of  $9 \times 10^{-3} \text{ cm}^2/\text{s}$ , while rock J44 reaches  $5 \times 10^{-3} \text{ cm}^2/\text{s}$ . Roughness rocks reached low shear stress (dashed lines in Figure 47), which could explain why fracture transmissivity increased, even if the fracture experienced mismatching and asperities broke due to the torsion. Figure 48 also shows a constant behavior of transmissivity after reaching their

maximum value, close to the strains of 0.06 rad and 0.08 rad for smooth and rough surfaces, respectively.

Fracture transmissivity and shear displacement data of the Jandaíra Formations were normalized using a fitted logistic model proposed by Cardona, Finkbeiner and Santamarina (2021). The implemented model to normalize the data is described above in section 3.2.1.3. The normalized data provides a “relative” transmissivity value for understanding the overall behavior of how transmissivity varies with shear displacement for different carbonate rocks. Figure 49 presents a normalized transmissivity as a function of the normalized shear displacement. The data plot of this figure includes Jandaíra Formation rocks of this study with rough (squares – rocks J15 and J44) and smooth (circles – rocks J33 and J16) surfaces; experimental data of limestone from the Middle East (empty triangles) and data of numerical simulations (lines), data published in Cardona, Finkbeiner and Santamarina (2021). The type of surface roughness is not specified for the Middle East’s limestones.

Figure 49- Transmissivity as a function of shear displacement due to torsion – Jandaíra Formation rocks with rough (filled squares - J15 and J44) and smooth surfaces (filled circles - J33 and J16); and experimental data (empty triangles) and fitted logistic model (lines) developed by Cardona, Finkbeiner and Santamarina (2021).



Source: author

Figure 49 suggests changes in fracture transmissivity are sensitive to initial mechanical aperture and surface roughness. The transmissivity changes of the rocks of the Jandaíra Formation behave asymptotically like the limestones of the Middle East. The figure shows that Jandaíra rough rocks gradually increase transmissivity while supporting deformation more than Jandaíra smooth samples that rapidly increase transmissivity at lower shear displacement (as described previously in Figure 47 and Figure 48).

## **SECTION 4 – CONCLUDING REMARKS**

### **CHAPTER 8 – DISCUSSION, CONCLUSIONS AND RECOMMENDATIONS**

This chapter discusses previous works and contributions of this research, summarizes the findings of this study in the conclusions, and exposes how future research could continue the knowledge contribution in this study area.

#### **8.1 FINAL DISCUSSION**

During the experiments, the fracture surface roughness increased to different degrees on both the smooth and rough surfaces due to the dissolution caused by the HCl acid and shear displacement.

After acidizing the samples, etched patterns, including irregular asperities, micropits, cavities, and channels, modified their fracture surface topographies, consistent with previous observations (Neumann et al. 2012; Pournik et al. 2009). As reported by Nino-Penaloza et al. (2015), at the fine scale, irregular micropits formed on the smooth surfaces due to the dissolution of microasperities, whereas on the rough surfaces, pre-existing microcavities were deepened and microchannels formed, as observed by Pournik et al. (2009). From the experimental measurements (Figure 45) and roughness profile analyses (Figure 39B), this research confirmed previous reporting by Cardona, Finkbeiner and Santamarina (2021) that chemical dissolution does not significantly affect the actual contact area of the fracture plane. Additionally, this study found that, during stress cycling, surfaces with pre-existing roughness and clay minerals present higher deformability and changes in fracture aperture (irreversible behavior), consistent with the experimental results of Wu et al. (2020), who determined a decrease in rock strength due to the presence of clay minerals. In particular, the Maria Farinha and Gramame formation samples tended to deform plastically due to the presence of clay minerals (Barbosa 2004, 2007). Conversely, the Jandaíra Formation samples exhibited greater strength than the Maria Farinha and Gramame formation samples due to the presence of silica cement in the former (Bertotti et al. 2017; Córdoba 2001).

Our results also confirm the relationship between chemical dissolution and fracture surface roughness after acid treatment. We found that carbonate minerals promoted dissolution in the Jandaíra Formation samples, while the presence of clay minerals reduced this effect in the Maria Farinha and Gramame formation samples. Similarly, studies by Jia et al. (2017); Jin et al. (2020), and Mou et al. (2010) have described surface changes due to acidizing as a function of carbonate mineral content. From this study, it is understood that the mineralogical composition of the rock influenced the intensity and pattern of dissolution on the fracture surface because of the control exerted by the grain size and distribution (Ng and Santamarina 2022), fracture surface topography (Wu et al. 2020), and hence the mechanical and hydraulic apertures (Dong 2020; Lai et al. 2019).

The experiments demonstrated that, after acidizing, the fracture transmissivity improved more in samples with rough surfaces (Asadollahpour et al. 2018; Nino-Penaloza et al. 2015) than smooth surfaces (Table 4). Overall, our findings contribute to our understanding of how improvements in fracture transmissivity, resulting from the application of HCl acid, are influenced by surface roughness, normal stress, chemical composition, as well as grain size and distribution (rock texture). Thus, this study led to our observing the following relationship—grain-supported rocks with a high Ca content, such as packstones to grainstones with a sparite matrix, exhibit the most significant increase in fracture transmissivity after acidizing, especially when the surface has pronounced initial roughness. Moreover, matrix-supported rocks dominated by micritic crystals (mudstones and wackstones) with fine allochem grains that contain clay minerals or exhibit dolomitization, demonstrate a lower transmissivity increase because of the acidizing, even with the condition of pre-existing roughness on the fracture surfaces.

Although the number of samples implemented during the torsion test is not enough to broadly discuss the effects of shear stress on fracture roughness, punctually, it was observed that slip by torsion produces changes in fracture transmissivity. The carbonate rocks tested in this study show that smooth fracture surfaces experienced rapid deformation or rupture at low shear stress, whereas rough surfaces get deformed more at high shear stress, as observed by Xu and Freitas (1988). Rough fractures show better transmissivity values than smooth ones because



roughness and matedness (Cardona; Finkbeiner; Santamarina, 2021) favor the initial mechanical aperture and define the evolution of the fluid through the fracture when subjected to shear displacement. Furthermore, this study reveals that in addition to roughness, the rock texture and mineral composition may impact the mechanical response of the rock when it is subjected to shear displacement.

## 8.2 CONCLUSIONS

This study finds that the effect of acid on fracture transmissivity depends on a variety of characteristics, including its roughness, the host rock's mineralogical composition, the rock texture, and the load normal to its surface. The main conclusions are as follows:

- 1- Chemical dissolution in response to HCl treatment along fracture surfaces preferentially creates micropits on smooth surfaces and microchannels on pre-existing rough surfaces, thus enhancing fluid flow along the fracture.
- 2- After the acid effect the level of fracture transmissivity increases with surface roughness.
- 3- Rocks with a high carbonate content exhibited a higher dissolution effect, which increased fracture transmissivity compared to rocks containing clay minerals, siliciclastics, and dolomite grains. This effect suggests that calcite grains react strongly to acid compared to other minerals.
- 4- For the loads (i.e., normal stress values) employed on our fracture samples, acidification does not significantly impact a fracture's mechanical response, irrespective of whether the surface is smooth or rough.
- 5- In the case of the results previous to acidification, the increasing normal stress mechanically impacts a fracture's aperture, especially in rocks containing asperities and those rich in clay minerals.

6- Grain-supported rocks with a high carbonate content exhibit the greatest fracture transmissivity enhancement after acidification, particularly in fractures with rough surfaces. The results suggest that acid dissolves preexisting cavities and tends to form channels, thereby enhancing fluid flow through these formed pathways.

7- Changes in fracture transmissivity due to shear displacement are sensitive to initial mechanical aperture, rock texture, and surface roughness.

### 8.3 FUTURE WORK

While this research contributes valuable insights into the effects of roughness, rock texture, and mineral composition on chemical and mechanical changes, several areas warrant exploration. Future research could include:

- Computational tomography scans before and after acidizing to understand the dissolution process on carbonate rocks relating to the mineral's lost mass quantity.
- Explore statistical tools to evaluate and analyze the distribution of asperity heights before and after acidizing.
- Use photos acquired during the experiments to study fracture aperture changes during loading and unloading.
- Develop torsion and acidification experiments on a diverse range of rock textures, enabling the identification of patterns in transmissivity alterations resulting from chemical and hydromechanical influences.
- Apply and validate the methodology of the strong discontinuities and the fracture closure Barton-Bandis constitutive model cited in (Bandis; Lumsden; Barton, 1983; Beserra et al., 2018; Manzoli et al., 2016) with the experimental results, using the in-house CODE\_BRIGHT simulator - COupled DEformation BRIne Gas and Heat Transport developed by Guimarães, Gens, Olivella (2007); Olivella et al. (1996).
- Validate the experimental results of fracture transmissivity changes due to shear stress in a 3D model using the CODE\_BRIGHT simulator.

- The experimental data should be integrated into commercial reservoir flow simulators to improve accuracy and performance. This enhancement will lead to more reliable simulations and better reservoir management.

## BIBLIOGRAPHIC REFERENCES

- Aguilera, R. (1995). Naturally fractured reservoirs. In *Second edition* (Second, pp. 1–528).
- Aguilera, R. (2003). Geologic and engineering aspects of naturally fractured reservoirs. *Canadian Society of Exploration Geophysicists*, 28(02), 1–13. <https://doi.org/10.1190/1.1437912>
- Ahoua, D., and Hincapie, F. (2008). Comprehensive Review of Key Parameters for Surfactant Polymer Flooding Design in Carbonates. *ITE Seminar S6181 ‘Seminar Petroleum Engineering’*. <https://doi.org/10.13140/RG.2.1.1749.2086>
- Akbar, M., Vissapragada, B., Alghamdi, A., Allen, D., Herron, M., Carnegie, A., Dutta, D., Olesen, J. (2015). *A Snapshot of Carbonate Reservoir Evaluation*. <https://www.researchgate.net/publication/280020441>
- Alameedy, U., Alhaleem, A., Isah, A., Al-Yaseri, A., Mahmoud, M., Salih, I. (2022). Effect of acid treatment on the geomechanical properties of rocks: an experimental investigation in Ahdeb oil field. *Journal of Petroleum Exploration and Production Technology*, 12(12), 3425–3441. <https://doi.org/10.1007/s13202-022-01533-x>
- Alameedy, U., Fatah, A., Abbas, A., Al-Yaseri, A. (2023). Matrix acidizing in carbonate rocks and the impact on geomechanical properties: A review. *Fuel*, 349, 1–10. <https://doi.org/10.1016/j.fuel.2023.128586>
- Al-Harthy, S., Dennis, J., Y., & Jing, X., Marsden, J. (1998). Hysteresis, True-Triaxial Stress-Path and Pore Pressure Effects on Permeability. *Society of Petroleum Engineers, SPE 47269*(July), 1–9. <https://doi.org/10.2118/47269-MS>
- Al-Momin, A., Zhu, D., Hill, A. D. (2014). The effects of initial condition of fracture surfaces, acid spending and acid type on conductivity of acid fracture. *Proceedings of the Annual Offshore Technology Conference*, 3, 1934–1948. <https://doi.org/10.4043/24895-ms>
- Araújo, R., La Bruna, V., Rustichelli, A., Bezerra, F., Xavier, M., Audra, P., Barbosa, J. A., Antonino, A. (2021). Structural and sedimentary discontinuities control the generation of karst dissolution cavities in a carbonate sequence, Potiguar Basin, Brazil. *Marine and Petroleum Geology*, 123(October 2020). <https://doi.org/10.1016/j.marpetgeo.2020.104753>
- Archer, R. (2008). Impact of Stress Sensitive Permeability on Production Data Analysis. *Society of Petroleum Engineers, SPE 114166*(February), 1–9.

- Asadollahpour, E., Baghbanan, A., Hashemolhosseini, H., Mohtarami, E. (2018). The etching and hydraulic conductivity of acidized rough fractures. *Journal of Petroleum Science and Engineering*, 166(January), 704–717. <https://doi.org/10.1016/j.petrol.2018.03.074>
- Auradou, H. (2009). Influence of wall roughness on the geometrical, mechanical and transport properties of single fractures. *Journal of Physics D: Applied Physics*, 42(21). <https://doi.org/10.1088/0022-3727/42/21/214015>
- Bagheri, M., and Settari, A. (2005). Modeling of Geomechanics in Naturally Fractured Reservoirs. *Society of Petroleum Engineers, SPE 93083*(February), 1–12.
- Bagni, F., Erthal, M., Tonietto, S., Maia, R., Bezerra, F., Balsamo, F., Córdoba, V., de Souza, F., Brod, J., Fernandes, C., Fonseca, J. (2022). Karstified layers and caves formed by superposed epigenic dissolution along subaerial unconformities in carbonate rocks – Impact on reservoir-scale permeability. *Marine and Petroleum Geology*, 138(January). <https://doi.org/10.1016/j.marpetgeo.2022.105523>
- Bai, M., Meng, F., Roegiers, J.C., Green, S. (2002). Improved Determination of Stress-Dependent Permeability for Anisotropic Formations. *Proceedings of SPE/ISRM Rock Mechanics Conference, SPE 78188*. <https://doi.org/10.2523/78188-MS>
- Baker, R.O., and Kuppe, F. (2000). Reservoir characterization for naturally fractured reservoirs. *Society of Petroleum Engineers, SPE 63286*(October), 1–11. <https://doi.org/10.2118/63286-MS>
- Bandis, S. C., Lumsden, A. C., Barton, N. R. (1983). Fundamentals of Rock Joint Deformation. *International Journal of Rock Mechanics and Mining Science*, 20(6), 249–268.
- Barbosa, A., and Lima Filho, M. (2006). Aspectos estruturais e estratigráficos da faixa costeira Recife-Natal: observações em dados de poços. *Boletim de Geociencias Da Petrobras*, 14(1), 287–306.
- Barbosa, J. A. (2004). Evolução da Bacia da Paraíba durante o Maastrichtiano-Paleoceno: formações Gramame e Maria Farinha, NE do Brasil. In *Universidade Federal de Pernambuco*.
- Barbosa, J. A. (2007). A deposição Carbonática na Faixa Recife-Natal: Aspectos Estratigráficos, Geoquímicos e Paleontológicos. In *Universidade Federal de Pernambuco*.
- Barbosa, J. A., Filho Lima, M., Neumann, V. (2003). A estratigrafia da bacia paraíba: uma reconsideração. *Estudos Geológicos*, 13, 89–108.

- Barbosa, J. A., Neumann, V. H., Lima Filho, M., Souza, E. M., Moraes, M. A. (2007). Estratigrafia da Faixa Costeira Recife-Natal (Bacia Da Paraíba e Plataforma de Natal), NE Brasil. *Estudos Geológicos*, 17(2), 3–30.
- Barton, C.A., Zoback, M.D., Moos, D. (1995). Fluid flow along potentially active faults in crystalline rock. *Geology*, 23(8), 683–686.
- Barton, N., Bandis, S., Bakhtar, K. (1985). Strength, Deformation and Conductivity Coupling of Rock Joints. *J Rock Mech Mm Sci & Geomech*, 22(3), 121–140.
- Becker, I., Koehrer, B., Waldvogel, M., Jelinek, W., Hilgers, C. (2018). Comparing fracture statistics from outcrop and reservoir data using conventional manual and t-LiDAR derived scanlines in Ca<sub>2</sub> carbonates from the Southern Permian Basin, Germany. *Mar Pet Geol* 95(2018):228-245. <https://doi.org/10.1016/j.marpetgeo.2018.04.021>.
- Beer J, Jhonston R, Dewolf J. (2006). *Mechanics of materials* (Vol. 4).
- Bennion, D. B. (1999). Formation Damage-The Impairment of the Invisible, by the Inevitable and Uncontrollable, Resulting in an Indeterminate Reduction of the Unquantifiable! *Journal of Canadian Petroleum Technology*, 38(2), 11–17. <https://doi.org/10.2118/99-02-DA>
- Bennion, D. B. (2002). An overview of formation damage mechanisms causing a reduction in the productivity and injectivity of oil and gas producing formations. *Journal of Canadian Petroleum Technology*, 41(11), 29–36. <https://doi.org/10.2118/02-11-DAS>
- Bentosa, E. (2010). Geomecânica aplicada a la industria petrolera. *Schlumberger Geomechanics (SGM)*, 1–36.
- Bertuzzi, F., Sanfilippo, F., Bngnoli, M., Parravicini, G. (1998). Characterization of flow within natural fractures: numerical simulations and field aDDlications. *Society of Petroleum Engineers, SPE 47268*(July), 337–345. <https://doi.org/10.2523/47268-MS>
- Beserra, L., Guimarães, L., Manzoli, O. L., Berrio, L. (2018). Finite element with embedded discontinuities analysis of well production decline due to fracture closure in naturally fr. *16th European Conference on the Mathematics of Oil Recovery, ECMOR 2018, September 2018*. <https://doi.org/10.3997/2214-4609.201802156>
- Beurlen, K. (1967). Estratigrafia da faixa sedimentar costeira Recife-João Pessoa. *Boletim Geologico*, 16(1), 43–53.

- Bin, Z.H., Amar, T., Altunbay, M., Barr, D. (1995). Stress sensitivity in the dulang field - how it is related to productivity. *Society of Petroleum Engineers, SPE* 30092(May), 1–19.
- Brown, S. R. (1987). Fluid flow through rock joints: the effect of surface roughness. *Journal of Geophysical Research*, 92(B2), 1337–1347. <https://doi.org/10.1029/JB092iB02p01337>
- Bruno, M.S., Bovberg, C.A., Nakagawa, E. M. (1991). Anisotropic stress influence on the permeability of weakly-cemented sandstones. *American Rock Mechanics Association*, 375(March), 375–383. [https://doi.org/10.1016/0148-9062\(92\)93848](https://doi.org/10.1016/0148-9062(92)93848)
- Buchsteiner, H., and Warpinski, N. R. (1993). Stress-Induced Permeability Reduction in Fissured Reservoirs. *Society of Petroleum Engineers, SPE* 26513(October), 65–74.
- Camacho, J.F., Reyes-Ortiz, O., Nieto, A., Millán, S., Rincón, F. (2009). Strength To the Cutting in Discontinuities With Different Degrees of Roughness. *Scientific Electronic Library Online (Scielo)*, 19(1), 55–70.
- Cardona, A. (2020). *Fluid Transport in Fractured Carbonate Rocks*.
- Cardona, A., Finkbeiner, T., Santamarina, J. C. (2021). Natural Rock Fractures: From Aperture to Fluid Flow. *Rock Mechanics and Rock Engineering*, 54(11), 5827–5844. <https://doi.org/10.1007/s00603-021-02565-1>
- Chen, C., Wang, S., Lu, C., Wang, K., Lai, J., Liu, Y., Liu, T., Liu, D. (2021). The Impact of Surface Roughness and Injection Rate on Acid-fracture Conductivity. *55th U.S. Rock Mechanics / Geomechanics Symposium 2021*, 2(2015).
- Chen, Y., Liang, W., Lian, H., Yang, J., Nguyen, V. (2017). Experimental study on the effect of fracture geometric characteristics on the permeability in deformable rough-walled fractures. *International Journal of Rock Mechanics and Mining Sciences*, 98, 121–140. <https://doi.org/10.1016/j.ijrmms.2017.07.003>
- Chilingar, G., Bissell, H., Fairbridge, R. (1967). Carbonate rocks: origin, occurrence and classification. In *Development in sedimentology* (pp. 1–444).
- Chilingarian, G., Mazzullo, S., Rieke, H. (1992). *Carbonate Reservoir Characterization: A Geologic-Engineering Analysis, Part I*.
- Córdoba, V. (2001). *A evolução da plataforma Carbonática Jandaíra durante o neocretáceo na Bacia Potiguar: análise paleoambiental, diagenética e estratigráfica*. Universidade Estadual Paulista.

- Córdoba, V., Jardim De Sá, E., Sousa, D., Antunes, A. (2007). Bacia de Pernambuco-Paraíba. In *Boletim de Geociências da Petrobras* (Vol. 15, Issue 2).
- Costa de Melo, A., de Castro, D., Bezerra, F., Bertotti, G. (2016). Rift fault geometry and evolution in the Cretaceous Potiguar Basin (NE Brazil) based on fault growth models. *Journal of South American Earth Sciences*, 71, 96–107. <https://doi.org/10.1016/j.jsames.2016.07.006>
- Crawford, B., and Smart, B. (1994). The Influence of Stress Anisotropy on Horizontal Well Performance Predicted Via Special Core Analysis Under True Triaxial Conditions. *Society of Petroleum Engineers, SPE 28452*(September), 923–935.
- Davies, J.P., and Davies, D. K. (1999). Stress-Dependent Permeability: Characterization and Modeling. *Society of Petroleum Engineers, SPE 56813*(October), 1–16.
- Davies, J.P., and Davies, D. K. (2001). Reservoir Stress Changes Induced by Production/Injection. *Society of Petroleum Engineers, SPE 71750*(May), 1–8. <https://doi.org/10.2118/71750-PA>
- de Castro, D., Bezerra, F., Sousa, M., Fuck, R. (2012). Influence of Neoproterozoic tectonic fabric on the origin of the Potiguar Basin, northeastern Brazil and its links with West Africa based on gravity and magnetic data. *Journal of Geodynamics*, 54, 29–42. <https://doi.org/10.1016/j.jog.2011.09.002>
- De Matos, R. M. (1992). The Northeast Brazilian rift system. *Tectonics*, 11(4), 766–791. <https://doi.org/10.4324/9780203494219-10>
- Deng, J., Texas, A., Mou, J., Hill, A. D. (2011). A New Correlation of Acid Fracture Conductivity Subject to Closure Stress. *SPE - Hydraulic Fracturing Technology Conference*, 140402.
- Di Toro, G., Niemeijer, A., Tripoli, A., Nielsen, S., Di Felice, F., Scarlato, P., Spada, G., Alessandroni, R., Romeo, G., Di Stefano, G., Smith, S., Spagnuolo, E., Mariano, S. (2010). From field geology to earthquake simulation: A new state-of-The-art tool to investigate rock friction during the seismic cycle (SHIVA). *Rendiconti Lincei*, 21(SUPPL. 1), 95–114. <https://doi.org/10.1007/s12210-010-0097-x>
- Dielman, S. (2005). Ground Water Hydrology. In *Hydraulic Conductivity/Transmissibility* (Vol. 1, pp. 507–514). Wiley. <https://doi.org/10.1002/047147844x.gw481>



- Dong, C., Hill, A., Zhu, D. (1999). Acid etching patterns in naturally-fractured formations. *Proceedings - SPE Annual Technical Conference and Exhibition*, 56531, 227–234. <https://doi.org/10.2118/56531-ms>
- Dong, C., Zhu, D., Hill, A. (2001). Acid Penetration in Natural Fracture Networks. *SPE - European Formation Damage Conference*, 68927, 18.
- Dong, C., Zhu, D., Hill, A. D. (2002). Acidizing in Naturally Fractured Carbonate Reservoirs. *SPE/DOE Improved Oil Recovery Symposium*, 75252, 1–11.
- Dorta, G., Boujana, M., Zerpa, L., Ramonez, M., Velasquez, C., Castillo, E. (2001). An Approach to Naturally Fractured Reservoir Characterization : Case Study, San Juan Formation, Orocual Field, Venezuela. *Society of Petroleum Engineers, SPE* 69471, 1–8.
- Du, J., and Wong, R. C. (2002). Stress-induced Permeability Anisotropy in Fractured Reservoir. *Society of Petroleum Engineers, SPE* 79019(November), 1–8. <http://www.onepetro.org/mslib/servlet/onepetropreview?id=00079019>.
- Dunham, R. (1962). Classification of Carbonate Rocks According to Depositional Textures. *Classification of Carbonate Rocks--A Symposium*, 108–121.
- Eberli, G., Baechle, G., Anselmetti, F., Incze, M. (2003). Factors controlling elastic properties in carbonate sediments and rocks. The leading edge. July. <https://doi.org/10.1190/1.1599691>
- Economides, M.J., Buchsteiner, H., Warpinski, N. R. (1994). Step-pressure test for stress-sensitive permeability determination. *Society of Petroleum Engineers, SPE* 27380, 359–367. <https://doi.org/10.2118/27380-MS>
- El Gadi, M., and Brookfield, M. (1999a). Open carbonate ramp facies, microfacies and paleoenvironments of the Gramame Formation (Maastrichtian), Pernambuco-Paraiba Basin, Northeastern Brazil. *Journal of South American Earth Sciences*, 12(4), 411–433. [https://doi.org/10.1016/S0895-9811\(99\)00027-9](https://doi.org/10.1016/S0895-9811(99)00027-9)
- Esaki, T., Du, S., Mitani, Y., Ikusada, K., Jing, L. (1999). Development of a shear-flow test apparatus and determination of coupled properties for a single rock joint. *international Journal of Rock Mechanics and Mining Sciences*, 36, 641–650. [www.elsevier.com/locate/ijrmms](http://www.elsevier.com/locate/ijrmms)
- Euskal Herriko Unibertsitatea. (2011). *Metrología del acabado superficial*.
- Farahmand, K., and Diederichs, M. S. (2014). Modeling of Stress-Induced Permeability Change With Progressive Damage in Intact Rock Using a Micro-Mechanical Approach. *American Rock Mechanics Association*, 7021(June), 1–8.

- Finkbeiner, T., Barton, C.A., Zoback, M. D. (1997). Relationships Among In-Situ Stress, Fractures and Faults, and Fluid Flow: Monterey Formation, Santa Maria Basin, California. *AAPG Bulletin*, 81 (1997)(12), 1975–1999. <https://doi.org/10.1306/3B05C6FE-172A-11D7-8645000102C1865D>
- Fjaer, E., Holt, R. M., Horsrud, P., Raaen, A. M., Risnes, R. (2008). Petroleum Related Rock Mechanics. In *Elsevier* (Second edi, Vol. 1, Issue 2). [https://doi.org/10.1016/0148-9062\(93\)92632-Z](https://doi.org/10.1016/0148-9062(93)92632-Z)
- Forstner, S., Laubach, S. (2022). Scale-dependent fracture networks. *Journal of Structural Geology*, 165. <https://doi.org/10.1016/j.jsg.2022.104748>
- Gale, J. E. (1982). The effects of fracture type (induced versus natural) on the stress-fracture closure-fracture permeability relationships. *American Rock Mechanics Association*, 290(July), 290–298. <https://doi.org/ARMA-82-290>
- Galindo, K., Guimarães, L., Lins, C., Lima, A., Santos, Y., Gomes, I. (2021). Minerals Dissolution Effect on the Mechanical Properties of Synthetic Carbonatic Rocks under a Reactive Fluid Injection. *American Scientific Research Journal for Engineering*, 1, 1–33. <http://asrjetsjournal.org/>
- Gertsch, B., Keller, G., Adatte, T., Berner, Z. (2013). The Cretaceous-Tertiary boundary (KTB) transition in NE Brazil. *Journal of the Geological Society*, 170(2), 249–262. <https://doi.org/10.1144/jgs2012-029>
- Ghoochaninejad, H., Asef, M., & Moallemi, S. (2018). Estimation of fracture aperture from petrophysical logs using teaching–learning-based optimization algorithm into a fuzzy inference system. *Journal of Petroleum Exploration and Production Technology*, 8(1), 143–154. <https://doi.org/10.1007/s13202-017-0396-1>
- Ghosh, S., Galvis-Portilla, H., Klockow, C., Slatt, R. (2018) An application of outcrop analogues to understanding the origin and abundance of natural fractures in the Woodford Shale. *J Pet Sci Eng* 164(2018):623-639. <https://doi.org/10.1016/j.petrol.2017.11.073>
- Giacomini, A., Buzzi, O., Ferrero, A. M., Migliazza, M., Giani, G. P. (2008). Numerical study of flow anisotropy within a single natural rock joint. *International Journal of Rock Mechanics and Mining Sciences*, 45(1), 47–58. <https://doi.org/10.1016/j.ijrmms.2007.04.007>
- Giraldo, L., Chen, H.Y., Teufel, L. (2000). Field Case Study of Geomechanical Impact of Pressure Depletion in the Low-Permeability Cupiagua Gas-Condensate

- Reservoir. *Society of Petroleum Engineers, SPE* 60297(March), 1–10.  
<https://doi.org/10.2523/60297-MS>
- Gong, M., and Lacote, S. (1998). A New Model of Acid Fracture Conductivity Based on Deformation of Surface Asperities. *Society of Petroleum Engineering*, 39431, 1–15. <http://onepetro.org/SPEFD/proceedings-pdf/98FD/All-98FD/SPE-39431-MS/1940196/spe-39431-ms.pdf/1>
- Gou, B., Qin, N., Wang, C., Ren, J., Guo, J. (2021). Acidizing Model to Couple the Closure Stress and Acid-rock Reactive Transport in Naturally Fractured Carbonate Reservoir. *55th US Rock Mechanics/Geomechanics Symposium*, 21(121).
- Grupo Tecnología Mecánica - GTM. (2017). *Rugosidad superficial*.
- Guimarães, L. D. N., Gens, A., Olivella, S. (2007). Coupled thermo-hydro-mechanical and chemical analysis of expansive clay subjected to heating and hydration. *Transport in Porous Media*, 66(3), 341–372. <https://doi.org/10.1007/s11242-006-0014-z>
- Guo, T., Li, Y., Ding, Y., Qu, Z., Gai, N., Rui, Z. (2017). Evaluation of Acid Fracturing Treatments in Shale Formation. *Energy Fuels*, 31(10), 10479–10489. <https://doi.org/10.1021/acs.energyfuels.7b01398>
- Gutierrez, M., Øino, L., Nygård, R. (2000). Stress-dependent permeability of a de-mineralised fracture in shale. *Marine and Petroleum Geology*, 17(8), 895–907. [www.elsevier.com/locate/marpetgeo](http://www.elsevier.com/locate/marpetgeo)
- Hassan, A., Tariq, Z., Al-Abdrabalnabi, R., Aljawad, M., Mahmoud, M. (2022). Evaluating the Impact of Rock Hardness and Roughness on Acid Fracturing Conductivity. *International Petroleum Technology Conference*, 1–9. <https://doi.org/10.2523/IPTC-22478-MS>
- Hibbeler R. (2009). *Resistência dos materiais* (Vol. 7).
- Holt, R. M. (1990). Permeability Reduction Induced by a Nonhydrostatic Stress Field. *SPE Formation Evaluation, SPE* 19595(December), 444–448. <https://doi.org/10.2118/19595-PA>
- Hommel Etamic. (2022). *Surface texture parameters in practice*. [www.hommel-etamic.com](http://www.hommel-etamic.com)
- Homuth, S., and Sass, I. (2014) Outcrop Analogue vs. Reservoir Data: Characteristics and Controlling Factors of Physical Properties of the Upper Jurassic Geothermal

Carbonate Reservoirs of the Molasse Basin, Germany. In: Proceedings of 38th Works on Geoth Res Eng Stanford, California, USA, 24-26 February, 2014.

- Hosseini, A., Rasouli, V., Bahrami, H. (2010). Analytical and numerical analysis of fluid flow through rough natural fracture profiles. *American Rock Mechanics Association*, 218(June), 1–6.
- Jia, Y., Lu, Y., Elsworth, D., Fang, Y., Wang, C., Tang, J. (2017). Hydro-Mechanical-Chemical Effects on Permeability Evolution of Fractures in Longmaxi Shale. *American Rock Mechanics Association*, 17(296), 9.
- Jin, M., Somerville, J., Smart, B. G. (2000). Coupled Reservoir Simulation Applied to the Management of Production Induced Stress-Sensitivity. *Society of Petroleum Engineers, SPE 64790*(November), 1–12. <https://doi.org/10.2118/64790-MS>
- Jin, X., Zhu, D., Hill, A., McDuff, D. (2020). Effects of Heterogeneity in Mineralogy Distribution on Acid-Fracturing Efficiency. *SPE Production and Operations*, 35(1), 147–160. <https://doi.org/10.2118/194377-PA>
- Jing, L., and Stephansson, O. (1995). Mechanics of Geomaterial Interfaces Mechanics of Rock Joints: Experimental Aspects. *Mechanics of Geomaterial Interfaces*, 317–342.
- Jones, F. (1975). A Laboratory Study of the Effects of Confining Pressure on Fracture Flow and Storage Capacity in Carbonate Rocks. *Society of Petroleum Engineers, SPE 4569*(January), 21–27. <https://doi.org/10.2118/4569-PA>
- Kasap, E., and Bush, E. S. (2003). Estimating a Relationship between Pore Pressure and Natural Fracture Permeability for Highly Stressed Reservoirs. *Society of Petroleum Engineers, SPE 84410*(October), 1–8. <https://doi.org/10.2523/84410-MS>
- Kegel, W. (1954). Nota sobre os microfósseis do fosfato cretáceo de Pernambuco. *Boletim Da Sociedade Brasileira de Geologia*, 3 (1), 73–76.
- Kersey, D. G. (1986). The Role of Petrographic Analyses in the Design of Nondamaging Drilling, Completion, and Stimulation Programs. *Society of Petroleum Engineers, SPE 14089*(March), 1–8.
- Krueger, R. F. (1988). An Overview of Formation Damage and Well Productivity in Oilfield Operations: An Update. *Society of Petroleum Engineers, SPE 17459*(March), 535–552. <https://doi.org/10.2118/10029-PA>

- Lacote, S. (1999). A New Model of Acid Fracture Conductivity Based on Deformation of Surface Asperities. *SPE - International Symposium on Formation Damage Control*, 39431, 133–147.
- Lai, J., Guo, J., Ma, Y., Zhou, H., Wang, S., Liu, Y. (2022). Effect of Acid–Rock Reaction on the Microstructure and Mechanical Property of Tight Limestone. *Rock Mechanics and Rock Engineering*, 55(1), 35–49. <https://doi.org/10.1007/s00603-021-02650-5>
- Lai, J., Guo, J., Wu, K., Chen, C., Wang, K., Wang, S., Lu, C., Zhao, X., An, H. (2019). The effects of initial roughness and mechanical property of rough fracture surface on hydraulic fracture conductivity. *53rd U.S. Rock Mechanics/Geomechanics Symposium*, 194780
- Laubach, E., Lander, R., Criscenti, L., Anovitz, I., Urai, J., Pollyea, R., Hooker, J., Narr, W., Evans, M., Kerisit, S., Olson, E., Dewers, T., Fisher, D., Bodnar, R., Evans, B., Dove, P., Bonnell, L., Marder, M., Pyrak-Nolte, L., (2019) The Role of Chemistry in Fracture Pattern Development and Opportunities to Advance Interpretations of Geological Materials. *Adv E Spa Sci* (2019)1065-1111. <https://doi.org/10.1029/2019RG000671>
- Lei, Q., Latham, J.P., Xiang, J., Lang, P. (2014). Coupled FEMDEM-DFN model for characterizing the stress-dependent permeability of an anisotropic fracture system. *International Discrete Fracture Network Engineering Conference*, 177, 1–8.
- Li, B., Jiang, Y., Koyama, T., Jing, L., Tanabashi, Y. (2008). Experimental study of the hydro-mechanical behavior of rock joints using a parallel-plate model containing contact areas and artificial fractures. *International Journal of Rock Mechanics and Mining Sciences*, 45(3), 362–375. <https://doi.org/10.1016/j.ijrmms.2007.06.004>
- Liang, Y., Huo, R., Mu, Y., Song, Z. (2023). Coupled Chemical and Mechanical Damage Model for Acid-Corroded Sandstone. *International Journal of Geomechanics*, 23(3), 1–11. <https://doi.org/10.1061/ijgnai.gmeng-7825>
- Lima Filho, M. (1998). *Análise Estratigráfica e Estrutural da Bacia Pernambuco*. Universidade de São Paulo.
- Lima Filho, M., Barbosa, J., Souza, E. (2006). Eventos Tectônicos e sedimentares nas bacias de Pernambuco e da Paraíba: Implicações no quebramento do Gondwana e correlação com a bacia do Rio Muni. *Geociências*, 25(13), 117–126.

- Lucia, J. (2007). *Carbonate reservoir characterization- an integrated approach* (2nd ed.).
- Lund, K., Foglers, H. S., Mccune, C. C., Ault, J. W. (1975). Acidization-II. the dissolution of calcite in hydrochloric acid. *Chemical Engineering Science*, 30, 825–335.
- Mabesoone, J., and Alheiros, M. (1988). A origem da Bacia Sedimentar Costeira PERNAMBUCO-PARAÍBA. *Revista Brasileira de Geociencias*, 18, 476–482.
- Manzoli, O. L., Maedo, M. A., Bitencourt, L. A. G., Rodrigues, E. A. (2016). On the use of finite elements with a high aspect ratio for modeling cracks in quasi-brittle materials. *Engineering Fracture Mechanics*, 153, 151–170. <https://doi.org/10.1016/j.engfracmech.2015.12.026>
- McGuire, T., Elsworth, D., Karcz, Z. (2011). Roles on chemical and mechanical processes on the evolution of fracture permeability. *American Rock Mechanics Association*, 1–5.
- McKee, C.R., Bumb, A.C., Koenig, R. A. (1988). Stress-Dependent Permeability and Porosity of Coal and Other Geologic Formations. *Society of Petroleum Engineers, SPE 12858*(March), 81–91. <https://doi.org/10.2118/12858-PA>
- Min, B. K., Rutqvist, J., Tsang, C. F., Jing, L. (2004). Stress-dependent permeability changes of fractured rock masses: a numerical study. *International Journal of Rock Mechanics and Mining Science*, 41(April), 1191–1210. <https://doi.org/10.1016/j.ijrmms.2004.05.005>
- Miranda, T., Filho, J., Neves, B., Barbosa, J. A. (2012). *Estudo do comportamento geológico-estrutural dos depósitos cretácicos do sistema aquífero Apodi, Bacia Potiguar, NE do Brasil*. 22(1), 3–19.
- Mou, J., Zhu, D., Hill, A. (2010). Acid-Etched Channels in Heterogeneous Carbonates — a Newly Discovered Mechanism for Creating Acid-Fracture Conductivity. *SPE Hydraulic Fracturing Technology Conference*, 119619.
- Multu, O., Pollar, D. D. (2006). A Complementarity Approach for Modeling Fractures. *American Rock Mechanics Association*, 1058(June), 1–9.
- Mumallah, N. A. (1996). Hydrochloric acid diffusion coefficients at acid-fracturing conditions. *Journal of Petroleum Science and Engineering*, 15(2–4), 361–374. [https://doi.org/10.1016/0920-4105\(95\)00086-0](https://doi.org/10.1016/0920-4105(95)00086-0)
- Mustafa, A., Alzaki, T., Aljawad, M., Solling, T., Dvorkin, J. (2022). Impact of acid wormhole on the mechanical properties of chalk, limestone, and dolomite:

- Experimental and modeling studies. *Energy Reports*, 8, 605–616.  
<https://doi.org/10.1016/j.egyr.2021.11.249>
- Nascimento-Silva, M., Sial, A., Ferreira, V., Neumann, V., Barbosa, J., Pimentel, M., de Lacerda, L. (2011). Cretaceous-Paleogene transition at the Paraíba Basin, Northeastern, Brazil: Carbon-isotope and mercury subsurface stratigraphies. *Journal of South American Earth Sciences*, 32(4), 379–392.  
<https://doi.org/10.1016/j.jsames.2011.02.014>
- Nelson, R. A. (1979). Natural Fracture Systems: Description and Classification. In *The American Association of Petroleum Geologist Bulletin* (Vol. 63, Issue 12).  
<https://doi.org/10.1306/2F91890F-16CE-11D7-8645000102C1865D>
- Nelson, R. A. (2000). Geomechanics for Reservoir Management. In *Department of Energy National Petroleum Technology Office* (Issue June, pp. 101–124).  
<https://doi.org/10.1016/B978-088415317-7/50005-1>
- Nelson, R. A. (2001). Geologic Analysis of Naturally Fractured Reservoirs. In Butterworth–Heinemann. (Ed.), *Geologic Analysis of Naturally Fractured Reservoirs* (Second edi). Gulf professional publishing.  
<https://doi.org/10.1016/B978-088415317-7/50005-1>
- Neumann, L., De Oliveira, J., Brandão, E., Oliveira, T. (2012). Acid Fracturing : New Insights on Acid Etching Patterns from Experimental Investigation. *SPE Hydraulic Fracturing Technology Conference*, 152179, 9.
- Neumann, V., Barbosa, J. A., Valberlândia, M., Sial, A., De Lima, M. (2009). Sedimentary development and isotope analysis of deposits at the Cretaceous/Palaeogene transition in the Paraíba Basin, NE Brazil. *Geologos*, 15(2), 103–113.
- Ng, K., Santamarina, J. C. (2022). Mechanical and hydraulic properties of carbonate rock : The critical role of porosity. *Journal of Rock Mechanics and Geotechnical Engineering*. <https://doi.org/10.1016/j.jrmge.2022.07.017>
- Nguyen, T., Selvadurai, A. (1998). A model for coupled mechanical and hydraulic behavior of a rock joint. *International Journal for Numerical and Analytical Methods in Geomechanics* , 22(1), 29–48.
- Nino-Penaloza, A., Al-Momin, A., Zhu, D., Hill, A. D. (2015). New Insights About Acid Fracture Conductivity at Laboratory Scale. *SPE Annual Technical Conference*, 174990.

- Okubo, J. (2014). *Calcários Albianos de Campo Petrolífero na Bacia de Campos: Fácies, Diagênese e Modelo Depositional*.
- Okubo, J., Lykawka, R., Warren, L., Favoreto, J., Dias-Brito, D. (2015). Depositional, diagenetic and stratigraphic aspects of Macaé Group carbonates (Albian): Example from an oilfield from Campos Basin. *Brazilian Journal of Geology*, 45(2), 243–258. <https://doi.org/10.1590/23174889201500020005>
- Oliveira, S., Oliveira, A., Guimarães, L., Gomes, I., Filho, O. (2020). Analysis of geomechanical behavior of carbonate rock fractures. *American Rock Mechanics Association*, 1757, 1–8.
- Olivella, S., Gens, A., Carrera, J., Alonso, E. E. (1996). Numerical formulation for a simulator (CODE\_BRIGHT) for the coupled analysis of saline media. *Engineering Computations*, 13(7), 87–112. <https://doi.org/10.1108/02644409610151575>
- Olsson, R., Barton, N., Barton, N., Paulo, S. (2001). An improved model for hydromechanical coupling during shearing of rock joints. In *International Journal of Rock Mechanics & Mining Sciences* (Vol. 38).
- Olsson, W. (1992). The effect of slip on the flow of fluid through a fracture. *Geophysical Research Letters*, 19(6), 541–543.
- Ordoñez, A., Peñuela, G., Idobro, E.A., y Medina, C. E. (2001). Recent advances in Naturally Fractured Reservoir Modeling. *CT&F – Ciencia, Tecnología y Futuro*, 2(2), 51–64.
- Oskan, E. (2013). Effect of Pressure-Dependent Natural-Fracture Permeability on Shale-Gas Well Production. *Artificial Lift & Production - Congress*, 1–25.
- Osorio, J.G., Chen, H.Y., Teufel, L.W., Schaffer, S. (1998). A Two-Domain, 3D, Fully Coupled Fluid-Flow/Geomechanical Simulation Model for Reservoirs With Stress-Sensitive Mechanical and Fluid-Flow Properties. *Society of Petroleum Engineers, SPE 47397*(July), 456–465. <https://doi.org/10.2118/47397-MS>
- Osorio, J.G., Chen, H.Y., Teufel, L. W. (1997). Numerical simulation of coupled fluid-flow/geomechanical behavior of tight gas reservoirs with stress sensitive permeability. *Society of Petroleum Engineers, SPE 39055*(August), 1–15.
- Ostensen, R. W. (1987). The effect of stress-dependent permeability on gas production and well testing. *Society of Petroleum Engineers, SPE 11220*(June), 227–237.
- Paluszny, A., and Matthai, S. K. (2008). Numerical simulation of geomechanic fracture networks: application to measuring effective permeability variability. *American*



- Rock Mechanics Association, ARMA 08-29(July), 1–9.*  
<http://www.onepetro.org/mslib/servlet/onepetropreview?id=ARMA-08-295>
- Parandeh, M., Dehkohne, H., Soulgani, B. (2023). Experimental investigation of the acidizing effects on the mechanical properties of carbonated rocks. *Geoenergy Science and Engineering*, 222. <https://doi.org/10.1016/j.geoen.2023.211447>
- Paterson, M., and Olgaard, D. (2000). Rock deformation tests to large shear strains in torsion. *Journal of Structural Geology*, 22(2000), 1341–1358.  
[www.elsevier.nl/locate/jstrugeo](http://www.elsevier.nl/locate/jstrugeo)
- Pessoa Neto, O., Soares, U., Fernandes, J., Roesner, E., Pires, C., De Souza, C. (2007). Bacia Potiguar. *Boletim de Geociências Da Petrobras.*, 15(2), 357–369.
- Petunin, V., Tutuncu, A.N., Prasad, M., Kazemi, H., Yin, X. (2011). An Experimental Study For Investigating the Stress Dependence of Permeability In Sandstones And Carbonates. *American Rock Mechanics Association*, 279(June), 1–9.  
<http://www.onepetro.org/mslib/servlet/onepetropreview?id=ARMA-11-279>
- Pinzon, C.L., Chen, H.Y., Teufel, L. W. (2001). Numerical Well Test Analysis of Stress-Sensitive Reservoirs. *Society of Petroleum Engineers, SPE 71034(May)*, 1–10.  
<https://doi.org/10.2523/71034-MS>
- Plesha, M. E. (1987). Constitutive models for rock discontinuities with dilatancy and surface degradation. *International Journal for Numerical and Analytical Methods in Geomechanics*, 11(4), 345–362.
- Portella, Y., and Fabianovicz, R. (2017). *Bacia Potiguar - Sumário Geológico e Setores em Oferta Superintendência de Definição de Blocos.*
- Pournik, M., Zhu, D., Hill, A. (2009). Acid-fracture conductivity correlation development based on acid-fracture characterization. *8th European Formation Damage Conference 2009 - New Technologies for Conventional and Unconventional Reservoirs*, 2, 1078–1092. <https://doi.org/10.2118/122333-ms>
- Pournik, M., Zou, C., Malagon, C., Melendez, M., Zhu, D., Hill, A., Weng, X. (2007). Small-scale fracture conductivity created by modern acid-fracture fluids. *SPE - Hydraulic Fracturing Technology Conference 2007*, 106272, 394–415.  
<https://doi.org/10.2118/106272-ms>
- Raghavan, R., and Chin, L. Y. (2004). Productivity Changes in Reservoirs With Stress-Dependent Permeability. *Society of Petroleum Engineers, SPE 88870(August)*, 308–315. <https://doi.org/10.2118/77535-MS>

- Rajagopalan, S., and Prakash, V. (1999). A Modified Torsional Kolsky Bar for Investigating Dynamic Friction. *Experimental Mechanics*, 39(4), 295–303.
- Rassouli, F., and Zoback, M. (2018). Comparison of Short-Term and Long-Term Creep Experiments in Shales and Carbonates from Unconventional Gas Reservoirs. *Rock Mechanics and Rock Engineering*, 51(7), 1995–2014. <https://doi.org/10.1007/s00603-018-1444-y>
- Rhett, D.W. and Teufel, L. W. (1992). *Stress path dependence of matrix permeability of North Sea reservoir rock*. 345–354.
- Rodríguez, X. A. (2017). *Daño geomecánico de sistemas naturalmente fracturados debido a esfuerzos inducidos por producción de fluidos*. Universidad Nacional de Colombia - Sede Medellín.
- Rodríguez, X. A., Guimarães, L., Canabarro, B. (2022). Hydromechanical analysis of fractured carbonates via finite elements with embedded discontinuities : scenarios based on the Brazilian Pre-salt. *CILAMCE Proceedings of the Joint XLIII Ibero-Latin American Congress on Computational Methods in Engineering*.
- Rodríguez, X. A., and Osorio, J. G. (2019). Near-wellbore geomechanical damage of naturally fractured system due to production-induced stresses. *Rock Mechanics for Natural Resources and Infrastructure Development- Proceedings of the 14th International Congress on Rock Mechanics and Rock Engineering, ISRM 2019*, 373, 3066–3082.
- Rong, G., Peng, J., Wang, X., Liu, G., Hou, D. (2013). Permeability tensor and representative elementary volume of fractured rock masses of fractured rock masses. *Hydrogeology Journal*, 21(November), 1655–1671. <https://doi.org/10.1007/s10040-013-1040-x>
- Safari, M.R., and Ghassemi, A. (2010). 3D Poroelastic Analysis of Natural Fracture Response to Variable Injection/Extraction Rates. *American Rock Mechanics Association, ARMA 10-32*(June), 1–8.
- Santos, B., Piovesan, M., Fauth, E., Srivastava, N. (2015). Paleoenvironmental interpretation through the analysis of ostracodes and carbonate microfacies: Study of the Jandaíra Formation, Upper Cretaceous, Potiguar Basin. *Brazilian Journal of Geology*, 45(1), 23–34. <https://doi.org/10.1590/23174889201500010002>
- Santos, M., Cassab, R., Campos, D., Brito, I., Carvalho, I., Tinoco, I., Duarte, L., Carvalho, M., Lima, M. (1994). The Pernambuco-Paraíba Basin. In G. Beurlen, D.

- Campos, V. M, *Stratigraphic range of Cretaceous of mega and macrofossils of Brazil* (Issue January, pp. 245–272). Universidade Federal do Rio de Janeiro. [https://www.researchgate.net/publication/236231193\\_The\\_Pernambuco-Paraiba\\_Basin](https://www.researchgate.net/publication/236231193_The_Pernambuco-Paraiba_Basin)
- Sartorato, A., Tonietto, S., and Pereira, E. (2020). Silicification and dissolution features in the Brazilian Pre-salt Barra Velha formation: impacts in the reservoir quality and insights for 3D geological modeling. *Rio Oil and Gas Expo and Conference*, 20(2020), 68–69. <https://doi.org/10.48072/2525-7579.rog.2020.068>
- Sayles, R., and Thomas, T. (1978). Surface topography as nonstationary random process. *Nature*, 271(2), 431–434.
- Schoenball, M., Sahara, D. P., Kohl, T. (2014). Time-dependent brittle creep as a mechanism for time-delayed wellbore failure. *International Journal of Rock Mechanics and Mining Sciences*, 70, 400–406. <https://doi.org/10.1016/j.ijrmms.2014.05.012>
- Scholle, P., and Ulmer-Scholle, D. (2005). A color guide to the petrography of carbonate rocks: Grains, textures, porosity, diagenesis. In *AAPG Memoir* (Issue 77).
- Sijing, W., and Xingtang, L. (1991). Geomechanical evaluation of crustal stability. *Congress International Society of Rock Mechanics*, 1785–1790.
- Smith, D., Jenkins, R., Buhrke, V. (1998). *Preparation of specimens for X-Ray fluorescence and X-Ray diffraction analysis* (Vol. 1).
- Soares, A. C., and Ferreira, F. H. (2002). An Experimental Study For Mechanical Formation Damage. *Society of Petroleum Engineers, SPE 73734*(February), 1–10. <https://doi.org/10.2523/73734-MS>
- Sone, H., and Zoback, M. (2013). Mechanical properties of shale-gas reservoir rocks - Part 2: Ductile creep, brittle strength, and their relation to the elastic modulus. *Geophysics*, 78(5). <https://doi.org/10.1190/GEO2013-0051.1>
- Song, X., Zhu, Y., Iiu, Q., Chen, J., Ren, D., Li, Y., Wang, B., Liao, M. (1998). Identification and Distribution of Natural Fractures. *Society of Petroleum Engineers, SPE 50877*(November), 45–51.
- Suárez, D. (1998). Deslizamientos y Estabilidad de Taludes en Zonas Tropicales. In *Deslizamientos y estabilidad de taludes en zonas tropicales*.

- Swan, G. (1983). Determination of Stiffness and Other Joint Properties from Roughness Measurements. *Rock Mechanics and Rock Engineering*, 16(1), 19–38.
- Takahashi, M., and Koide, H. (1995). Three principal stress effects on permeability of Shirahama sandstone. *International Society for Rock Mechanics*, 148(June), 729–732.
- Tarrahi, M., Jafarpour, B., Ghassemi, A. (2013). Geomechanical Reservoir Characterization with Microseismic Data. *Society of Petroleum Engineers, SPE* 165683 (August), 1–14.
- Teufel, L. W. (1987). Permeability changes during shear deformation of fractured rock. *American Rock Mechanics Association*, 0473(July), 473–480.  
<https://www.onepetro.org/conference-paper/ARMA-87-0473>
- Tezuka, K., Tamagawa, T., Watanabe, K. (2005). Numerical Simulation of Hydraulic Shearing in Fractured Reservoir. *World Geothermal Congress*, 24–29.
- Thomas, T. (1999). *Rough Surfaces* (Vol. 2).
- Timoshenko, S., Gere, J. (1993). *Mecânica dos Sólidos* (Vol. 1).
- Tovar, J., and Salazar, A. (2007). Integrating Drilling and Geomechanical Damage in Sandstone Reservoirs: Identification, Quantification, and Removal. *Society of Petroleum Engineers, SPE* 107611(May), 1–8.
- Tucker, M., and Bathurst, R. (1990). *Carbonate diagenesis* (Vol. 1).  
[https://books.google.com.br/books?id=L24lsW38YE0C&printsec=frontcover&source=gbg\\_ge\\_summary\\_r&cad=0#v=onepage&q&f=false](https://books.google.com.br/books?id=L24lsW38YE0C&printsec=frontcover&source=gbg_ge_summary_r&cad=0#v=onepage&q&f=false)
- Tucker, M., Wright, V., and Dickson, J. (1990). *Carbonate sedimentology*. Blackwell Scientific Publications.
- Vitha, M. (2015). Total-reflection X-Ray fluorescence analysis and related methods. In *Chemical analysis* (Vol. 1, p. 527).
- Walsh, J. B. (1981). Effect of Pore Pressure and Confining Pressure on Fracture Permeability. In *Int. J. Rock Mech. Min. Sci. & Geomech. Abstr* (Vol. 18).
- Wayne, M. (2008). Geology of Carbonate Reservoirs: The Identification, Description, and Characterization of Hydrocarbon Reservoirs in Carbonate Rocks. In *Geology of Carbonate Reservoirs: The Identification, Description, and Characterization of Hydrocarbon Reservoirs in Carbonate Rocks*.  
<https://doi.org/10.1002/9780470370650>

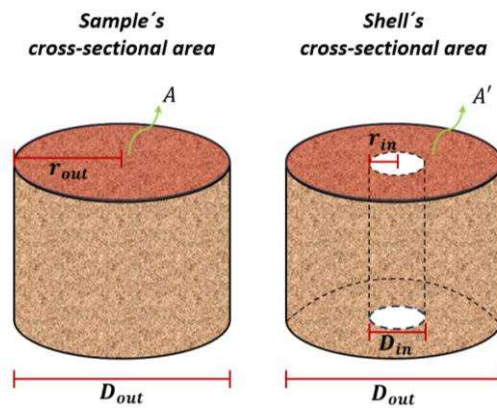
- Wu, W., Szabian, M., Sharma, M. (2020). Effect of Acid Etching on Surface Topography, Mechanical Properties and Fracture Conductivity in Shale. *Unconventional Technology Conference - SPE*, 3177. <https://doi.org/10.15530/urtec-2020-3177>
- Xiao, Y., Wang, H., Mi, Z., Cheng, Y., Cao, X., Qu, J., Guo, J. (2020). Laboratory Measurements of Acid-Etched Fracture Conductivity for Medium-High Porosity and Low Permeability Limestone Reservoirs in EE Oil Field. *American Rock Mechanics Association*, 20(1394), 6.
- Xu, S., and Freitas, M. (1988). Use of a rotary shear box for testing strength of rock joints. *Geotechnique*, 38(2), 301–309.
- Yuan, F., and Prakash, V. (2008). Use of a modified torsional Kolsky bar to study frictional slip resistance in rock-analog materials at coseismic slip rates. *International Journal of Solids and Structures*, 45(14–15), 4247–4263. <https://doi.org/10.1016/j.ijsolstr.2008.03.012>
- Yuting, D., Xudong, J., Yingfeng, M., Pingya, L. (2000). Closure Behaviour of Natural Rock Fractures. *Society of Petroleum Engineers, SPE* 62539(June), 1–9. <https://doi.org/10.1306/A967359A-1738-11D7-8645000102C1865D>
- Zhang, J., Bai, M., Roegiers, J. C., Liu, T. (1999). Determining stress-dependent permeability in the laboratory. *American Rock Mechanics Association*, 0341(March), 341–347.
- Zhang, W., Jin, X., & Zhu, D. (2018). A Model for Acid Fracture Conductivity Based on Asperity Deformation with Coupled Normal-Shear Behavior of Rough Surfaces. *SPE - Hydraulic International Hydraulic Fracturing Technology Conference*, 191456(18IHFT-MS), 14.
- Zhou, X., and Ghassemi, A. (2009). Three-dimensional Poroelastic Displacement Discontinuity Simulation of Natural Fractures. *American Rock Mechanics Association*, 09–154(June), 1–7.
- Zimmerman, R., and Bodvarsson, G. (1996). Hydraulic Conductivity of Rock Fractures. *Transport in Porous Media*, 23(1), 1–30.
- Zoback, M. D. (2007). Reservoir Geomechanics. In Cambridge.org (Ed.), *First edition* (first, pp. 1–507).

## APPENDAGES

### APPENDIX 1 – DETERMINATION OF THE EFFECTIVE NORMAL STRESS, [ $\sigma'$ ]

The rock specimen is considered to have a cylindrical shape. Figure A1- 1 represents the cross-sectional area of the sample and the sample's shell. The subscript *out* denotes the outer or external diameter ( $D_{out}$ ) and radius ( $r_{out}$ ) of the sample, while *in* corresponds to inner or internal diameter ( $D_{in}$ ) and radius ( $r_{in}$ ) of the tube's hole.

Figure A1- 1 Sketch of the cross-sectional area of the sample and sample's shell.



Author

Equation (A1.1) determines the cross-sectional area of the specimen,

$$A = \pi r_{out}^2 \quad (A1.1)$$

Rewritten Equation (A1.1) as a function of the outer diameter,

$$A = \pi \left( \frac{D_{out}}{2} \right)^2 = \frac{\pi}{4} D_{out}^2 \quad (A1.2)$$

Likewise, the cross-sectional area of the tube's hole (internal area,  $A_{in}$ ),

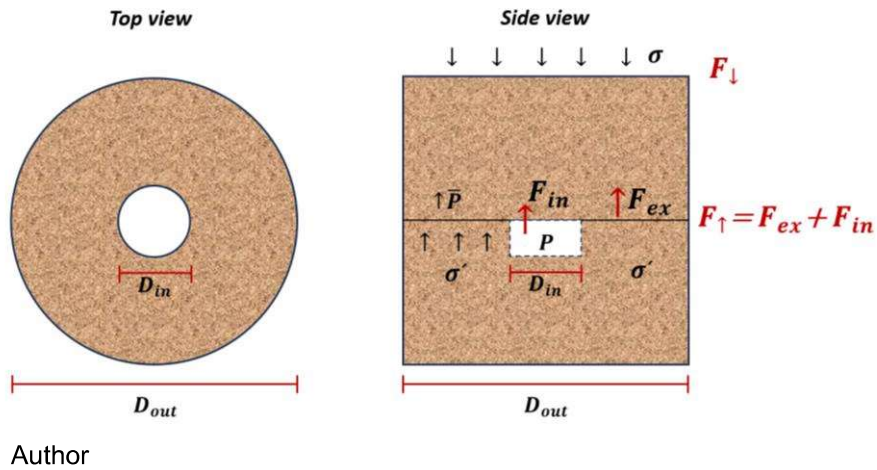
$$A_{in} = \pi r_{in}^2 = \frac{\pi}{4} D_{in}^2 \quad (A1.3)$$

Equation (A1.4) determines the cross-sectional area of the shell's specimen (shell's area,  $A'$  ),

$$A' = \frac{\pi}{4} D_{out}^2 - \frac{\pi}{4} D_{in}^2 = \frac{\pi}{4} (D_{out}^2 - D_{in}^2) \quad (A1.4)$$

Figure A1- 2 shows a sketch of a specimen's top and side view. This figure provides detailed information about the stress and pressure conditions experienced by rock during the experiments.

Figure A1- 2 Sketch of a top and side view of a specimen.



From a balance force, an applied force ( $F_{\downarrow}$ ) and resultant force ( $F_{\uparrow}$ ) equivalents to zero (see Figure A1- 2),

$$F_{\downarrow} + F_{\uparrow} = 0 \quad (A1.5)$$

Force ( $F$ ) can be defined as the product of stress ( $\sigma$ ) and cross-sectional area, expressed mathematically as:

$$F = \sigma A \quad (A1.6)$$

Thus, the applied force could be written as,

$$F_{\downarrow} = \sigma A = \sigma \frac{\pi}{4} D_{out}^2 \quad (A1.7)$$

The called resultant force results from the sum of the internal force ( $F_{in}$ ) and external force ( $F_{ex}$ ), (see Figure A1- 2),

$$F_{\uparrow} = F_{in} + F_{ex} \quad (A1.8)$$

Therefore, applying the definition of equation A1.6, the internal force results from the product of the internal area and fluid pressure ( $P$ ),

$$F_{in} = PA_{in} = P \frac{\pi}{4} D_{in}^2 \quad (A1.9)$$

Equation A1.10 describes the external force derived from the product of the shell's area and the pressure acting on the fracture surface.

$$F_{ex} = (\bar{P} + \sigma') A' = (\bar{P} + \sigma') \frac{\pi}{4} (D_{out}^2 - D_{in}^2) \quad (A1.10)$$

where  $\bar{P}$  represents the average pressure through the fracture (pressure mean), and  $\sigma'$  is the effective stress acting on the fracture plane. Using equations A1.9 and A1.10 in equation A1.8, equation A1.8 could be rewritten as,

$$F_{\uparrow} = \frac{\pi}{4} D_{out}^2 P + \frac{\pi}{4} (D_{out}^2 - D_{in}^2) (\bar{P} + \sigma') \quad (A1.11)$$

Substituting equations A1.7 and A1.11 in equation A1.5,

$$\sigma \frac{\pi}{4} D_{out}^2 = P \frac{\pi}{4} D_{in}^2 + \frac{\pi}{4} (D_{out}^2 - D_{in}^2) (\bar{P} + \sigma') \quad (A1.12)$$

Factorizing terms,

$$\sigma D_{out}^2 - P D_{in}^2 - \bar{P} (D_{out}^2 - D_{in}^2) = \sigma' (D_{out}^2 - D_{in}^2) \quad (A1.13)$$

Finally,

$$\sigma' = \frac{\sigma D_{out}^2 - P D_{in}^2}{(D_{out}^2 - D_{in}^2)} - \bar{P} \quad (A1.14)$$



## APPENDIX 2 – DETERMINATION OF AVERAGE PRESSURE THROUGH THE FRACTURE OR PRESSURE MEAN, $[\bar{P}]$

From Darcy's law have the follow proportionality ( $\alpha$ ),

$$Q \propto A_s \frac{dP}{dr} = cte \quad (A2.1)$$

$$\frac{Q}{2\pi h} \propto r \frac{dP}{dr} \rightarrow \frac{\gamma Q}{2\pi h} = \beta \quad (A2.2)$$

where  $\gamma$  is a proportionality constant and  $\beta$  is a constant. Thus,

$$r \frac{dP}{dr} = \beta \rightarrow \frac{dP}{dr} = \frac{\beta}{r} \rightarrow dP = \frac{\beta dr}{r} \rightarrow \int dP = \int \beta \frac{dr}{r} \quad (A2.3)$$

Developing the integration constants  $c_1$  and  $c_2$  are obtained. Both constant will be called constant  $c$  in the general solution (equation A2.5).

$$P + c_1 = \beta \ln(r) + c_2 \quad (A2.4)$$

$$P = \beta \ln(r) + c \quad (A2.5)$$

By applying the follow boundary condition in the general solution: when the radius ( $r$ ) is equal to ( $r_{out}$ ), the pressure equivalents to the outer or external pressure ( $P_{out}$ ), as follows,

$$P_{out} = \beta \ln(r_{out}) + c \quad (A2.6)$$

Solving  $c$ ,

$$c = P_{out} - \beta \ln(r_{out}) \quad (A2.7)$$

Replacing  $c$  in the general solution,

$$P = \beta \ln(r) + P_{out} - \beta \ln(r_{out}) \quad (A2.8)$$

$$P = P_{out} + \beta [\ln(r) - \ln(r_{out})] \quad (A2.9)$$

$$P = P_{out} + \beta \ln\left(\frac{r}{r_{out}}\right) \quad (A2.10)$$

Now,  $\beta$  is obtained by imposing a second boundary condition in equation A2.10. When the radius ( $r$ ) is equal to ( $r_{in}$ ), the pressure equals to the inner or internal pressure ( $P_{in}$ ), such as

$$P_{in} = P_{out} + \beta \ln\left(\frac{r_{in}}{r_{out}}\right) \quad (A2.11)$$

Solving  $\beta$ ,

$$\beta = \frac{(P_{in}-P_{out})}{\ln\left(\frac{r_{in}}{r_{out}}\right)} \quad (A2.12)$$

Replacing  $\beta$  in equation A2.10, an expression to calculate pressure as a function of the ratio is obtained,

$$P(r) = P_{out} + \frac{(P_{in}-P_{out}) \ln\left(\frac{r}{r_{out}}\right)}{\ln\left(\frac{r_{in}}{r_{out}}\right)} \quad (A2.13)$$

Equation A2.13 is integrating between  $r_{in}$  to  $r_{out}$ , (equations A2.14 to A2.16),

$$\int_{r_{in}}^{r_{out}} P(r) = \int_{r_{in}}^{r_{out}} P_{out} + \frac{(P_{in}-P_{out}) \ln\left(\frac{r}{r_{out}}\right)}{\ln\left(\frac{r_{in}}{r_{out}}\right)} dr \quad (A2.14)$$

$$= P_{out}r_{out} - P_{in}r_{in} + \frac{(P_{in}r_{in}-P_{in}r_{out}-P_{out}r_{in}+P_{out}r_{out})}{\ln\left(\frac{r_{in}}{r_{out}}\right)} \quad (A2.15)$$

$$= (P_{out}r_{out} - P_{in}r_{in}) + \frac{[(r_{in}-r_{out})(P_{in}-P_{out})]}{\ln\left(\frac{r_{in}}{r_{out}}\right)} \quad (A2.16)$$

Finally, equation A2.16 is divided in the range of the function to obtain  $\bar{P}$ ,

$$\bar{P} = \frac{(P_{out}r_{out}-P_{in}r_{in}) + \frac{[(r_{in}-r_{out})(P_{in}-P_{out})]}{\ln\left(\frac{r_{in}}{r_{out}}\right)}}{r_{out}-r_{in}} \quad (A2.17)$$

### APPENDIX 3 – DETERMINATION OF FRACTURE TRANSMISSIVITY, [T]

Equation A3.1 describes Darcy's law for radial flow, which considers single-phase fluid, constant stress, and constant permeability with respect to radius and depth.

$$Q = \frac{K_I A_s}{\mu} \frac{\partial P}{\partial r} \quad (\text{A3.1})$$

where  $Q$  corresponds to the flow rate,  $K_I$  represent to the intrinsic permeability,  $A_s$  denotes the area of the sample (cylinder area defined as  $2\pi r h$ ),  $\mu$  represents fluid viscosity,  $\partial P$  corresponds to the pressure differential, and  $\partial r$  corresponds to the radial distance differential. Applying cylinder area definition,

$$Q = \frac{(2\pi r h) K_I}{\mu} \frac{\partial P}{\partial r} \quad (\text{A3.2})$$

Equations A3.3 to A3.6 are obtained from resolving equation A3.1. The pressure differential  $\partial P$  denotes a pressure in the internal limit ( $p_i$ ) and a pressure in the external limit ( $p_{i+1}$ ). Similarly, the radius differential defines a radius in the internal limit ( $r_i$ ) and a radius in the external limit ( $r_{i+1}$ ).

$$\frac{(2\pi h) K_I}{Q \mu} \partial P = \frac{\partial r}{r} \quad (\text{A3.3})$$

$$\frac{(2\pi h) K_I}{Q \mu} \int_{P_i}^{P_{i+1}} \partial P = \int_{r_i}^{r_{i+1}} \frac{\partial r}{r} \quad (\text{A3.4})$$

$$\frac{(2\pi h) K_I}{Q \mu} (P_{i+1} - P_i) = \ln \left( \frac{r_{i+1}}{r_i} \right) \quad (\text{A3.5})$$

$$(P_{i+1} - P_i) = \left[ \left( \frac{Q \mu}{(2\pi h) K_I} \right) \ln \left( \frac{r_{i+1}}{r_i} \right) \right] \quad (\text{A3.6})$$

Equation A3.6 could be rewritten by applying the definition of the “geotechnical” permeability ( $K_G$ ), where  $\rho$  corresponds to the rock's density, and  $g$  represents gravity, as follows,

$$(P_{i+1} - P_i) = \left[ \left( \frac{Q \mu}{(2\pi h) \frac{\mu}{\rho g} K_G} \right) \ln \left( \frac{r_{i+1}}{r_i} \right) \right] \quad (\text{A3.7})$$

By definition, transmissivity is given by,

$$T = K_G h \quad (\text{A3.8})$$

Applying equation A3.8 in A3.7,

$$(P_{i+1} - P_i) = \left[ \left( \frac{Q \mu}{2\pi T \frac{\mu}{\rho g}} \right) \ln \left( \frac{r_{i+1}}{r_i} \right) \right] \quad (\text{A3.9})$$

Solving equation A3.9 for  $T$ ,

$$T = \frac{Q \rho g}{(P_i - P_{i+1})} \left( \frac{\ln \left( \frac{r_{i+1}}{r_i} \right)}{2\pi} \right) \quad (\text{A3.10})$$

Equation A3.10 is modified in terms of outer and inner diameter, such as,

$$T = \frac{Q \rho g}{(P_i - P_{i+1})} \left( \frac{\ln \left( \frac{D_{out}}{D_{in}} \right)}{2\pi} \right) \quad (\text{A3.11})$$

$$\text{Because } r = \frac{D}{2} \rightarrow \frac{r_{out}}{r_{in}} = \frac{D_{out}/2}{D_{in}/2} = \frac{D_{out}}{D_{in}}$$

Rewritten equation A3.11 by assuming the pressure at the internal limit as  $P$  and the pressure at the external limit as atmospheric pressure  $P_a$ ,

$$T = \frac{Q \rho g}{(P - P_a)} \left( \frac{\ln \left( \frac{D_{out}}{D_{in}} \right)}{2\pi} \right) \quad (\text{A3.12})$$

## APPENDIX 4 – DETERMINATION OF SHEAR STRESS FROM A TORSION DISPLACEMENT, $[\tau]$

The torque vector ( $\bar{M}$ ) is defined as the cross-product between a vector radius ( $\bar{r}$ ) and the vector force ( $\bar{F}$ ), as follows,

$$\bar{M} = \bar{r} \times \bar{F} \quad (\text{A4.1})$$

From equation A4.1, if  $\bar{r}$  is parallel to  $\bar{F}$ ,

$$M = r F \quad (\text{A4.2})$$

The torque ( $M$ ) for a differential area element ( $dA$ ) is defined as,

$$dM = dF r \quad (\text{A4.3})$$

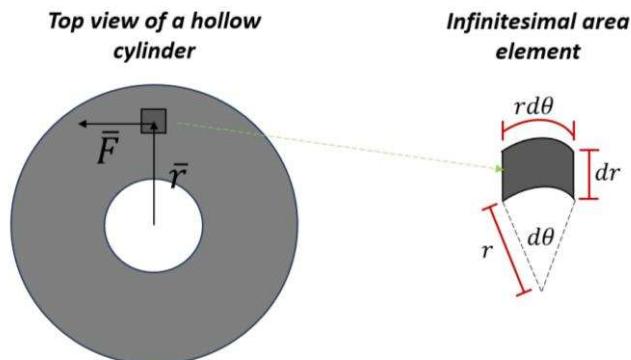
where  $dF$  is equivalent to  $\tau dA$ . Rewritten A4.3,

$$dM = \tau dA r \quad (\text{A4.4})$$

Figure A4- 1 Figure A4- 1 shows a top view of a hollow cylinder relating an infinitesimal element with radius  $dr$  and angle  $d\theta$ . The diferencial area for an infinitesimal element of a hollow cylinder is given by,

$$dA = r d\theta dr \quad (\text{A4.5})$$

Figure A4- 1 Top view of a hollow cylinder relating an infinitesimal area element of it.



Author

Rewritten equation A4.4 using equation A4.5,

$$dM = \tau r r d\theta dr \quad (\text{A4.6})$$

From equation A4.5, torque is defined as,

$$M = \int dM = \int \tau r^2 dr d\theta \quad (\text{A4.7})$$

By assuming perfectly plastic material, the shear stress acts uniformly over the cross-section (i.e., not function of  $r$  and  $\theta$ ), the torque is,

$$M = \tau \int r^2 dr d\theta \quad (\text{A4.8})$$

$$M = \tau \int_{r_{in}}^{r_{out}} r^2 dr \int_{\theta=0}^{\theta=2\pi} d\theta \quad (\text{A4.9})$$

$$M = 2\pi\tau \int_{r_{in}}^{r_{out}} r^2 dr \quad (\text{A4.10})$$

$$M = 2\pi\tau \left. \frac{r^3}{3} \right|_{r_{in}}^{r_{out}} \quad (\text{A4.11})$$

$$M = \frac{2\pi}{3}\tau (r_{out}^3 - r_{in}^3) \quad (\text{A4.12})$$

By definition, Diameter ( $D$ ) equals to  $D = 2r$ . Thus, rewritten equation A4.12,

$$M = \frac{\pi\tau}{12} (D_{out}^3 - D_{in}^3) \quad (\text{A4.13})$$

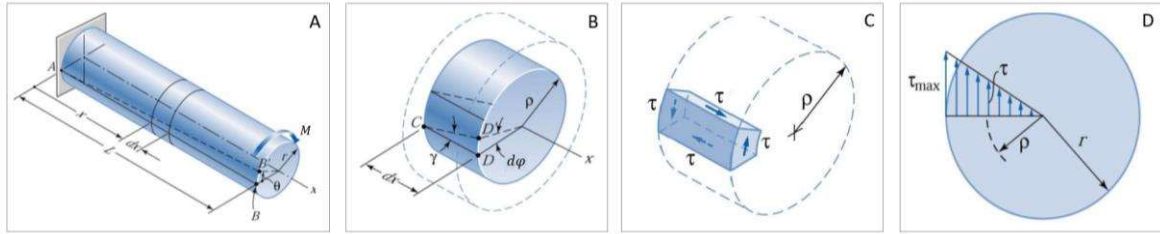
Solving shear stress ( $\tau$ ) from equation A4.13,

$$\tau = \frac{12M}{\pi(D_{out}^3 - D_{in}^3)} \quad (\text{A4.14})$$

## APPENDIX 5 – TORSION: BASIC CONCEPTS

Torsion or torsional moment refers to the twisting or rotational deformation experienced by a structural element when subjected to a torque or twisting force. The torsional force induces the material to rotate by an angle  $\theta$  about its longitudinal axis (goes from point B to B', Figure A5- 1A), resulting in a change in its cross-sectional shape (assuming rhomboidal form in the direction of  $dx$ , see Figure A5- 1B) (Beer; Jhonston; Dewolf, 2006).

Figure A5- 1 Shaft over pure torsion. A- Deformation of the shaft caused by torque ( $M$ ). B- Shear strain ( $\gamma$ ) of the shaft caused by torsion. C- Shear stress acting on an element subjected to torsion. D- Distribution of the shear stress ( $\tau$ ) along the radius of the shaft.



Source: Modified of Beer; Jhonston; Dewolf (2006, p. 132)

Figure A5- 1B shows the distance BB' corresponds with the length of an arc of radius  $r$  and angle  $d\phi$ .  $d\phi$  is the torsion angle of a cross-section compared with the other. Thus, shear strain ( $\gamma$ ) is given by,

$$\gamma = \frac{r d\phi}{dx} \quad (\text{A5.1})$$

$d\phi$  varies at a constant rate in the  $dx$  direction when the shaft experiences torsion. This constant denoted  $\theta$  and expressed in radians represents the torsion angle per unit of length ( $\theta = \phi/L$ ), where  $L$  is the shaft's length.

$$\gamma = r\theta = \frac{r\phi}{L} \quad (\text{A5.2})$$

Figure A5- 1C shows the directions of the shear stress ( $\tau$ ) acting on the element resulted from a torsion. From equation (8), being  $G$  the shear elastic modulus, the shear stress for a linearly elastic material is defined as,

$$\tau = G\gamma = Gr\theta \quad (\text{A5.3})$$

Figure A5- 1D illustrates that the radius and cross-sections inside a shaft subjected to torsion are not modified. Therefore, the shear strain and stress for an element on the surface of a cylinder with radius  $\rho$ , can be calculated as follows,

$$\gamma = \rho\theta \quad (\text{A5.4})$$

$$\tau = G\rho\theta \quad (\text{A5.5})$$



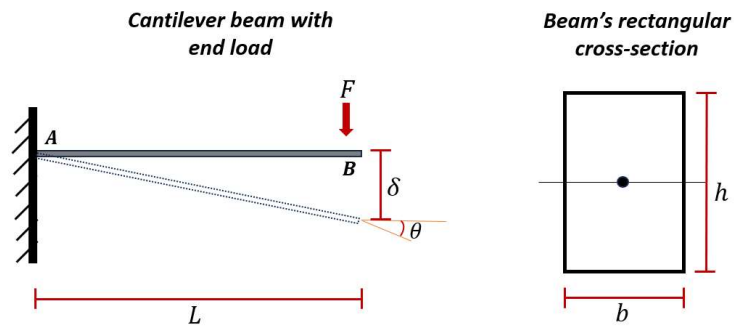
## APPENDIX 6 – STRESS AND STRAIN IN A CANTILEVER BEAM

Figure A6- 1 shows a cantilever beam with end load ( $F$ ). From the moment-area theorem the angle between points  $A$  and  $B$  is defined by Timoshenko and Gere (1993) as,

$$\theta = \frac{FL^2}{2EI} \quad (\text{A6.1})$$

Where  $E$  corresponds with Young's modulus, and  $I$  is the inertial moment. Equation (3) is negative when the tangent of  $B$  rotates clockwise, concerning the tangent of the point  $A$ .

Figure A6- 1 Cantilever beam deflection scheme when experiencing an end load.



Source: Modified of Timoshenko and Gere (1993, p. 96 and 146)

When a beam has a rectangular cross-section, width ( $b$ ), and height ( $h$ ), the moment of inertia is described as follows (Timoshenko and Gere, 1993),

$$I = \frac{bh^3}{12} \quad (\text{A6.2})$$

Equation (4) defines the distance ( $\Delta$ ) between point  $B$  and the tangent of  $A$ ,

$$\Delta = -\frac{FL^2}{2EI} \left( \frac{2L}{3} \right) \quad (\text{A6.3})$$

### 8.3.1

Timoshenko and Gere (1993) describe the negative sign, explaining that point ***B*** of the elastic line is lower than the tangent of ***A***. Thus, the deflection ( $\delta$ , or displacement) in a cantilever beam with end load is given by,

$$\delta = \frac{FL^3}{3EI} \quad (\text{A6.4})$$